CEOS Intercalibration of Ground-Based Spectrometers and Lidars

RFQ/3-12340/08/I-EC

Contract: 22202/09/I-EC

Contract Change Notice

2012-2013

Final Report

July 2014

DOCUMENT PROPERTIES

Title	CEOS Intercalibration of Ground-Based Spectrometers and Lidars Contract Change Notice 2012-2013 - Final Report
Reference	CEOS-ICal-CCN-2012-2013-FinalReport
Issue	2.1
Revision	0
Status	Final
Date of issue	7/15/2014
Document type	Report

	FUNCTION	NAME	DATE	SIGNATURE
LEAD AUTHOR	Project coordinator	Michel Van Roozendael (BIRA)		
CONTRIBUTING AUTHORS	Project partners	Esko Kyrö (FMI) Tomi Karppinen (FMI) Alberto Redondas (AEMET) Alexander Cede (LuftBlick) François Hendrick (BIRA)		
REVIEWED BY	ESA project officer	Thorsten Fehr Stefano Casadio		
ISSUED BY	Project coordinator	Michel Van Roozendael (BIRA)		

DOCUMENT CHANGE RECORD

Issue	Revision	Date	Modified items	Observations
0.0	00	Jan 2014	Initial draft	
1.0	00	1 Feb 2014	Integrated draft for ESA review	
2.0	00	27 Feb 2014	Reviewed version, changes implemented in sections 5 and 6	
2.1	01	15 July 2014	Final version	Accepted by ESA

Contents

1 Executive summary

1.1 Brewer calibrations (WP 1)

During the project extension, two Brewer calibration campaigns were organized and 23 calibrations were performed. In these campaigns the calibration scale has been transferred from the RBCC-E triad at the Izaña Atmospheric Research Centre to the participants. A significant improvement on the reference triad characterization and its maintenance has been obtained including the development of operational procedures and the public diffusion of the status of the reference. We can estimate a long-term precision of 0.25% for the European Reference Triad. The observations from all campaigns have been submitted to the CEOS Cal-Val Database.

The cross calibration of the Toronto triad and RBCC-E could not be accomplished during the extension of the project. The indirect link through IO 017 instrument shows worse result than previously reported with discrepancies of about 1%.

The results of the campaign are worse than in previous reports. The status of the network as revealed during the calibration campaigns is that all of the operative instruments are on the +/-2% range, 66% of the Brewer instruments are inside 1% range and 1/3 shows a perfect agreement of +/- 0.5% after two years calibration period. The reference instruments, i.e. the Brewers that are used to transfer calibration, show an agreement around 0.5%.

A Stray Light empirical model presented at the SAUNA campaigns has been adapted to the calibration procedure. As the calibration accounts for the stray light, it can be made possible under high ozone slant path conditions. The application of the method to Huelva campaign data shows a perfect agreement with the original method and good performance of the correction using an iterative procedure. The application of the method to the Brewer #037 suggests that the non-linear parameters accounting for the stray light do not depend on the change in response of the instrument, which supports the characterization strategies developed by FMI.

A new set of ozone absorption coefficients for Dobson and Brewer spectrophotometers, using the five cross section laboratory data, was calculated and compared with the previous calculations. The performances of these coefficients were evaluated using the data of simultaneous Brewer and Dobson observations during the CEOS Calibration campaign and the ozone observations at Arosa. The main conclusions of our study are:

- The Brewer and Dobson instrument results agree best when the absorption coefficients used are based on the HARMONICS (IUP) cross section. The application of the temperature dependent absorption coefficients substantially reduces the seasonality found in the Arosa Brewer-Dobson record. The DBM set also reduces the seasonality but the change in absolute scale in the Brewer instrument (away from the Dobson results) makes its use unsuitable for the network.
- The temperature dependence values obtained confirm the hypothesis of Kerr (2002): the systematic annual differences between Brewer and Dobson are due to the different temperature dependence in the instrument's ozone retrieval algorithm. With the Brewer this is small; less than 0.01 %/°C. The suggestion Kerr et al. (1988) that this difference is due to the temperature dependence in the Dobson algorithm is also confirmed.

- The Dobson record will change by less than 1 % using any one of these XS dataset. A change to the temperature dependent absorption coefficients provides the largest benefit by removing an artificial seasonality in the ozone record. The application of the temperature dependent absorption coefficients will be station dependent, as knowledge of the stratospheric temperature record over the station is required. The determination of the best method to determine this record is a subject for another study.
- The calculation of the DXS for a particular Brewer instrument is very sensitive to both the XS and the handling of the XS (editing, smoothing, etc.); these differences can be as large as 1 % in ozone.
- The existing Brewer record of TOC can be adjusted to the IUP scale through the record of the wavelength calibrations. Using the average Brewer value the maximum uncertainty based on 123 instruments was 0.4 %; using the known operational absorption coefficient that uncertainty can be reduced to 0.1 %.

1.2 Single Brewer straylight error compensation (WP 2)

A model, describing Brewer stray light performance, was built. The modeling of Brewer performance was scripted on Matlab and the irradiance spectra were created with the Libradtran radiative transfer model package. The work involved is fairly demanding compared to the alternative of using a statistical model based on comparison measurements with a high quality double Brewer as described in section 3.4. On the other hand the physical model is, in principle, easy to update by just re-measuring the key parameters like slit functions and instrumental responses. It can also be used to look after differences in stray light properties under different atmospheric conditions.

The model was run over a variety of zenith angles and total ozone columns to create a lookup-table of compensation factors as needed to simulate a “single Brewer” having the characteristics of the Brewer 037, to perform like an “ideal” Brewer instrument. When the compensation was applied on real data from two CEOS-campaigns on 2011 in Izana and in Sodankylä, the performance of the Brewer 037 compared to RBCC-E Brewer was greatly improved.

A new Matlab script for the Brewer data processing was written to introduce the stray light compensation. The same compensation as used for the campaign, was applied to the 25 year-long Sodankylä ozone time series. Only direct sun measurements were analyzed and the results were presented. While the effect in the long term trend analysis is small, individual values can have large stray light errors and consequently for applications requiring highly accurate individual measurements, like e.g. for the validation of satellite sensors, the significance of stray light becomes high.

1.3 CINDI analysis and MAXDOAS developments (WP 3)

During this project extension, MAXDOAS developments have been continued with the aim to further demonstrate the technique, consolidate and harmonise retrieval methods and progress on the generation of quality controlled standardized data products, compatible with requirements defined within Copernicus/GMES for reference “in-situ” data. Work has dealt with the continued exploitation of CINDI campaign measurements, with (1) a focus on the development and assessment of tropospheric NO_2 retrieval methods and (2) the development of a new generic cloud flagging approach applicable to all scattered-light UV-Vis instruments. In addition, large efforts have been devoted to the design of a

quality controlled automated processing system for MAXDOAS measurements, based on BIRA observations and addressing issues of data reporting including comprehensive metadata provision compliant with GEOMS rules. This work was largely done in synergy with the EU FP7 NORS project. Finally the development of the MAXDOAS technique for other air quality gases than NO_2 has been continued with a particular emphasis on SO_2 and HCHO and the demonstration of their usefulness for satellite validation.

Concerning the continued exploitation of CINDI data, the main focus has been on tropospheric NO_2 studies. The NO_2 vertical profile inversion intercomparison already started during the main phase of the CEOS project has been continued and finalized. This study includes first an exercise on synthetic data analysis and second an intercomparison of real observations including also reference in-situ measurements. One interesting and somewhat unexpected result is that the NO_2 mixing ratio at the surface has been found to be even better retrieved than the tropospheric column. In contrast to the situation for the columns, even high aerosol situations do not lead to larger errors in the surface mixing ratios although there is a tendency for larger variability. As regards the intercomparison of real measurements with in-situ systems, it was concluded that reliable surface mixing ratios can be derived from MAXDOAS inversions. The uncertainties on the retrieved values was found to vary between instruments and algorithms, and for the best data set (BIRA-UV) this resulted in a correlation of 0.8 which is considered to be excellent. It is noted however that in the presence of very shallow boundary layers (early morning), most of the retrievals either failed or yielded too low NO_2 mixing ratios because of the intrinsic limited vertical resolution of the MAXDOAS measurements.

Complementing these MAXDOAS analysis, work has also been done on tropospheric NO_2 column retrieval from zenith-sky (and direct-sun) measurements using a residual approach. Although the information content is limited in comparison to MAXDOAS, this approach has the advantage of being applicable to historical long series of e.g. SAOZ measurements. Strengths and limitations of the technique have been better characterized, and an error budget has been produced.

In addition to CINDI-related activities, research also concentrated on the exploration of MAXDOAS retrieval for other gases than NO_2. In particular MAXDOAS profile inversions have been demonstrated for SO_2 and HCHO using BIRA measurements in Beijing/Xianghe (China), and their potential for satellite validation has been investigated using OMI data produced within the S5P level-2 development project. In addition, the same Beijing/Xianghe data set has been used to illustrate the MAXDOAS capabilities for HONO detection. In support of all these tropospheric studies, a new generic cloud detection methodology has been designed and applied to demonstration data sets in several sites.

In June 2013, we took part to MAD-CAT intercomparison campaign which was organized “on the spot” at MPI Mainz and gathered 16 MAX-DOAS, 3 Car-MAXDOAS and several other systems. Like for CINDI, the focus was on comparisons of NO_2, HCHO, CHOCHO, H_2O and O_4 differential slant columns densities, however in contrast to CINDI, MAD-CAT had a stronger focus on characterizing the horizontal variability of the NO_2 field using a combination of MAXDOAS systems equipped of azimuthal scanners and mobile DOAS systems. The analysis of these interesting measurements is in progress and will provide a baseline for the design of more advanced experiments on the same subject in an upcoming S5P validation campaign to be organized in Romania in 2015 or 2016.

Finally we report on recent efforts at BIRA to advance the standardization and automation of MAXDOAS data processing and data reporting. A full processing chain starting from raw measurements to inverted

and characterized vertical profiles of NO_2, aerosol and HCHO has been demonstrated for a few BIRA stations involved in the EU NORS project. As a contribution to the same project, a common GEOMS-compliant HDF file format for reporting DOAS data of all kinds and all geometries has been defined and implemented in collaboration with the GEOMS Metadata Board. This processing chain is currently under evaluation. It is our aim to extend the NORS/CEOS automatized processing to all BIRA stations, and for all relevant data products, i.e. NO_2, O_3, HCHO, SO_2, aerosols and possibly additional species such as glyoxal, BrO, HONO, H_2O.

Note that such a system could potentially be applied to a larger number of stations through establishment of suitable collaborative agreements with other NDACC partners. Considering the large spread of MAXDOAS systems developed and operated within NDACC, an intermediate level of centralization could be adopted where the processing of raw measurements to generate slant columns would still be performed by individual PI (possibly by means of a common well established software such as QDOAS). Slant columns would then be pushed into a centralized MAXDOAS profiling processing system including suitable formatting following GEOMS templates and NRT distribution on NDACC data base. Discussions along these lines have already been started confirming the interest of the community to join into such a centralized approach for NRT data production while maintaining in parallel the traditional scientific processing and development lines. **Error! Reference source not found.** illustrates the network of MAXDOAS sites that could potentially be gathered through involvement of current NDACC partners.

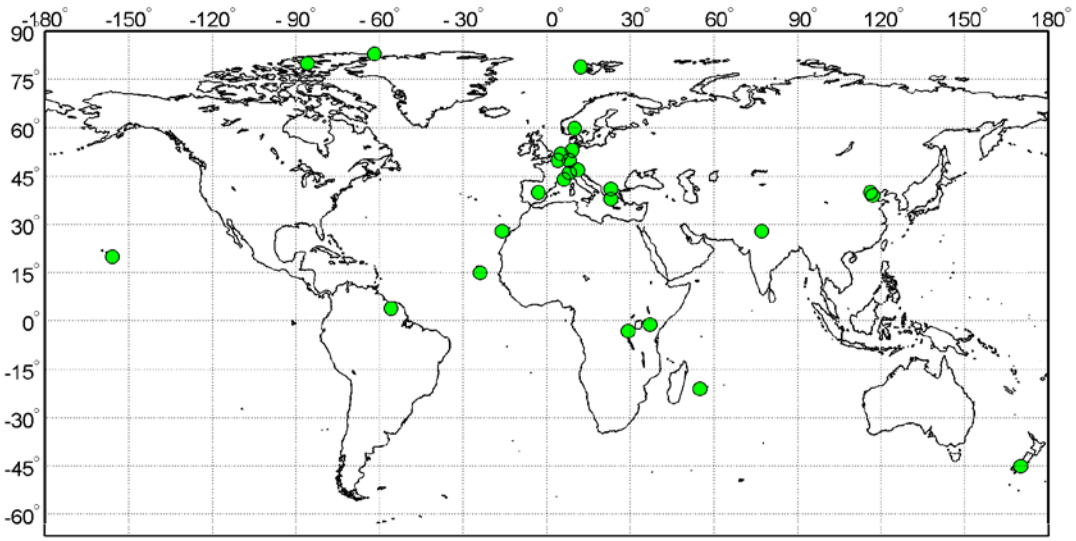

Figure 1.1. MAXDOAS sites operated by NDACC UV-Vis WG participants

1.4 Minispectrometer intercalibration and satellite validation (WP 4)

The entire data base for Pandora O_3 and NO_2 column amounts has been collected and processed using the best possible calibration for each instrument. These are the main “deficiencies” of the obtained data base.

- The data base is not calibrated like a proper network, instead a “self-calibration” was applied to each unit.
- The O_3 data are affected by spectral stray light, which biases the data for SZAs above 75-80°, depending on the instrument. An improved stray light characterization and correction should allow expanding the usable SZA-range to possibly up to 84°.
- We observed enhanced scatter in the NO_2 data, which happens usually around noon, only affects some instruments and only during specific periods and at some locations. The reason for this effect is still unknown.
- We frequently observed an additional spectral signal in the data. It seems to affect basically all instruments, but to different extent. The cause is not understood at this time. This effect does not impact the calibration, i.e. the final data are correct on average, but it is the main driver of the overall uncertainty in the retrieved O_3 and NO_2 columns and also inhibits the retrieval of weaker atmospheric species (e.g. formaldehyde) from Pandora direct sun data.

We conclude that a well-maintained Pandora is capable of measuring reliable O_3 and NO_2 data for more than years between calibrations. In addition, the instruments do not loose calibration during travel, under normal circumstances. These characteristics make Pandora an excellent network instrument. For a Pandora O_3 and NO_2 network one should use 1-3 stationary reference instruments and at least one mobile reference instrument per 25 monitoring instrument.

We validated SCIAMACHY vertical O_3 column with the Pandora data base. A sensitivity study revealed the following results:

- Distance and size of the SCIAMACHY footprint have no significant influence on the validation, as long as the ground location is included in the SCIAMACHY footprint.
- SCIAMACHY cloud fraction does not need to be limited as long as the high quality Pandora data are used.
- The ground data should be averaged over a window of 200 min around the SCIAMACHY overpass time.

Since the standard Pandora O_3 algorithm does not include a variable effective O_3 temperature we see an undulating difference between the satellite and Pandora data during the year. Pandora’s gas temperature related error is approximately 7 DU in the extreme points (summer and winter).

When attempting to perform the same validation for SCIAMACHY NO_2 data, we noticed that they are too small by a factor of ~2 at each location.

The overall conclusions of the SCIAMACHY validation are:

- Obtaining the overpass data was not a simple process. An infrastructure to extract SCIAMACHY overpass data in a clean, fast way is needed.
- Excluding Cabauw, all correlation coefficients between SCIAMACHY and Pandora vertical O_3 columns are above 0.95 and the median difference SCIAMACHY minus Pandora, corrected for the temperature cycles, are between 3 and 13 DU, which (from the Pandora side) could be attributed to a too low calibration standard.
- We can observe the excellent homogeneity of the Pandora data. Only in Cabauw are the Pandora data on average higher than the SCIAMACHY data, which could be caused by an underestimation in temperature at that location.

- The Pandora O_3 algorithm should include the effective O_3 temperature. If Pandora could retrieve effective temperature, the satellite validation study could be improved and one could also determine satellite error from the use of an effective O_3 temperature climatology. Preliminary tests have shown the retrieval of effective O_3 temperature by Pandora is possible with a further developed algorithm. We are presently working on such an algorithm to be used in routine network operation.
- The SCIAMACHY NO_2 columns underestimate the true columns by a factor of ~2 in polluted regions due to an improper tropospheric air mass factor. A meaningful validation could be done if a new SCIAMACHY data version is available, which corrected for this issue.

2 Introduction

2.1 Scope of this document

This document is the final report of the Intercalibration of ground-based spectrometers and Lidars - Extension 2012-2013. It summarizes the activities performed in the period from November 2012 until December 2013 and the main results obtained.

2.2 Acronyms and abbreviations

ACSO	Absorption Cross Sections of Ozone
AOD	Aerosol Optical Density
AVDC	Atmospheric Validation Data Center
B&P	Ozone cross-section determined by Bass, A. M. and Paur, R. J., published in 1985.
B05	Ozone cross section in the reevaluation of the Dobson by Berhard 2005
BIRA-IASB	Belgian Institute for Space Aeronomy
BOp	The official cross-section used to determine the absorption coefficients for Brewer
Cal/Val	Calibration and Validation
CCN	Contract Change Notice
CEOS	Committee on Earth Observation Satellites
CINDI	Cabauw Intercomparison of Nitrogen Dioxide Measuring Instruments
DBM	Ozone cross-section data determined by Daumont, D; Brion, J, and Malicet, J
DBML	DMB ozone cross-sections expressed as quadratic polynomial approximation in temperature at each wavelength registration, determined by Liu et al. (2007)
DBMQ	DMB ozone cross-sections expressed as quadratic polynomial approximation in temperature at each wavelength registration.
DOAS	Differential Optical Absorption Spectroscopy
DQ	Data quality
DQP	Data quality parameter
DXS	Differential Cross-Section
ENVISAT	Environmental Satellite
EO	Earth Observation
ERS-2	European Remote Sensing Satellite-2
ESA	European Space Agency
ESRIN	European Space Research Institute
EUMETSAT	European Organisation for the Exploitation of Meteorological Satellites
EVDC	Earth Observation Validation Data Center
FP7	Seventh Framework Preogramme of the European Commission
GAW	Global Atmospheric Watch
GEO	Geostationary orbit
GEOMS	Generic Earth Observation Metadata Standard
GOME	Global Ozone Monitoring Experiment
IGACO	Integrated Global Atmospheric Chemistry Observations
IGQ4	B&P cross-section data base published on the IGACO website

IO3C	International Ozone Commission
IUP	Ozone cross-section data base determined by the Institute of Environmental Physics, University of Bremen at ten temperatures per wavelength registration (HARMONICS)
IUPQ	The IUP ozone cross-section expressed as quadratic polynomial approximation in temperature at each wavelength registration.
LIDORT	Linearised Discrete Ordinate Radiative Transport
MAXDOAS	Multi-Axis DOAS
METOP	Meteorological Operational satellite programme
MOHp	Meteorological Observatory Hohenpeissenberg
NASA	National Aeronautics and Space Administration
NDACC	Network for the Detection of Atmospheric Composition Change
NO_2	Nitrogen dioxide
O_3	Ozone
OEM	Optimal Estimation Method
OMI	Ozone Monitoring Instrument
Pandora	Pandora spectrometer system
QA/QC	Quality Assessment/Quality Control
RBCC-E/RDCC.E	Regional Brewer Calibration Center/Regional Dobson Calibration Center
SAOZ	Système d'Analyse par Observations Zénithales
SCD	Slant Column Density
SCIAMACHY	SCanning Imaging Absorption spectroMeter for Atmospheric CartograpHY
SOW	Statement of Work
SZA	Solar Zenith Angle
TOC	Total Ozone Content
TOMS	Total Ozone Mapping Spectrometer
VCD	Vertical Column Density
WCWG	CEOS Working Group on Calibration and Validation
WMO	World Meteorological Office
WOUDC	World Ozone and Ultraviolet Data Center
wRMS	Normalized root mean square of weighted spectral fitting residuals

2.3 Applicable documents

[AD1] CEOS Intercalibration of Ground-Based Spectrometers and Lidars, Proposal in response to ESRIN/RFQ/3-12340/08/I-EC (ref. this proposal).

[AD2] ESA/ESRIN Statement of Work, ref. SOW: CEOS Intercalibration of ground-based spectrometers and lidars, GMES-CLVL-EOPG-SW-08-0002.

[AD3] Draft Contract, Appendix 2 to ESRIN/RFQ/3-12340/08/I-EC

[AD4] ESA/ESRIN Statement of Work: Inter-calibration of ground-based spectrometers and Lidars - Extension 2012-2013, GMES-CLVL-EOPG-SW-12-0002, 27/09/2012

[AD5] Inter-calibration of ground-based spectrometers and Lidars – Minispectrometer Intercalibration and Satellite Validation [Statement of Work], Issue 1, Revision 0, GMES-CLVL-EOPG-SW-13-0001, 15 January 2013

[AD6] Inter-calibration of ground-based spectrometers and Lidars – Minispectrometer Intercalibration and Satellite Validation [Proposal], Contract: 22202/09/I-EC, RFQ/3-12340/08/I-EC, 22 January 2013

2.4 Reference Documents

[RD1] Vicarious Calibration and Geophysical Validation Functional Baseline, GMES-SPPA-EOPG-TN-06-0001.

[RD2] ENVISAT Calibration and Validation Plan, PO-PL-ESA-GS-1092.

[RD3] IGOS – Integrated Global Observing Strategy: Atmospheric Chemistry, http://ioc.unesco.org/igodpartners/atmosphere.htm

[RD4] CEOS – Working Group on Calibration and Validation: Satellite missions/ Atmospheric Chemistry, http://www.oma.be/NDSC_SatWG/Documents/SatelliteMissionsPlanning(30 Nov2007)_A4.pdf

[RD5] Inter-calibration of ground-based spectrometers and Lidars – Minispectrometer Intercalibration and Satellite Validation, Report 1: List of Minispectrometers considered in this activity, 10 April 2013

[RD6] Inter-calibration of ground-based spectrometers and Lidars – Minispectrometer Intercalibration and Satellite Validation, Report 2: Recommendations for Inter-Calibration of minispectrometer networks, 25 September 2013

[RD7] Inter-calibration of ground-based spectrometers and Lidars – Minispectrometer Intercalibration and Satellite Validation, Report 3: Mid-term progress report, 1 December 2013

[RD8] Inter-calibration of ground-based spectrometers and Lidars – Minispectrometer Intercalibration and Satellite Validation, Report 4: Minispectrometer Data Quality Report, 1 December 2013

[RD9] Inter-calibration of ground-based spectrometers and Lidars – Minispectrometer Intercalibration and Satellite Validation, Report 5: Minispectrometer Validation Data, 1 December 2013

[RD10] Inter-calibration of ground-based spectrometers and Lidars – Minispectrometer Intercalibration and Satellite Validation, Report 6: Validation protocol, 1 December 2013

[RD11] Inter-calibration of ground-based spectrometers and Lidars – Minispectrometer Intercalibration and Satellite Validation, Report 7: Validation Report, 25 January 2014.

3 Extension of Brewer calibrations and effect of ozone cross-section change (WP 1)

3.1 Absolute Calibration of the RBCC-E Reference Instruments

The RBCC-E Brewer triad comprises three double monochromator instruments: the absolute standard Brewer#157, the experimental unit Brewer#183 and the travelling standard Brewer#185. The stability of the RBCC-E travelling standard is checked before and after every campaign by comparison with all the members of the triad, and, if possible, by performing Langley plots.

During the reporting period, developing and testing of a method for the analysis of routine absolute calibrations of the RBCC-E reference instruments at Izaña has been continued, focusing on improved quality controlled automated processing of Langley plots. We have dealt with two different approaches to the analysis of Langley plots, using both Dobson and Brewer algorithms. As reported in previous reports, we have confirmed the similarities in results obtained through both methods.

Next in Figure 3.1 and Figure 3.2 we show the corresponding results for all the RBCC-E triad members during the 2013, highlighting the dates of each campaign (vertical thick red lines) as well as the operational calibration constants (horizontal black lines). For both Brewer #157 and #183 the Langley confirmed the operational constant during the reporting period within ±5 units, which is the accepted tolerance range. Note that 5 units change in ETC means less than 0.3% in ozone change, depending on the air mass range (lower variations corresponding to higher air masses).

The linear regression is performed on the [1.15 - 4.25] air mass range, using the Brewer astronomical formulas for the air mass determination and further splitting each clear day with constant ozone into morning and afternoon Langley events. We have worked with the individual direct-sun ozone measurements (DS) fulfilling the following criteria:

1. The individual direct sun ozone observations are performed 5 times in 3.5 minutes.
2. The ozone column and standard deviation is computed on such a group of five individual DS measurements. Data are accepted if the standard deviation is lower than 2.5 DU (Brewer cloud-screening method).
3. The number of such individual DS data must be at least 100 (i.e. 20 sequences of 5 observations).

We have computed ETC monthly means using both AM as well as PM results Langley results. To estimate the accuracy of these monthly values we calculate the standard error of the mean, defined as $sem = \mathrm{SD} / \sqrt{\mathrm{N}}$, where SD and N are the standard deviation and the size of the monthly sample, respectively. MS9 double ratios are corrected for non-neutrality effects of ND filters in the case of Brewer#185. We currently have not stated a definitive ozone calibration constant in the case of Brewer #185, due to some issue related to the temperature dependence of the instrument's response. Considerable progress has been made, as shown in Figure 3.3. It is remarkable to note the ability of Langley plots to adequately capture changes in the instrument's response.

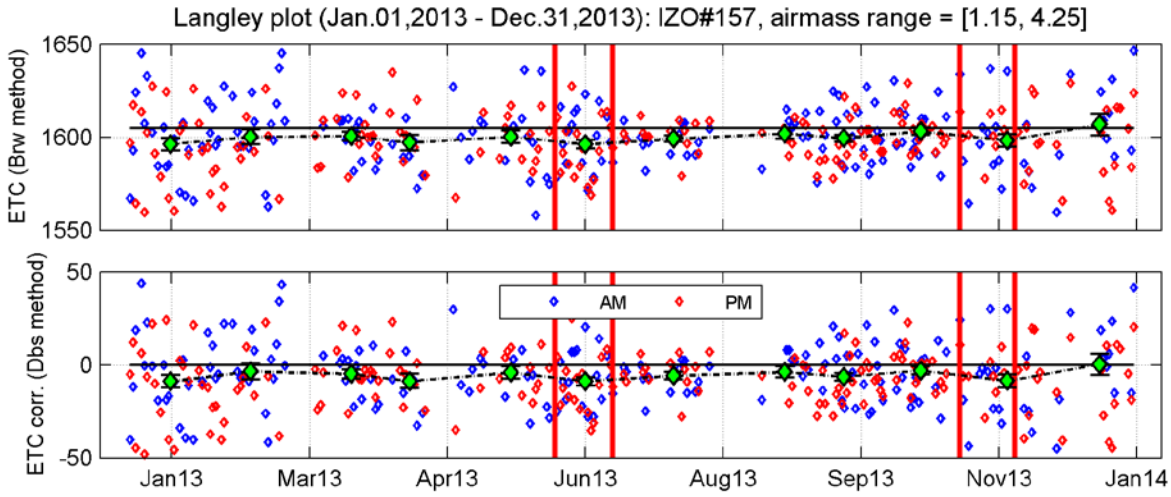

Figure 3.1: Langley ETC calculation at IZO before and after the campaign. The blue (red) diamonds correspond to Langley results derived from AM (PM) filtered data. The green diamond error bars (+/-1 sem) are monthly means of both AM and PM Langley results. The horizontal black solid line indicates the operational ETC constant for Brewer #157. We show two different methods of Langley analysis: ordinary Least Squares (top) and the Dobson regression 1/m (bottom).

Brewer IZO#157	ETC	sem	ETC corr. (Dobson)	sem (Dobson)	N	ETC Op.
15-Jan-2013	1596	3	-9	3	42	1605
13-Feb-2013	1600	4	-4	4	28	1605
22-Mar-2013	1601	2	-5	2	27	1605
12-Apr-2013	1597	4	-9	4	19	1605
19-May-2013	1600	3	-4	3	26	1605
15-Jun-2013	1596	2	-9	2	43	1605
17-Jul-2013	1599	2	-6	2	24	1605
26-Aug-2013	1602	3	-4	3	11	1605
16-Sep-2013	1599	2	-7	2	47	1605
14-Oct-2013	1603	2	-3	2	39	1605
14-Nov-2013	1598	3	-9	4	30	1605
18-Dec-2013	1607	6	0	6	27	1605

Table 3.1: Langley monthly mean extraterrestrial constant for the Brewer #157 obtained by two different methods: OLS ordinary Least Square and the Dobson regression 1/m.

In the case of Brewer #185 we currently have not stated a definitive ozone calibration constant, due to some issue related to the temperature dependence of the instrument's response. Considerable progress has been made, as shown in Figure 3.3. It is remarkable the ability of Langley plots to adequately capture changes in the instrument's response.

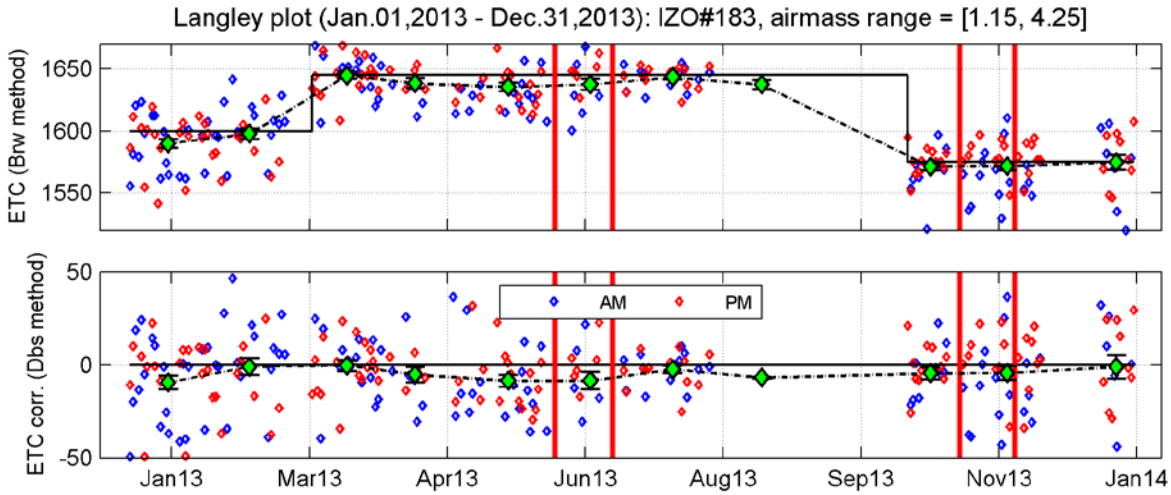

Figure 3.2: Langley ETC calculation at IZO before and after the campaign. The blue (red) diamonds correspond to Langley results derived from AM (PM) filtered data. The green diamond error bars (+/-1 sem) are monthly means of both AM and PM Langley results. The horizontal black solid line indicates the operational ETC constant for Brewer #183. We show two different methods of Langley analysis: ordinary Least Squares (top) and the Dobson regression 1/m (bottom).

Brewer IZO#183	ETC	sem	ETC corr. (Dobson)	sem (Dobson)	N	ETC Op.
14-Jan-2013	1590	4	-9	4	37	1600
13-Feb-2013	1598	5	-1	5	24	1600
20-Mar-2013	1645	3	-0	3	29	1645
14-Apr-2013	1638	4	-5	4	18	1645
18-May-2013	1635	3	-9	3	29	1645
16-Jun-2013	1638	5	-9	5	17	1645
16-Jul-2013	1643	2	-2	2	21	1645
18-Aug-2013	1637	4	-7	1	2	1645
18-Oct-2013	1571	3	-5	3	24	1575
15-Nov-2013	1571	4	-4	4	32	1575
24-Dec-2013	1575	6	-1	6	17	1575

Table 3.2: Langley monthly mean extraterrestrial constant for the Brewer #183 obtained by two different methods: OLS ordinary Least Square and the Dobson regression 1/m.

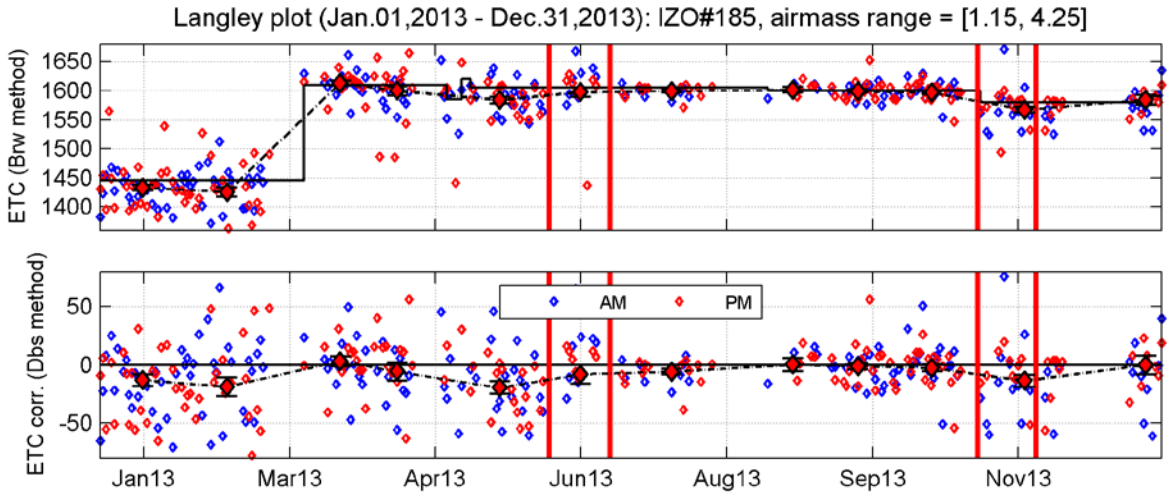

Figure 3.3: Langley ETC calculation at IZO before and after the campaign. The blue (red) diamonds correspond to Langley results derived from AM (PM) filtered data. The green diamond error bars (+/-1) are monthly means of both AM and PM Langley results. The horizontal black solid line indicates the operational ETC constant for Brewer #185. We show two different methods of Langley analysis: ordinary Least Squares (top) and the Dobson regression 1/m (bottom).

Brewer IZO#185	ETC	sem	ETC corr. (Dobson)	sem (Dobson)	N	ETC Op.
15-Jan-2013	1433	5	-13	5	49	NaN
13-Feb-2013	1425	8	-19	8	42	
24-Mar-2013	1613	4	3	4	24	
12-Apr-2013	1599	8	-6	8	34	
18-May-2013	1584	6	-20	5	36	
14-Jun-2013	1598	8	-8	8	25	
16-Jul-2013	1599	2	-6	2	20	
26-Aug-2013	1602	5	0	6	6	
18-Sep-2013	1599	2	-1	3	36	
13-Oct-2013	1596	3	-3	3	39	
14-Nov-2013	1567	5	-14	5	35	
25-Dec-2013	1584	9	-0	8	18	

Table 3.3: Langley monthly mean extraterrestrial constant for the Brewer #183 obtained by two different methods: OLS ordinary Least Square and the Dobson regression 1/m.

3.1.1 RBCC-E Intercomparison Campaigns

Two intercomparisons campaigns have been held during the last year. The eighth RBCC-E campaign was held at El Arenosillo, Spain, during the period 10-20 June, 2013. The ESA CAL-VAL project-specific Nordic campaign was held at the Izaña Observatory during the period 30 October to 19 November, 2013. We used the RBCC-E triad member Brewer #183 as a reference instrument.

The results obtained from analysis of Langley plots performed at IZO station before and after the campaign confirmed the calibration constant transferred during the intercomparisons.

3.1.1.1 *EL Arenosillo* Campaign, June 2013

In Figure 3.4, we show near-simultaneous ozone relative differences of RBCC-E triad members with respect to the mean of the three instruments for a period of 20 days before (May 13 – June 2, 2013) and after (June 25 – July 15, 2013) the El Arenosillo 2013 campaign. No change is observed in responses of Brewer #157 and #183, whereas some slight change in ETC constant can be deduced in the case of Brewer#185. In any case, the instrument deviations are within 0.25% for both periods.

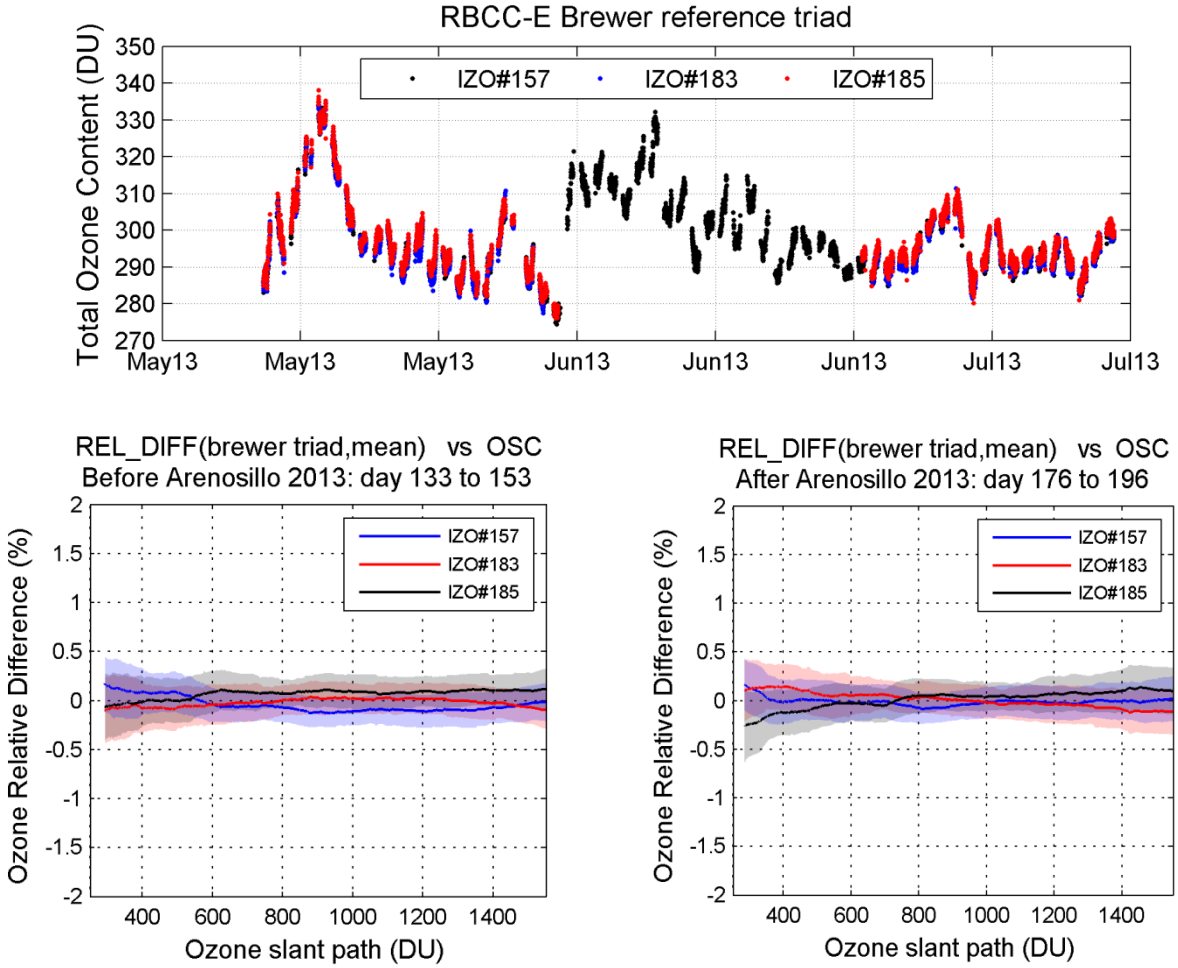

Figure 3.4: Near-simultaneous ozone ratios of RBCC-E standard Brewers (serial no. #157, #183 and #185) to the mean of all instruments are shown before (left) and after (right) the El Arenosillo 2013 intercomparison.

	#157	#183	#185	Nobs
Before Are2013 Campaign	0.1 +/- 0.23	-0.1 +/- 0.24	0.1 +/- 0.25	695
After Are2013 Campaign	0.0 +/- 0.26	0.1 +/- 0.30	-0.1 +/- 0.30	1105

Table 3.4: Statistics of RBCC-E standard Brewers (serial no. #157, #183 and #185) comparisons to the mean of all instruments as obtained during the El Arenosillo 2013 intercomparison.

3.1.1.2 *Izaña* Campaign, Oct-Nov 2013

We show in Figure 3.5 near-simultaneous ozone relative differences of RBCC-E triad members with respect to the mean of the three instruments for a period of 20 days before and after (Oct10 – Dec07, 2013) the campaign. The agreement during this period is very good between the reference instruments Brewer #157 and #183. In opposition, the Brewer #185 changed significantly its response to light just

before the intercomparison (Day 302, 29 of October), due to the replacement of the internal mercury lamp.

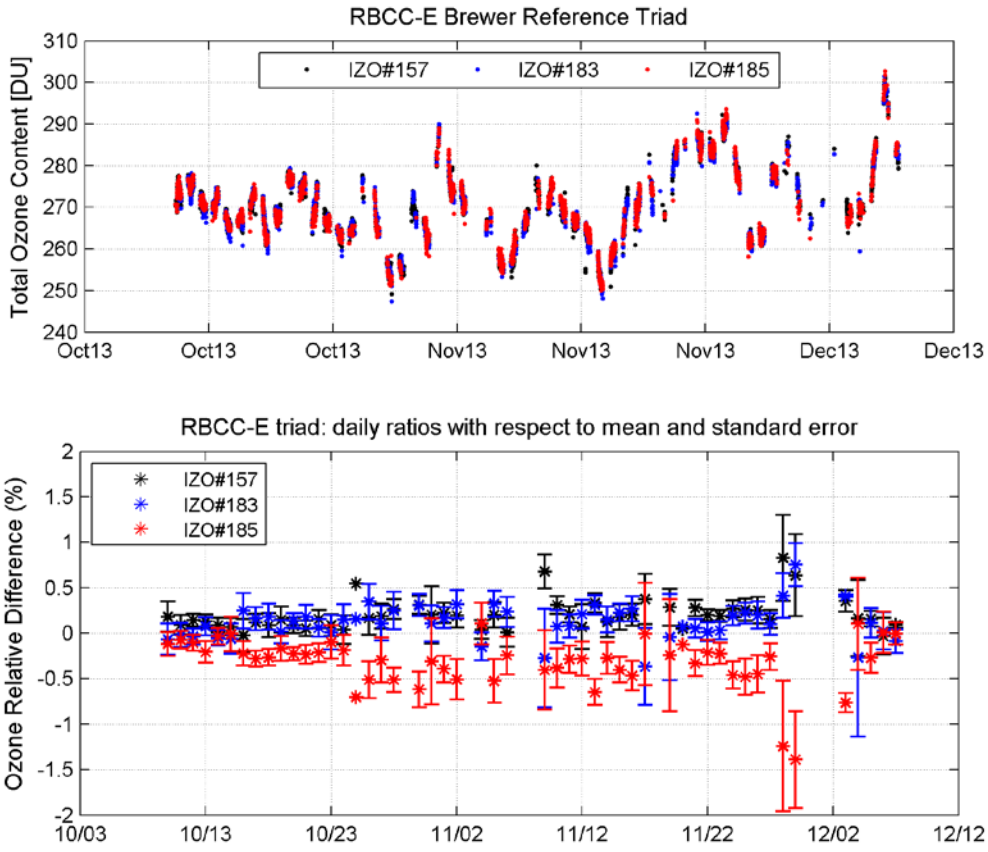

Figure 3.5: Near-simultaneous ozone ratios of RBCC-E standard Brewers (serial no. #157, #183 and #185) to the mean of all instruments during the period October – December 2013.

	IZO#157	**IZO#183**	**IZO#185**	**mean osc**
All osc	0.2 +/-0.31	0.1 +/-0.36	-0.3 +/-0.4	645.4 +/-34
osc <700	0.2 +/-0.28	0.2 +/-0.32	-0.5 +/-0.3	454.1 +/-94
700<osc<1000	0.1 +/-0.26	0 +/-0.26	-0.1 +/-0.3	821.1 +/-86
osc>1000	0 +/-0.38	-0.2 +/-0.3	0.2 +/-0.32	1341.4 +/-2

Table 3.5: Statistics of RBCC-E standard Brewers comparisons to the mean of all instruments during the period October – December 2013.

3.1.2 Standard Instruments Intercomparison

Two reference standards routinely used for ozone calibration scale transfer to instruments in the world network were operated during the *El Arenosillo 2013* intercomparison campaign: the single-monochromator Brewer #017 (International Ozone Service, IOS, EC) and the double-monochromator Brewer #158 (Kipp & Zonen, manufacturer of the Brewer).

The Brewer #017 response changed by more than 2% in ozone during the intercomparison days (Figure 3.6, top). This change in instrument's response was related to changes in standard lamp R6 ratio (around 30 units during the intercomparison days, same Figure, bottom). We observed a very good agreement between both IOS#017 and IZO#183 during the first day of the campaign (Julian day 161), but then the comparison got worse, with ozone differences larger than -2%. Finally, after applying the change in standard lamp ratio to Brewer #017 calibration constants, we achieved an overall improvement of Brewer's response for the whole intercomparison days, but still with ozone deviations on the order of -1% for osc lower than 800 DU.

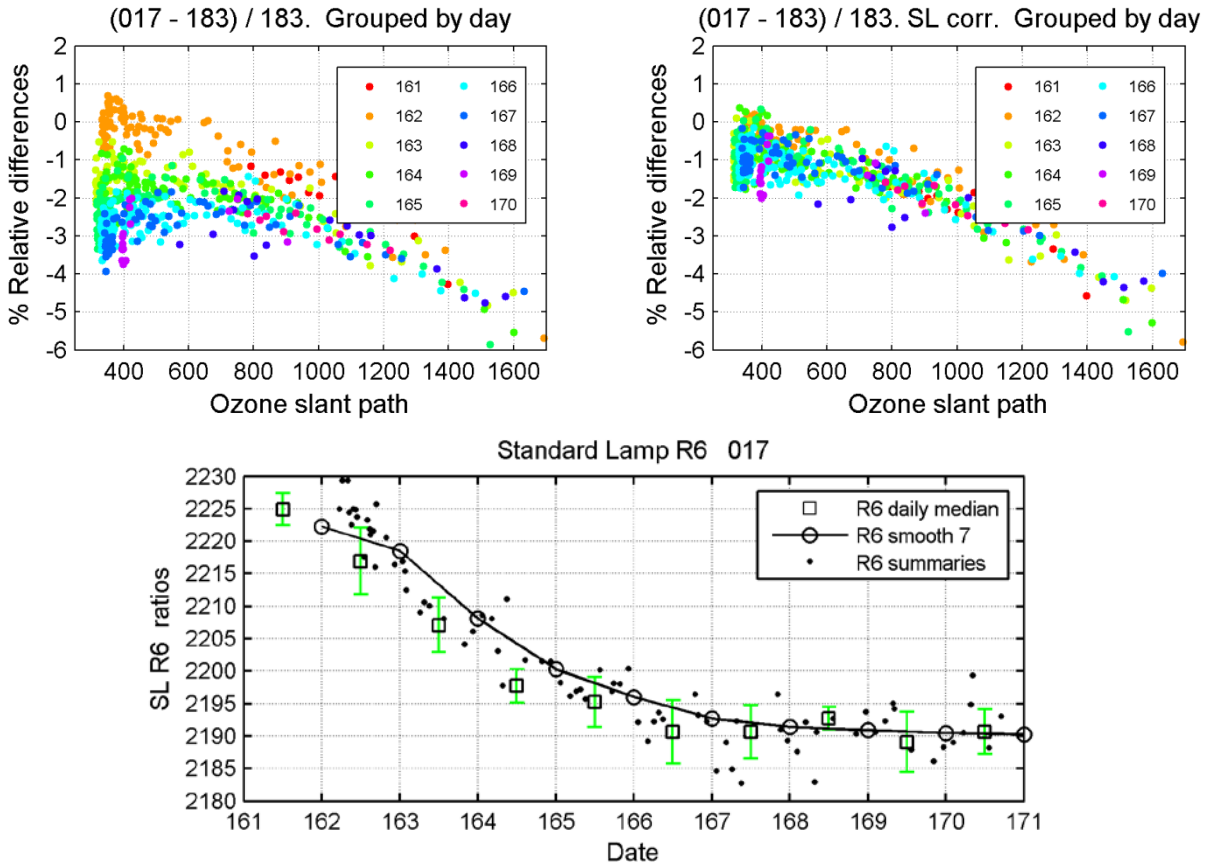

Figure 3.6: Near-simultaneous direct sun ozone column percentage differences between travelling standard Brewer IOS#017 and RBCC-E reference Brewer#183, grouped by Julian day, as a function of ozone slant path (top) and standard lampR6 ratio series (bottom) during the intercomparison days. We show Brewer#017 ozone data with (top, right) and without (top, left) SL correction.

In the case of the Brewer #158 the standard lamp R6 ratio was quite stable during the campaign days (see Figure 3.7, bottom), which points also to the instrument's response being stable during the intercomparison (same Figure, top). However, the operational calibration constants (no SL corrected) resulted in ozone deviations of the order of +1%, on average. The comparison with RBCC-E standard Brewer #183 improved after applying the SL correction to the ozone calibration constant. Even in this case, ozone measurements obtained from Brewer #158 were of the order of 0.5-1% higher as compared to Brewer #183 ozone data.

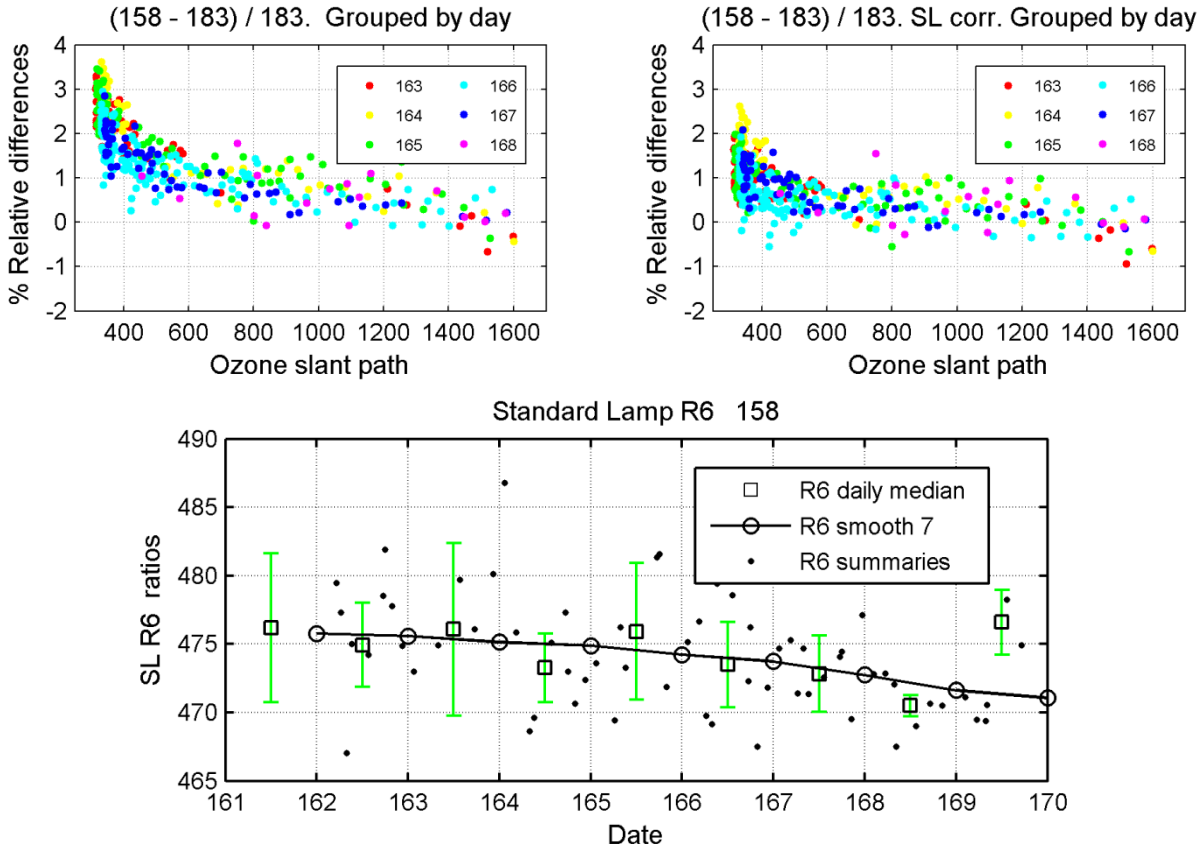

Figure 3.7: Near-simultaneous direct sun ozone column percentage differences between travelling standard Brewer K&Z#158 and RBCC-E reference Brewer IZO#183 grouped by Julian day as a function of ozone slant path (top) and standard lampR6 ratio series (bottom) during the intercomparison days. We show Brewer#158 ozone data with (top, right) and without (top, left) SL correction.

In summary, we observed ozone deviations or the order of +/-1% between standard instruments which are routinely used for ozone transfer calibration worldwide. For this to be true it is necessary to apply the SL correction to ozone data. However, this should be taken with care for most of instruments, or at least it is necessary to work with a precise standard lamp R6 reference value.

3.2 Regular *Regional Brewer Calibration Center-Europe* (RBCC-E) Intercomparison Campaign: El Arenosillo 2013

A total number of eighteen Brewer spectrophotometers from eight countries have participated in the intercomparison. These campaigns, with a large number of participants, provide an overview of the current state of ozone measurements being made by the European Brewer network. Apart from RBCC-E standards, two additional reference instruments were present at the campaign: single-monochromator Brewer #017 (IOS, EC) and double-monochromator Brewer#158 (K&Z). The instruments were compared with the RBCC-E standard Brewer#183 for ozone and with the European UV reference from the World Radiation Center (QASUME unit) for UV. For this report we used our own calibration constants obtained by Langley plots at IZO.

Figure 3.8: Participants in the eighth RBCC-E intercomparison campaign, *El Arenosillo* 2013.

3.2.1 The Intercomparison Conditions

We collected during the campaign in average 500 direct sun ozone simultaneous measurements with the reference instrument, most of them (≈85%) within the 300-600 DU ozone slant path range. The lower number of near-simultaneous ozone measurements was around 250. Total ozone content values at *El Arenosillo* station during the intercomparison ranged between 200 to 400 DU. This campaign was characterized by high internal temperatures, with maximum ≈45ºC for some of the participant instruments. We show in Figure 3.9 different useful parameters related to the intercomparison conditions.

3.2.2 Blind Comparison

The blind comparison gives us an idea of the initial status of the instrument, i.e., how well the instrument performed using the original calibration constants (those operational at the instrument's station).

The Standard Lamp (SL) test is used to track the spectral response of the instrument and therefore the ozone calibration. The ozone is corrected assuming that changes in R6 are related to changes in the ETC constant. In this case the ETC constant is corrected by the observed change in the standard lamp R6 ratio as $ETC_{new} = ETC_{old} - (SL_{ref} - SL_{measured})$. This procedure constitutes the so called Standard Lamp

Correction. The comparison with a reference standard instrument is the only tool to assess whether the SL R6 ratio change is related or unrelated with changes in the instrument's response.

Only 8 out of 18 instruments agreed (on average) within +/-10 units (≈1% in ozone) with the corresponding R6 reference value (see Figure 3.10). On the other hand, the blind-days comparison shows rather poor results for the comparison with the reference Brewer #183, with ozone deviations within +/-1% for only 8 out of 18 instruments. In most cases, the SL correction did not improve the comparison (see Figure 3.11).

Institution	**Name**	**Instrument**	**Country**
RBCC-E AEMET	Alberto Redondas Juan José Rodríguez Virgilio Carreño	Brewer #183-MKIII Brewer #185-MKIII	Spain
IOS	Ken Lamb V. Savastiouk Martin Stanek	Brewer #017-MKII	Canada Czech Republic
Kipp & Zonen	David Godoy Keith M. Wilson	Brewer #158-MKIII	Netherland
INTA	Jose Manuel Vilaplana	Brewer #150-MKIII	Spain
AEMET	J.R. Moreta González. Daniel Moreno J.M San Atanasio Angel Miguel Boned Francisco Escribá Francisco García	Brewer #070-MKIV Brewer #186-MKIII Brewer #166-MKIV Brewer #117-MKIV Brewer #151-MKIV	Spain
ONM	Ouchene Bouziane Ferroudj Mohammed Salah	Brewer #201-MKIII	Algeria
UKMO	John Rimmer Peter Kelly	Brewer #075-MKIV Brewer #126-MKII Brewer #172-MKIII	U.K.
DMN	Hamza Rachidi Mohammed Jamaleddine Abdelkarim Faquih	Brewer #051-MKII Brewer #165 - MKIII	Morroco
WRC	Luca Egli Christian Thomann	Brewer #163-MKIII QUASUME	Switzerland
KMA	JungMi Lee Young Suk You Yun Gon Lee	Brewer #095-MKII	Korea

Table 3.6: El Arenosillo 2013 intercomparison campaign participating instruments.

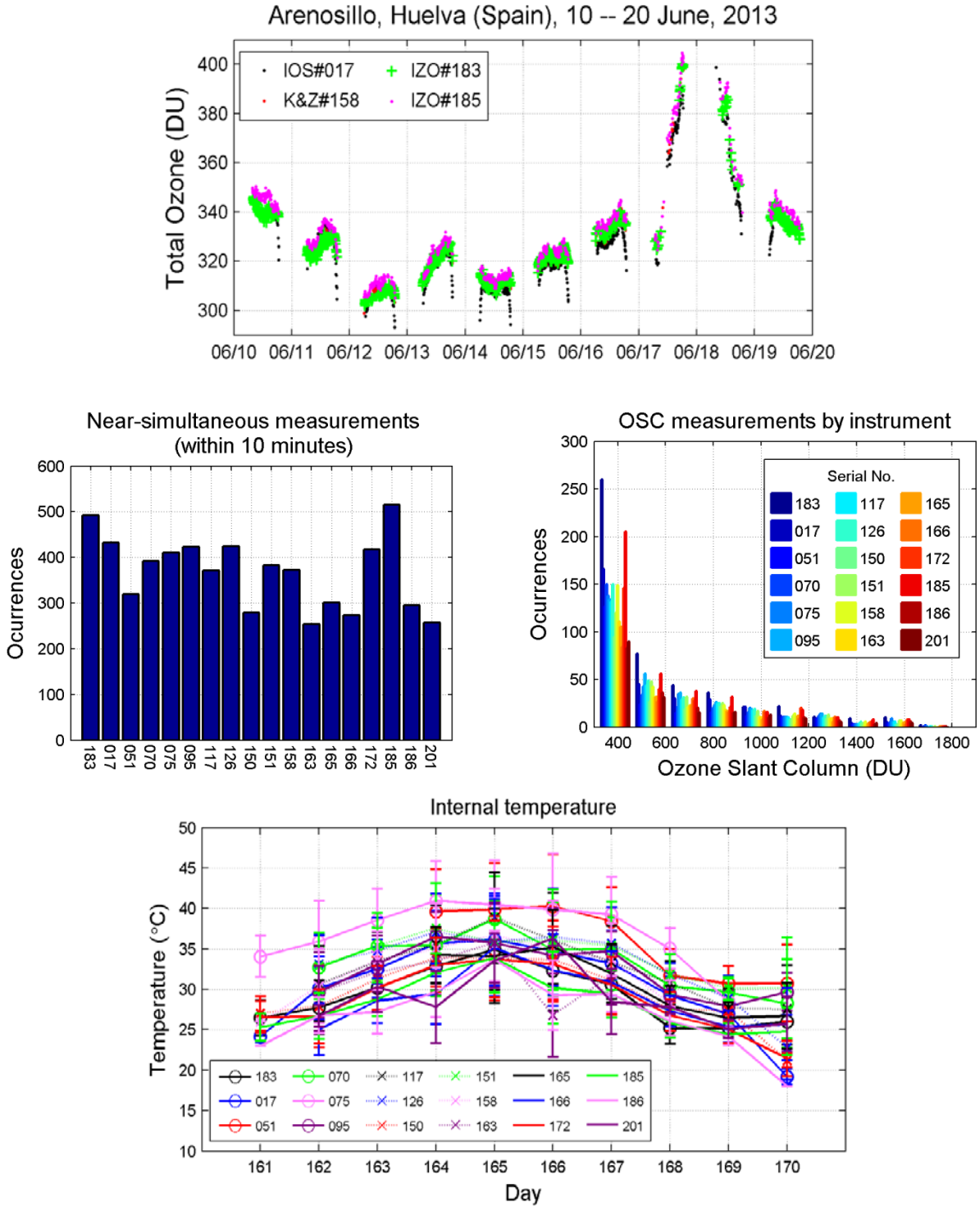

Figure 3.9: Statistics of the intercomparison conditions.

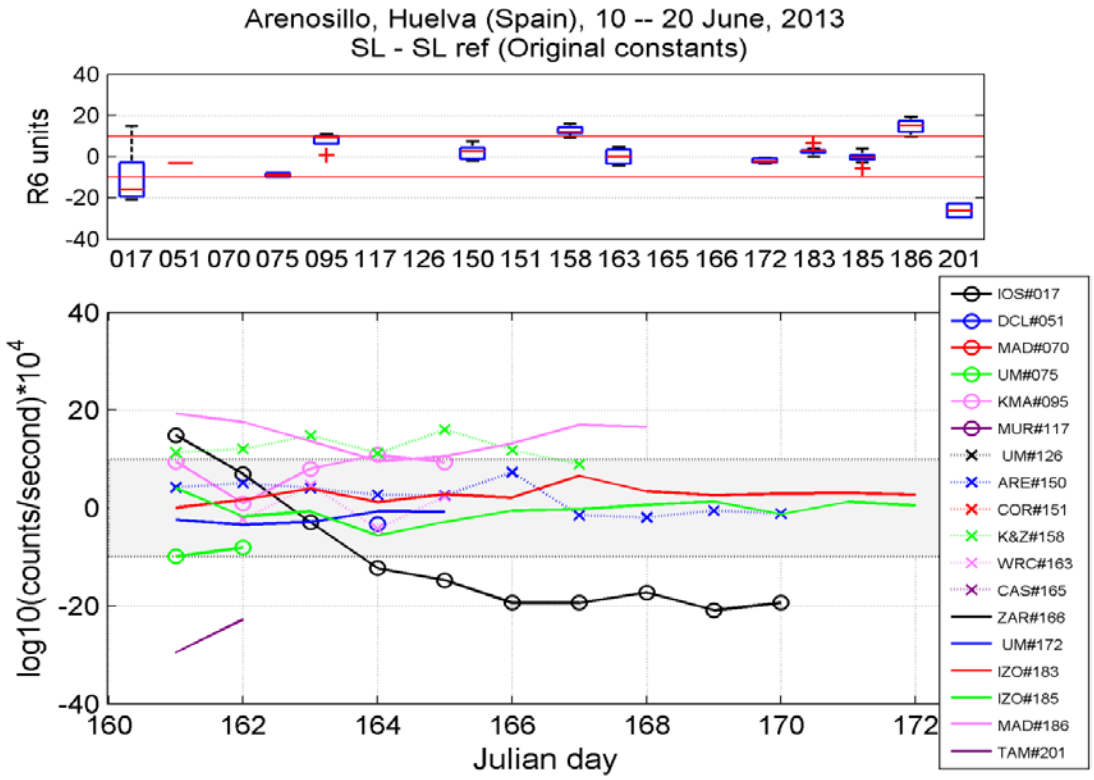

Figure 3.10: Standard lamp R6 difference to R6 reference value from last calibration during the blind days, before the maintenance. Data is grouped by Brewer serial number (above) and as a function of time (below). Missing instruments are off-scale. Variations of the order of +/- 10 units (~1% in ozone) are considered normal, whereas larger changes would require further analysis of the instrument performance.

3.2.3 Final Comparison

We used ozone data after the maintenance (final-days) to perform the ozone final calibration for all the participating instruments. The standard lamp R6 value recorded during the final days is normally adopted as the new SL reference value. It is also expected that this parameter will not vary more than 5 units during the same period (see Figure 3.13).

All the participant instruments were calibrated using the 1-parameter ETC transfer method (thus, Ozone absorption coefficients were derived from the wavelength calibration). The two parameters calibration method is also used as a quality indicator.

Overall, we achieved a quite good agreement with the reference instrument Brewer#183 after the new calibration constants were applied (see Figure 3.12). Ozone deviations are found to be of the order of +/-0.5% for the ozone slant path region less affected by the stray light rejection (OSC<800 DU for most of single Brewers). Note that we used original constants for the standard instrument IOS#017.

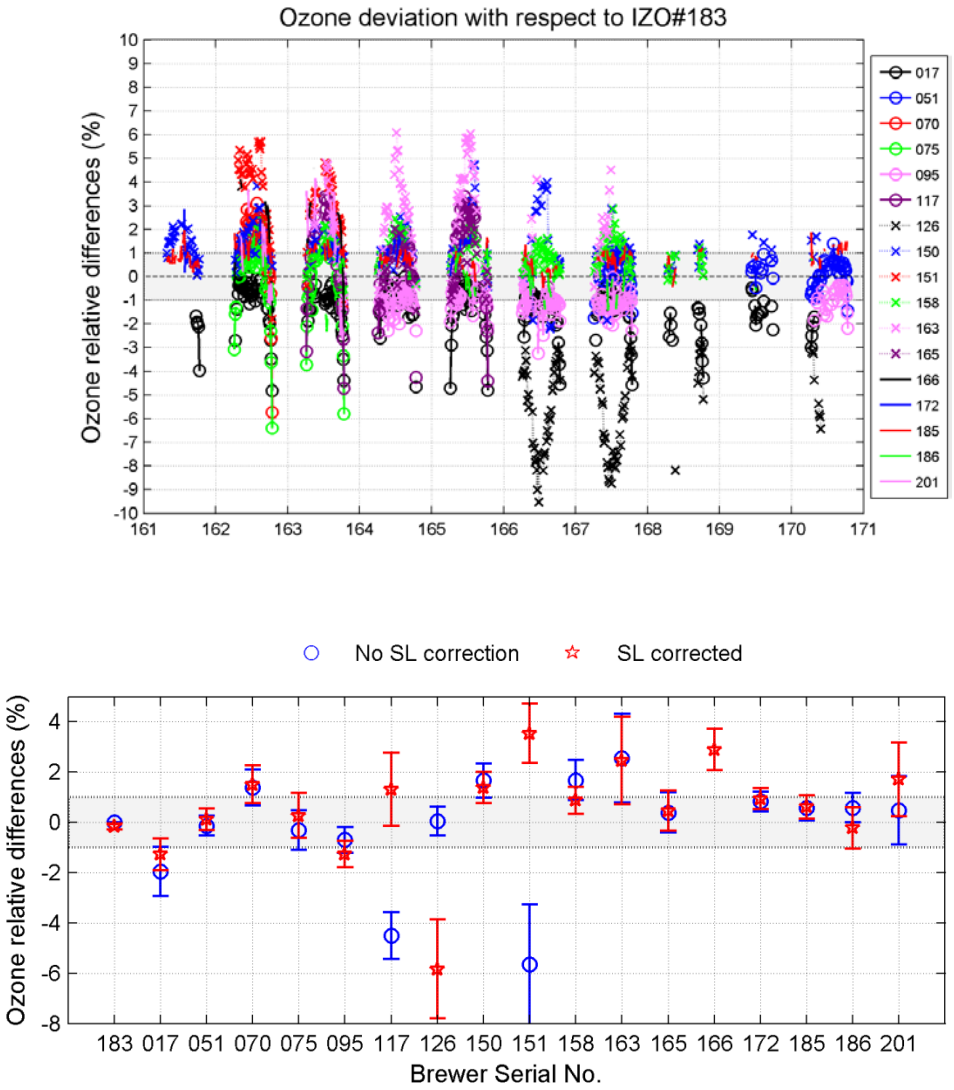

Figure 3.11: Blind-days ozone relative differences (percentage) of El Arenosillo 2013 participant instruments to RBCC-E travelling standard #183. Ozone measurements collected during the blind period (before the maintenance) are reprocessed using the original calibration constants, with (red plots) and without (blue plots) SL correction. Ozone deviations in bottom figure represent only the ozone slant column range not affected by the stray light rejection (OSC< 900 DU). The error bars represent the standard deviation of the mean.

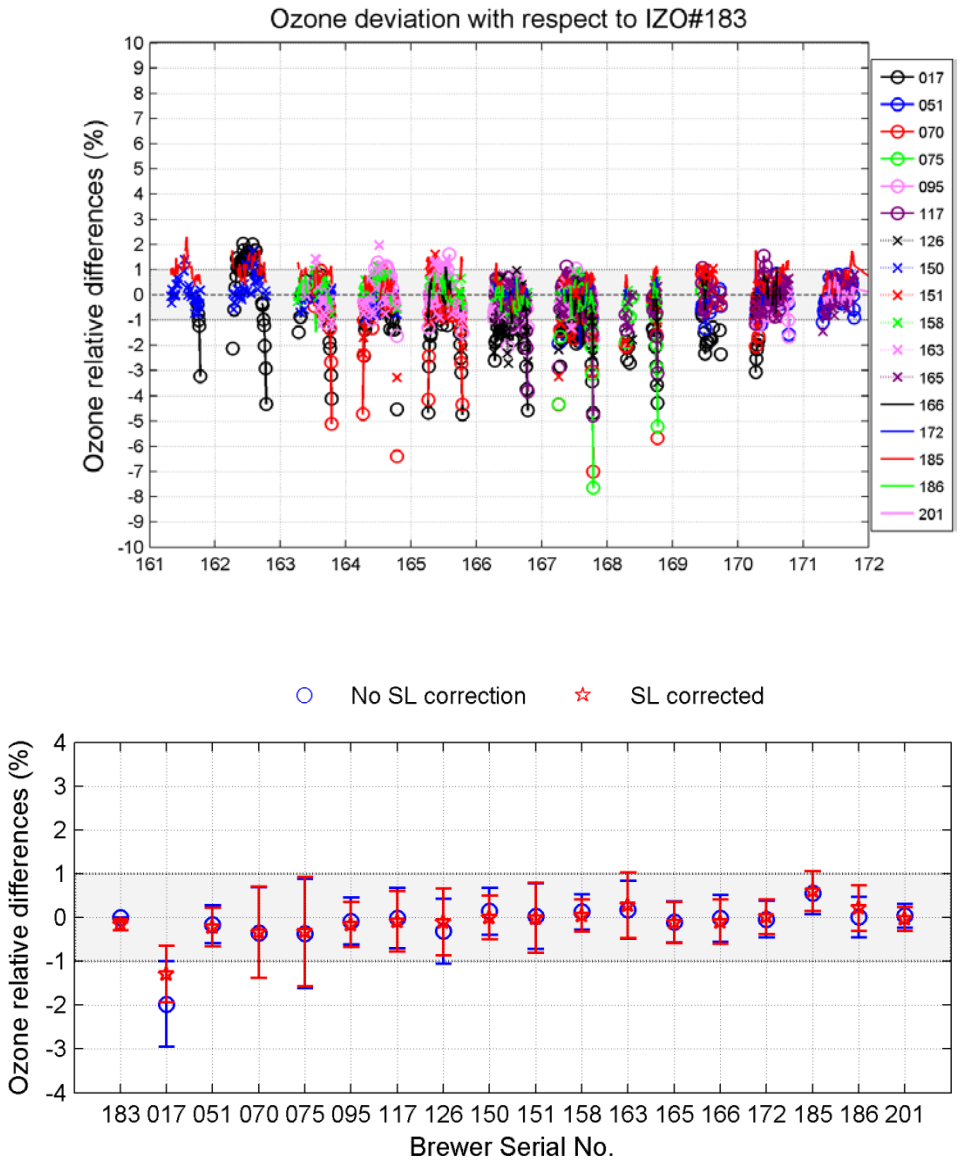

Figure 3.12: Final-days ozone relative differences (percentage) of El Arenosillo 2013 participant instruments to RBCC-E travelling standard #183. Ozone measurements collected during the final period (after the maintenance) are reprocessed using the final calibration constants, with (red plots) and without (blue plots) SL correction. The error bars represent the standard deviation of the mean. Ozone deviations in bottom figure represent only the ozone slant column range not affected by the stray light rejection (OSC< 900 DU). The error bars represent the standard deviation of the mean.

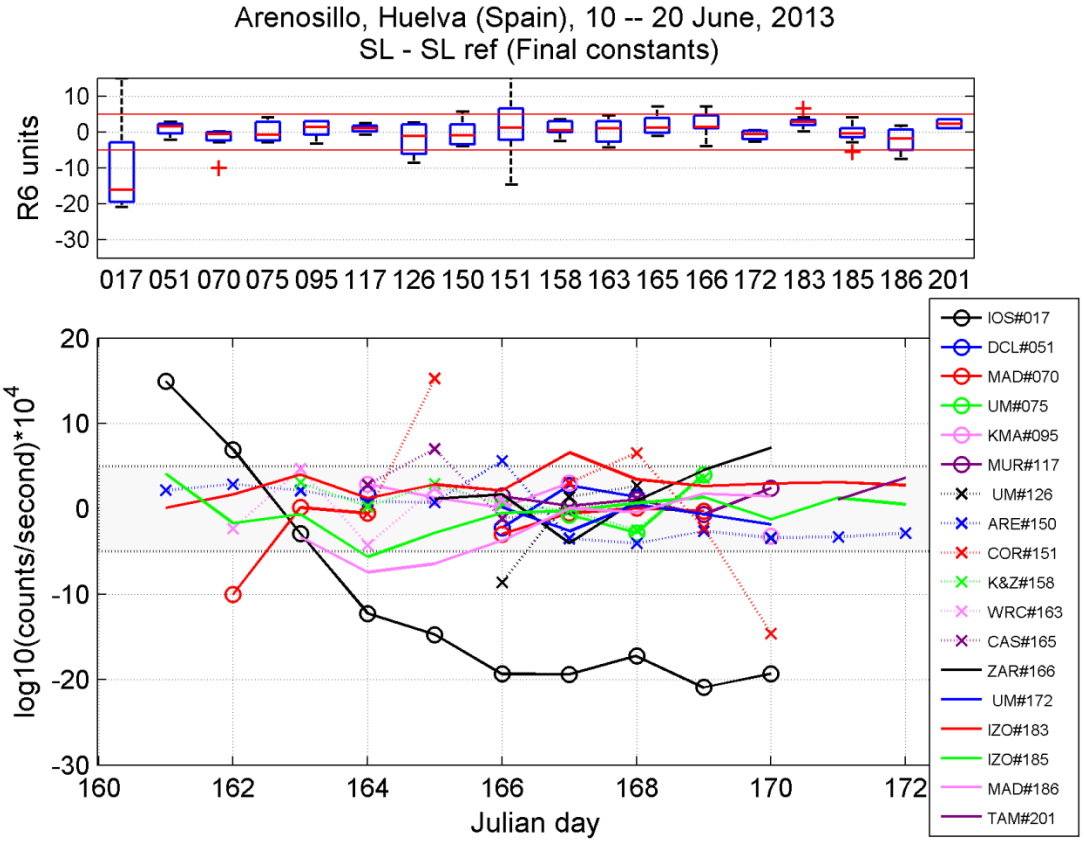

Figure 3.13: Standard lamp R6 ratio to R6 reference value from last calibration differences during the final days grouped by Brewer serial number (above) and as a function of time (below). The shaded area represents the tolerance range +/- 5 R6 units.

3.3 Nordic Campaign Activities: Izaña 2013

In this campaign, Brewer calibrated at high latitudes station during early spring conditions are compared to the RBCC-E triad members with the following main objectives

- Verify and compare the calibration performed at high ozone slant path conditions.
- Double against Single monochromators comparison.
- Characterization of the instruments at the Izaña Atmospheric Observatory (IZO) facilities.
- To perform direct irradiance calibration.
- To investigate the precision of the Langley Plot method.

Five Brewer spectrophotometers from high latitude stations have participated in the intercomparison. The instruments were compared with the RBCC-E standard Brewer#183 for ozone. We used our own calibration constants obtained by Langley plots at IZO.

Figure 3.14 : Participants of the Izaña campaign 2013

Institution	Name	Instrument	Country
RBCC-E AEMET	Alberto Redondas Juan José Rodríguez Virgilio Carreño Marta Sierra	Brewer #157-MKIII Brewer #183-MKIII Brewer #185-MKIII	Spain
FMI	Pauli Heikkinen Tomi Karppinen Juha M. Karhu	Brewer #037-MKII Brewer #214-MkIII	Finland
DMI	Paul Eriksen Nis Jepsen	Brewer #053-MKII Brewer #082-MKII Brewer #202-MKIII	Denmark

Table 3.7: Izaña 2013 intercomparison campaign: participating instruments.

We present next an overview of the main results obtained during the intercomparison, focusing in the initial status of the instruments during the first days of the intercomparison and in the performance of the final ozone calibration constants provided.

3.3.1 The Intercomparison Conditions

We collected during the intercomparison period ≈800 direct sun ozone measurements with the reference instrument (Brewer #183), most of them (≈70%) within the 400-600 DU ozone slant path range. The lower number of near-simultaneous ozone measurements was around 200 (Brewer #202). Total ozone content values at *Izaña* station during the intercomparison ranged between 250 to290 DU. The instrument's internal temperatures were quite stable during the intercomparison days, ≈20ºC for all the participant instruments with the exception of Brewer #082 who shows an obvious internal thermometer miss-calibration. We show in Figure 3.9 different useful parameters related to the intercomparison conditions.

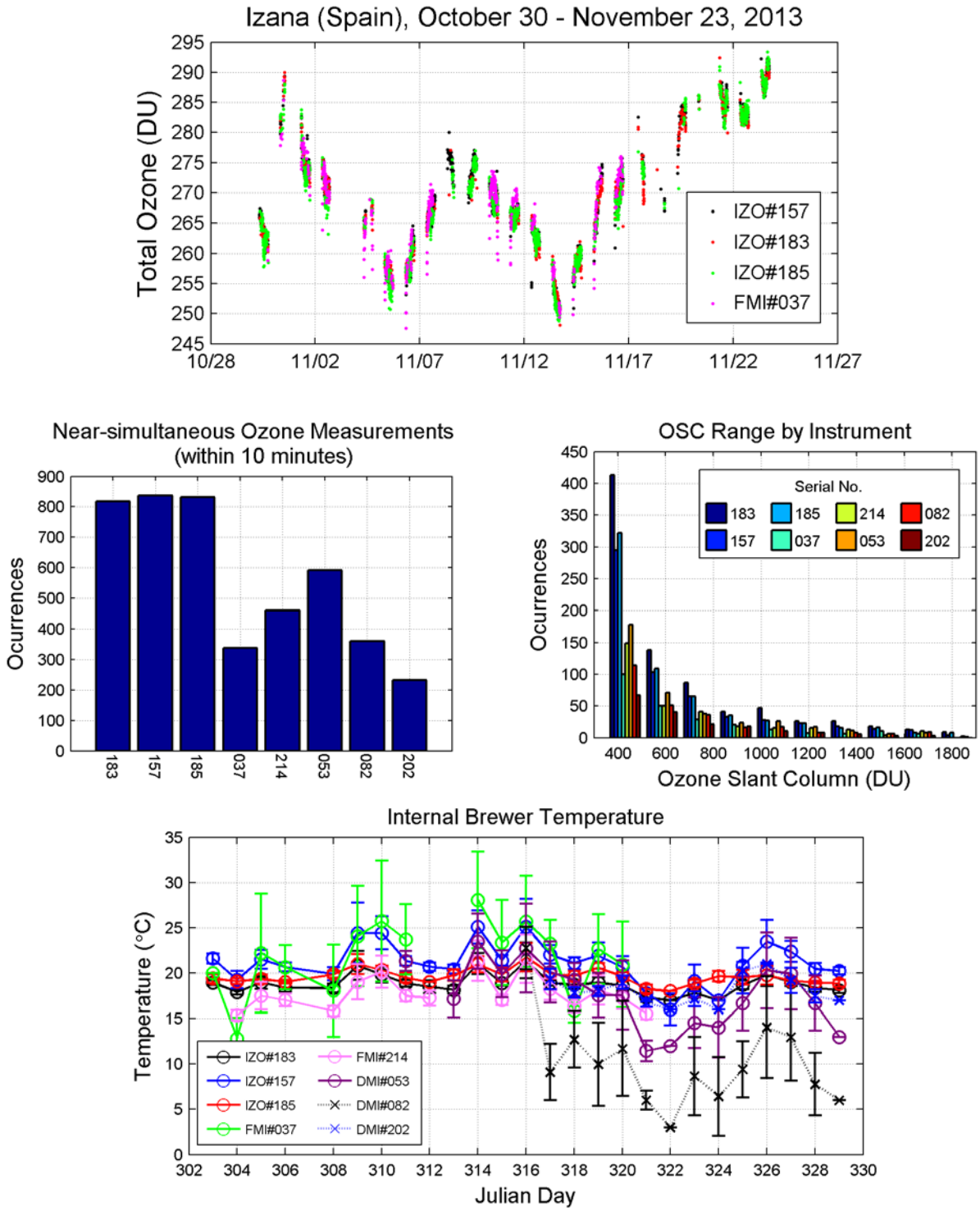

Figure 3.15: Statistics of the intercomparison conditions.

3.3.2 Blind Comparison

Apart from the RBCC-E triad members, only the Brewer #037 agreed within +/-10 units (≈1% in ozone) with the corresponding standard lamp R6 ratio reference value (see Figure 3.16). On the other hand, the blind-days comparison shows rather poor results for the comparison with the reference instrument Brewer #183: ozone deviations were found within +/-1% just for Danish Brewers #053 (we refer to here to the stray light free region in the case of single Brewer). Overall, the standard lamp correction did not improve the comparison with the reference instrument in the case of Finish Brewers, whereas the opposite was found to be true in the case of Danish instruments (see Figure 3.16).

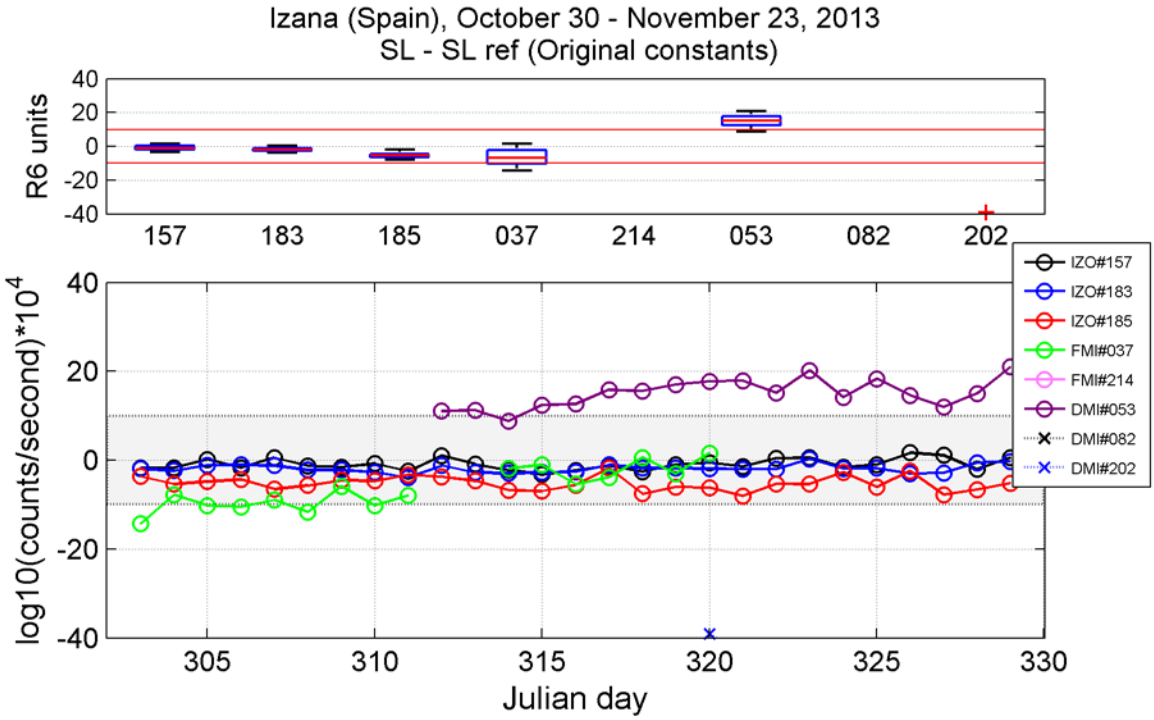

Figure 3.16: Standard lamp R6 difference to R6 reference value from last calibration during the blind days, before the maintenance. Data is grouped by Brewer serial number (above) and as a function of time (below).Variations of the order of +/- 10 units (~1% in ozone) are considered normal. Larger changes would require further analysis of the instrument performance.

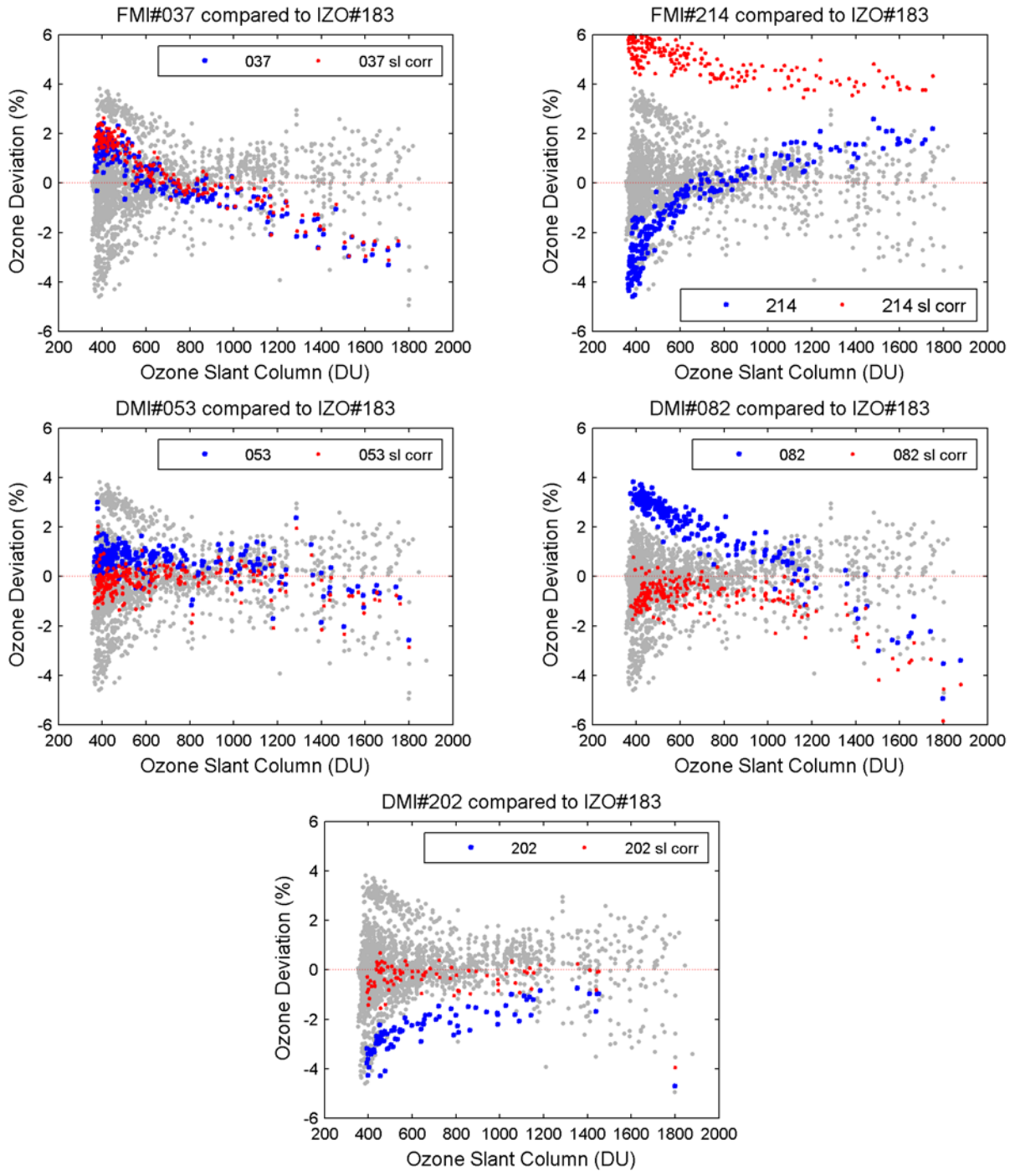

Figure 3.17: Blind-days ozone relative differences (percentage) of Izaña 2013 participant instruments to RBCC-E travelling standard Brewer #183. Ozone measurements collected during the blind period (before the maintenance) were reprocessed using the original calibration constants, with (red stars) and without (blue stars) standard lamp correction. Grey dots mean ozone deviations for all participating instruments.

3.3.3 Final Comparison

All the participant instruments were calibrated using the 1-parameter ETC transfer method (thus, Ozone absorption coefficients were derived from the wavelength calibration). The two parameters calibration method is also used as a quality indicator. All the instruments were reasonably stable during the days used to transfer the ozone calibration, as can be inferred from the corresponding standard lamp R6 ratio time series (see Figure 3.18).

Overall, we achieved a quite good agreement with the reference instrument Brewer#183 after the new calibration constants were applied (see Figure 3.19). Ozone deviations are found to be of the order of +/-.5% for the ozone slant path region less affected by the stray light rejection (OSC<800 DU for most of single Brewers).

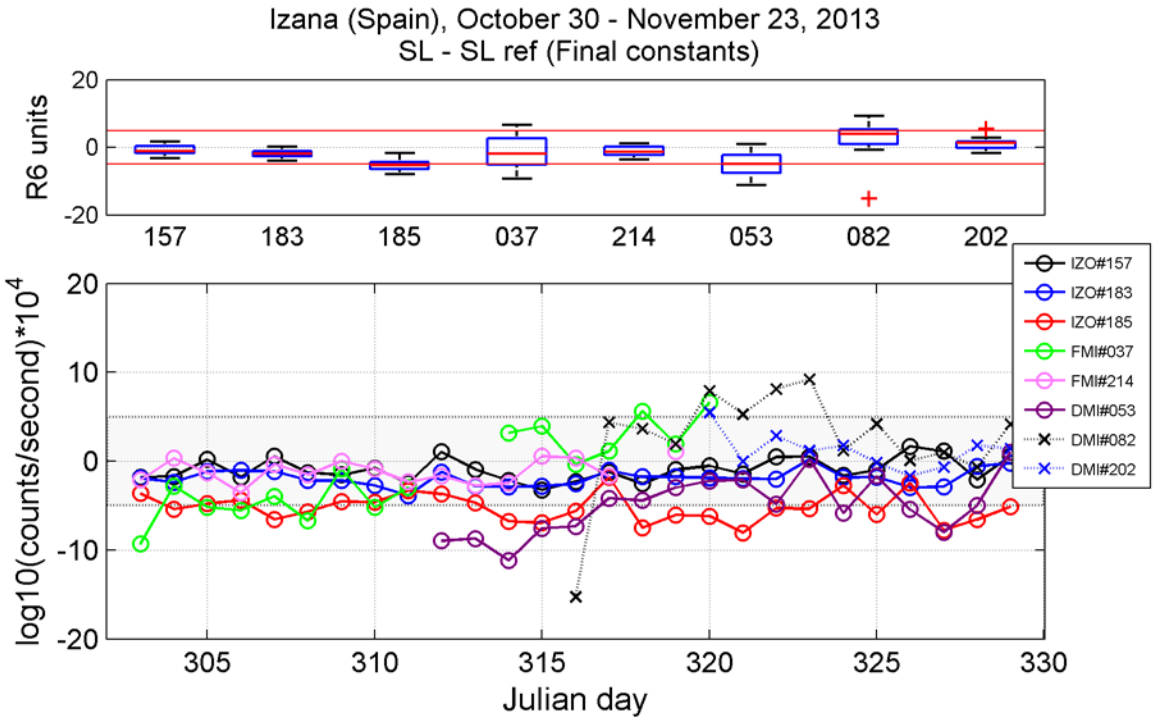

Figure 3.18: Standard lamp R6 ratio to R6 reference value from last calibration differences during the final days grouped by Brewer serial number (above) and as a function of time (below). The shaded area represents the tolerance range +/-5 R6 units.

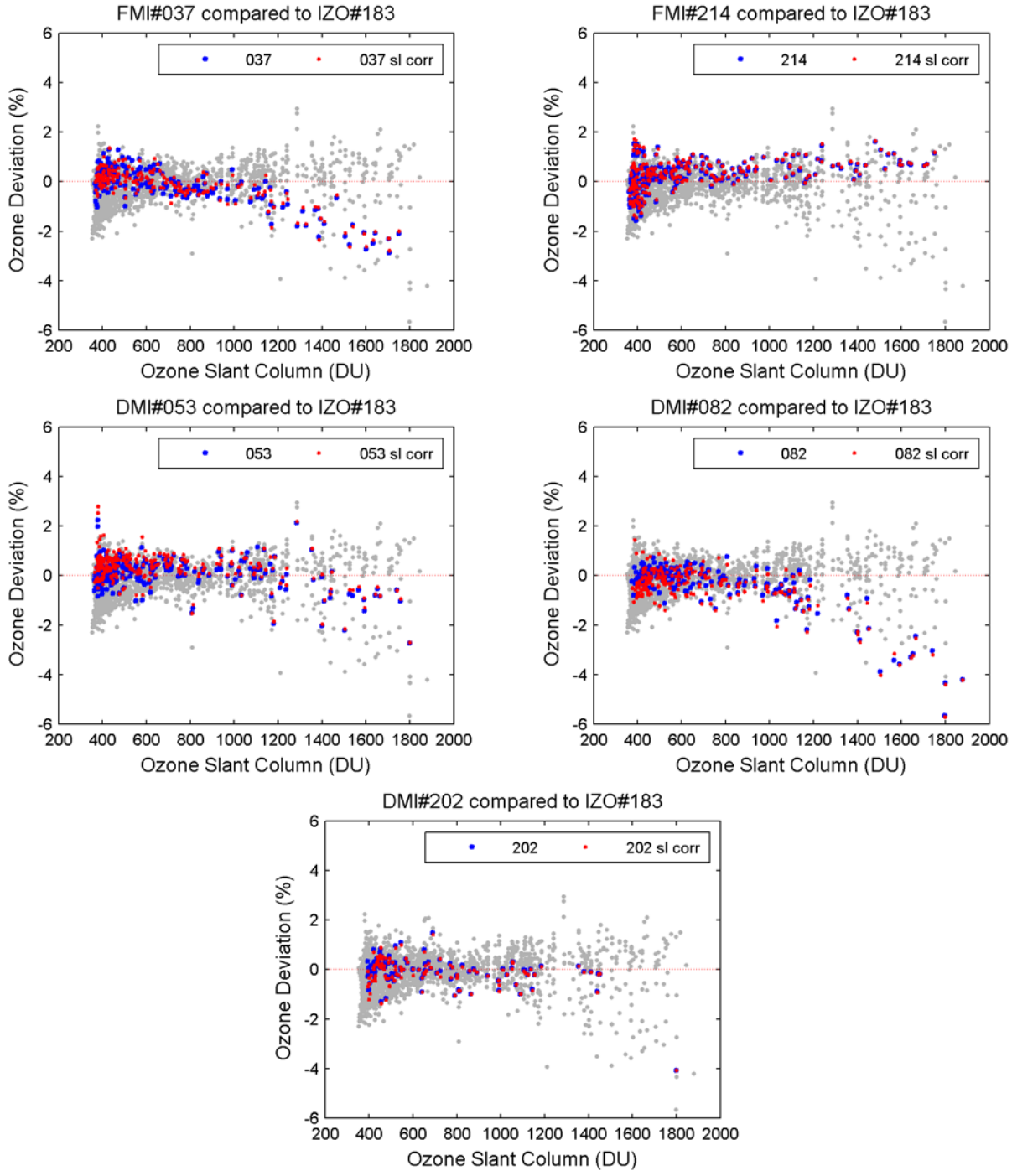

Figure 3.19: Final-days ozone relative differences (percentage) of Izaña 2013 participant instruments to RBCC-E travelling standard Brewer #183. Ozone measurements collected during the final period were reprocessed using the proposed calibration constants, with (red stars) and without (blue stars) standard lamp correction. Grey dots mean ozone deviations for all participating instruments.

3.4 Single Brewer Stray Light Rejection

The underestimation of Brewer Total Ozone due to the stray light rejection on single Brewer was already discussed on the previous report. A new physically based corrective method has been developed and tested within the scope of this project, which will be reported in Section 4 of this report. Here we show the results of an empirical method which is based entirely on comparison with a reference instrument. This empirical method should work fine enough so as to achieve the required precision ±.3% on Brewer column ozone, as demonstrated using the results of Huelva 2013 and the different calibrations performed on Sodankyla Brewer#037.

As a starting point, we will first introduce the basis of the 1-parameter calibration method, which is based on the Brewer Total Ozone retrieval algorithm:

$$X = \frac{N - B}{A\mu} \tag{1}$$

Here $N=F-F_0$, with F and F_0 being linear combinations of logarithms of the direct normal irradiance at the surface and extraterrestrial irradiance at the four wavelengths used for Brewer total Ozone measurements, respectively, μ is the ozone airmass, B is the Rayleigh coefficient and A is the ozone absorption coefficient. Note that all the instrumental characterization is already present on the *F* term. This includes Dead Time as well as temperature dependence. It is also noteworthy that neutral density filters corrections, if any, will be also included on the same term.
The transfer of the calibration scale (namely F_0) is done by side by side operation with the standard instrument. Once we have collected enough near-simultaneous direct sun ozone measurements we calculate the new extraterrestrial constant after imposing the condition $X_{ref} = X_{inst}$, which in terms of Equation 1 leads to the following:

$$F_o = F - \mu \times A \times X_{ref} \tag{2}$$

From this equation we obtain a set of (F_0,*osc*) pairs, where we have defined the ozone slant path as *osc* = $\mu \times X_{ref}$.

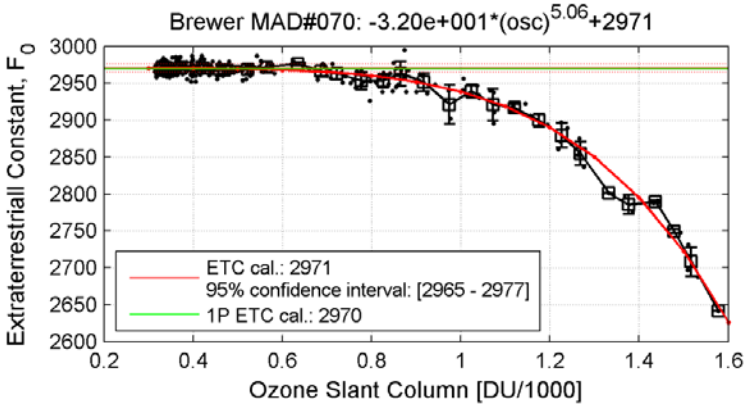

Figure 3.20: Extraterrestrial constants derived from comparison of single Brewer #070 against the double Brewer #183 and Extraterrestrial constant fitting curve.

We show in Figure 3.20 the effect of stray light rejection on F_0, as derived from Equation 2 for the single Brewer MAD#070 during the *El Arenosillo 2013* intercomparison (Julian day 167). We model the available set of (F_0,*osc*) values, including the stray light-affected ozone slant path range and using non-linear least squares to fit the observed F_0's to a power-law as $F_0^{corr} = F_0 + k \times osc^s$, where F_0 represents the extraterrestrial constant corresponding to the ozone slant range not affected by stray light, generally below 700 DU for most of single Brewers.

Next we can use this empirical relation for F_0 as a function of o*sc* to correct the single Brewer stray light rejection. For this, we propose the following algorithm:

1. Compute the Brewer Total Ozone (*TOZ*) as usual, i.e., applying Equation 1 (the usual standard lamp correction to F_0 is included in this step).

2. Apply the empirical relation $F_0^{corr} = F_0 + k \times osc^s$, where $osc \equiv \mu \times TOZ$, to obtain F_0 for the whole ozone slant range.

$$F_o^{corr}(osc) = F_o + k\ osc^s = F_o + k \times (\mu X)^s$$

3. Using F_0^{corr} in Equation 1 we obtain the Brewer Total Ozone stray light corrected.

$$\mathrm{X}^{corr} = \frac{F - F_o^{corr}}{\mu \times A}$$

It is important to note that, as mentioned, the power-law so far discussed is derived from comparison with a reference instrument. Hence, the ozone slant path refers to the real ozone (as measured by a double monochromator). Because of single Brewer affected by stray light, Total Ozone in step 2 is underestimated, but we can use this as an estimation of the real one and iterate the procedure until the ETC correction is below certain limit (5 units). Generally, the correction converges after the second iteration, due to the small OSC dependence of the Ozone at high OSC (at 1500 DU of OSC a change of 45 units in ETC is only a 1% in ozone). We illustrate the procedure in the case of Brewer #070 with a very large stray light issue, resulting in Total Ozone underestimated by more than 5% corresponding to ozone slant path ≈1500 DU (Figure 3.21, top, green solid line).

We have calculated and tested this empirical stray light correction for all single instruments participating at *El Arenosillo 2013* intercomparison campaign. As show in Figure 3.22, we have greatly improved the comparison against the reference instrument (double Brewer) after applying the stray light correction to the Extraterrestrial constant. We also summarize in Table 3.8 the corresponding k and s parameters and the intercept F0, together with the 95% confidence interval, the ETC constant derived from the standard 1-parameter method and the coefficient of determination.

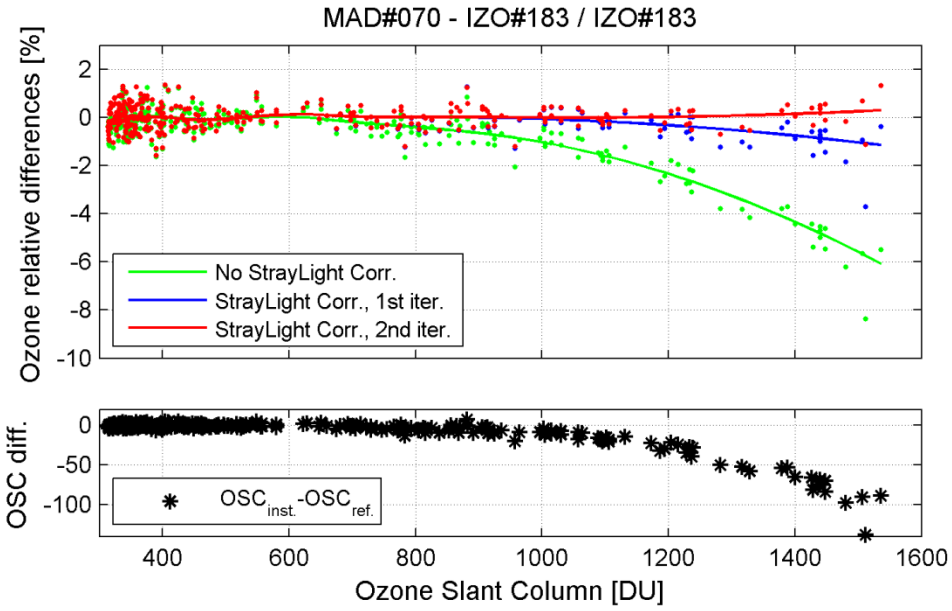

Figure 3.21: Ozone relative differences (percentage) of Brewer #070 against RBCC-E travelling standard Brewer #183 (top) and single to double Brewer ozone slant path differences. Ozone measurements are reprocessed using the final calibration constants without applying any correction to Stray Light (green plot) and after applying the correction method (1 iteration, blue, and 2 iterations, red plots). Bottom figure represent the difference in ozone slant path due to single Brewer Stray Light rejection.

	k	k(95%CI)	s	s(95%CI)	F0	F0(95%CI)	F0(1P)	rsquare
DCL#051, Mk2	-5.27	[-6.95,-3.59]	6.55	[5.89,7.20]	3085	[3083,3087]	3086	0.994
MAD#070, Mk4	-31.98	[-38.49,-25.47]	5.06	[4.59,5.53]	2971	[2965,2977]	2970	0.992
UM#075, Mk4	-48.74	[-58.33,-39.15]	3.74	[3.15,4.34]	3024	[3019,3030]	3021	0.985
KMA#095, Mk2	-7.62	[-10.26,-4.97]	5.46	[4.66,6.26]	2957	[2955,2960]	2957	0.980
MUR#117, Mk4	-12.57	[-16.31,-8.82]	7.21	[6.44,7.98]	2807	[2804,2811]	2806	0.983
UM#126, Mk2	-10.25	[-13.73,-6.77]	5.96	[5.14,6.79]	3251	[3248,3254]	3251	0.985
COR#151, Mk4	-0.34	[-1.01,0.34]	14.15	[9.19,19.11]	2977	[2972,2982]	2978	0.937
ZAR#166, Mk4	-6.59	[-11.21,-1.97]	6.08	[4.29,7.87]	3132	[3128,3137]	3130	0.957

Table 3.8: ETC's non-linear fitting. *El Arenosillo 2013* intercomparison.

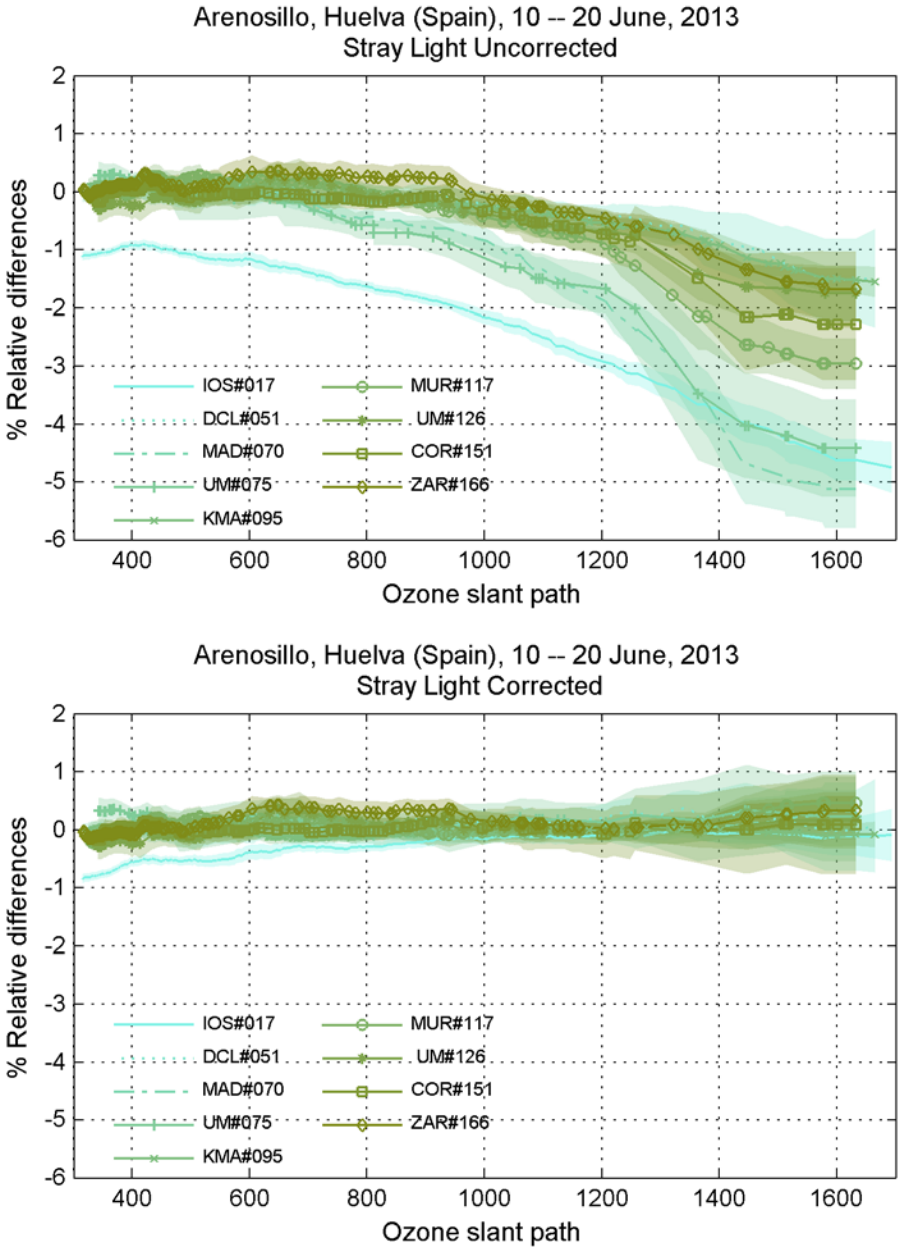

Figure 3.22: Final-days ozone relative differences (percentage) of El Arenosillo 2013 participant single instruments to RBCC-E travelling standard #183. Ozone measurements collected during the final period (after the maintenance) are reprocessed using the final calibration, without (top) and with (bottom) applying the proposed Stray Light correcting. The shadow areas represent the 95% confidence interval. Standard instrument Brewer #017 has been reprocessed using the original calibration constants.

Finally, we show the model results corresponding to Brewer #037 during all the campaigns taking place at Izaña, Spain (2009, 2011 and 2013 years) and at Sodankyla, Finland (2011). This instrument has been well characterized during the last 5 years, and it has been proved to be quite stable. Actually we have used the same configuration as the one provided during the 2009 intercomparison, SL corrected, resulting in a very good agreement with the RBCC-E reference for ozone slant paths lower than 900 DU, that is, corresponding to the stray light free region. During the last campaign (Izaña 2013) the agreement was not so good, even after applying the SL corrections (see Figure 3.23, top, pink solid line). New calibration constants were necessary during this last campaign, but it is expected that single Brewer #037 stray light rejection was still well represented by the empirical model determined at the Izaña 2009 intercomparison (same Figure, bottom).

We have confirmed the validity of the stray light correction calculated during the Izaña 2009 intercomparison (see Table 3.9), applying the same SL correction as usually. The results are shown in Figure 3.23. Note that, as mentioned in previous paragraph, we have applied the same calibration constants (i.e. Izaña 2009, SL corrected) to all campaigns data sets, including a correction factor to neutral density filter #3. It is also noteworthy that, when correcting Brewer #037 stray rejection during the Izaña 2013 intercomparison we have used updated extraterrestrial constant but kept the same *k* and *s* power law fitting parameters (the one calculated at Izaña 2009) as for all the other data sets.

Campaign	k	k(95%CI)	s	s(95%CI)	F0	F0(95%CI)	R^2	$F0_{1P}$	$R6_{Ref}$
Izo2009	-12.00	[-17.58,-6.41]	4.79	[3.79,5.78]	3117	[3112,3123]	0.942	3115	1880
Sdk2011	-12.66	[-18.65,-6.67]	4.56	[3.88,5.23]	3104	[3091,3118]	0.990	3115	1880
Izo2011	-18.29	[-24.51,-12.07]	3.97	[3.19,4.76]	3106	[3102,3111]	0.987	3115	1880
Izo2013	-11.37	[-17.50,-5.25]	5.54	[4.42,6.66]	3119	[3112,3126]	0.986	3120	1870

Table 3.9: FMI#037 Calibration constants including the stray light parameters k and s, the intercept F0 and the ETC constant calculated using the standard 1-parameter method ($F0_{1P}$) and the standard lamp R6 ratio reference value ($R6_{ref}$). R^2 is the coefficient of determination for the power-law fitting.

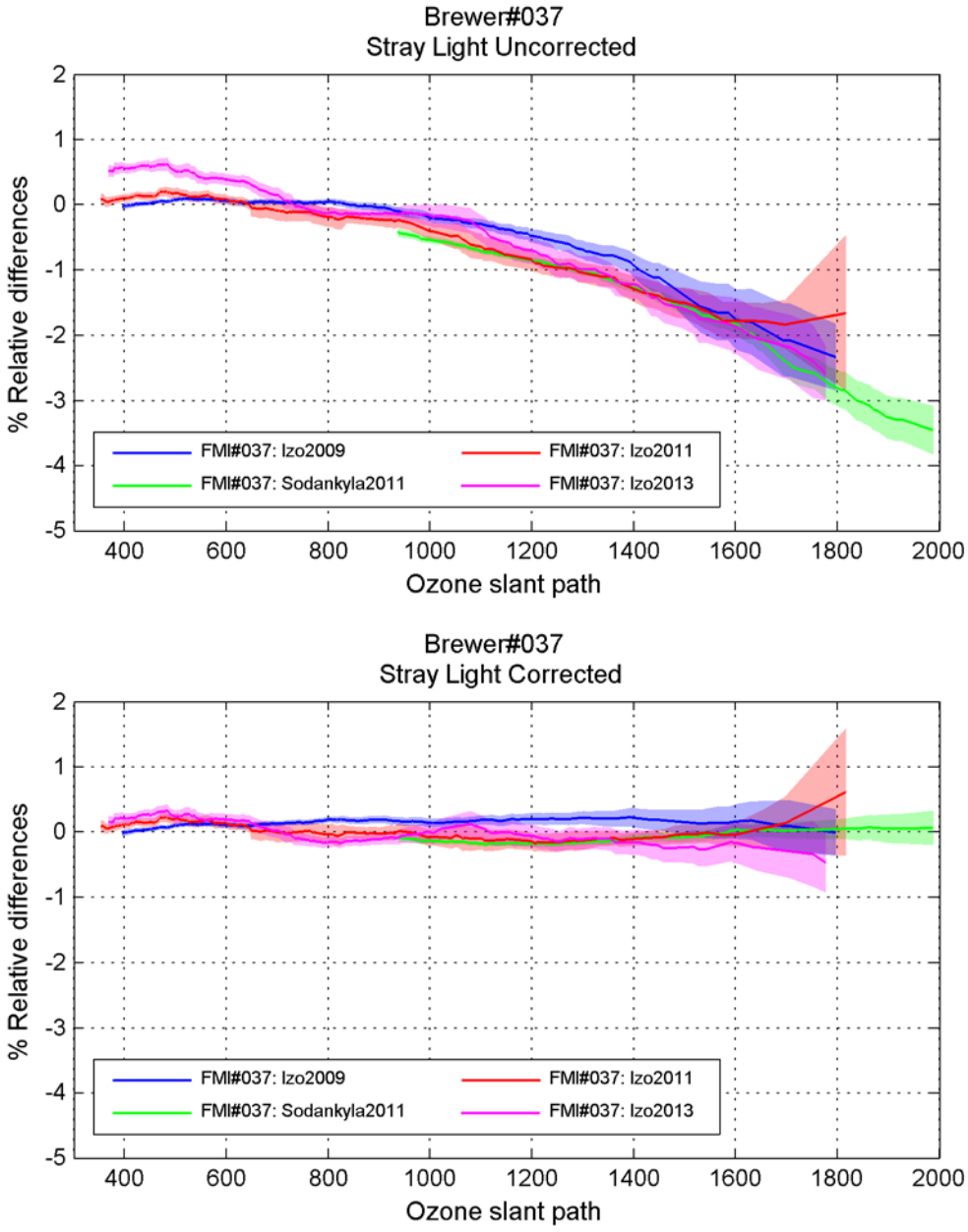

Figure 3.23: Ozone relative differences (percentage) of Brewer #037 to RBCC-E standard instruments Brewer #183 and Brewer #185. We have processed data sets collected during several intercomparisons campaigns (Izaña2009, Sodankyla 2011, Izaña2011 and Izaña2013) with (bottom) and without (top) stray light correction. Ozone datasets have been reprocessed using the same calibration constants provided at the Izaña 2009 campaign, except for updated extraterrestrial constant corresponding to the last Izaña 2013 intercomparison. In all cases a correction factor to neutral density filter #3 has been applied. The shadow areas represent the 95% confidence interval.

3.5 Effect of HARMONICS ozone cross-section on the Brewer and Dobson network

The effect of the change of the ozone cross section were analyzed during this project. This study was recently accepted for publication in ACP.

We have analyzed the effect on the Dobson and Brewer network of five ozone cross section data sets: three dataset that are based from measurements of Bass and Paur, one derived from Daumont, Malicet and Brion (DMB) and a new set determined by Institute of Environmental Physics (IUP), University of Bremen developed during the HARMONICS projects. The three Bass and Paur (1985) sets are: quadratic temperature coefficients from IGACO web page (IGQ4), the Brewer network operational calibration set (BOp), and the set used by Bernhard et al. (2005), in the reanalysis of the Dobson absorption coefficient values (B05). The ozone absorption coefficients for Brewer and Dobson have been calculated using the normal Brewer operative method, which is essentially the same, that used for Dobson instruments.

A full description of this work and of the conclusions reached is available in Redondas et al. (2014), also attached as an Annex of this report.

4 Straylight error compensation in single Brewers (WP 2)

4.1 The stray light model

The stray light rejection properties of single Brewers are well documented in section 3.4. To illustrate the reasons for these properties and how to compensate for the effects of stray light a model of Brewer measurements was set up. The basic physical stray light correction model, written in Matlab scripting, was developed during the main project. The model can be considered physical since it is based on the simulated measurements in a radiative transfer model atmosphere (*Libradtran* RTM in this case) rather than comparing instrument to another. The properties of the modelled Brewer are based on real laboratory measurements.

In the model the irradiance spectrum, I(λ), is created by Libradtran radiative transfer model. The spectrum is then turned into count rate of a model Brewer, F, for each slit n:

$$F_n(\lambda_n) = \int S(\lambda_0 - \lambda) \times R_n(\lambda) \times I(\lambda) d\lambda \,.$$

Slit function S and the response R are based on the laboratory measurements. The double ratio MS9 is then calculated as

$$MS9 = 10^4 \times \log_{10}\left(\frac{F_5^{2.2} \times F_4^{0.5}}{F_6^{1.7} \times F_3} \right)$$

and the total ozone column, MS11, is derived from equation

$$MS11 = \frac{MS9 - ETC}{A\mu},$$

using the air mass calculated from the zenith angle put into the model. Calibration coefficients ETC and α are got by doing a two-point calibration on the model Brewers using the model input ozone as reference.

The difference in stray light properties of Brewers can be described by slit functions (Figure 4.1). When measuring a monochromatic source, the signal outside the main peak measured by a single Brewer is usually two orders of magnitude larger than signal measured by a double Brewer. In the model the amount of stray light is evaluated by considering difference of two cases: First, an ideal Brewer that has narrow slit functions with no wing regions and, second, a real Brewer that has truly measured slit functions. Otherwise the two Brewers are considered identical i.e. the response functions (Figure 4.2) are the same. The model has been described in detail in (Karppinen et al., 2014) and complemented in the extension period as described in the following subsections.

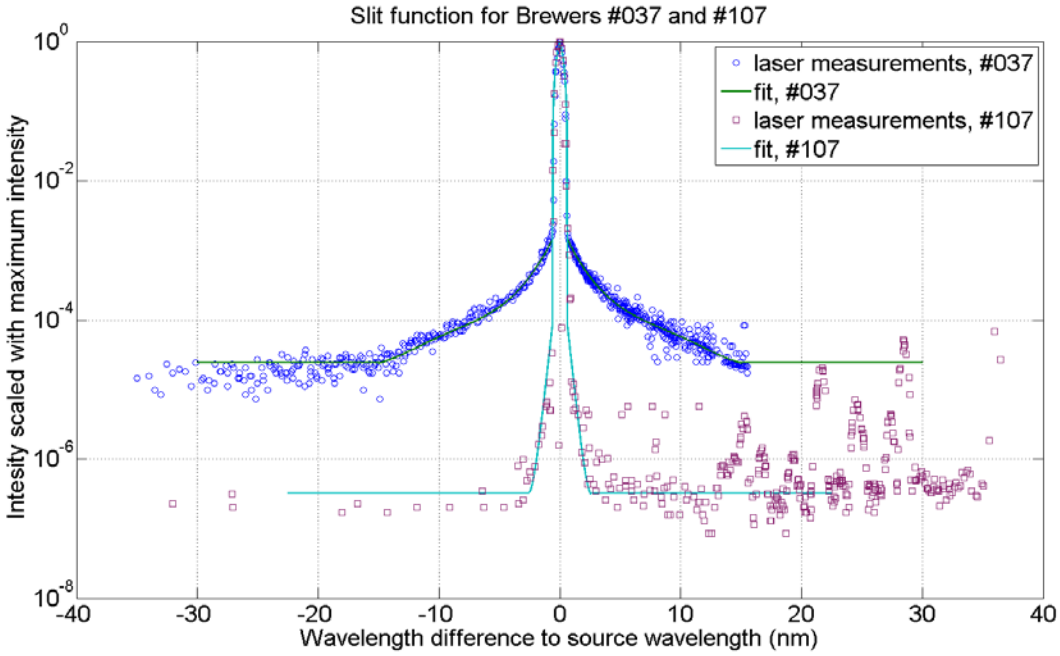

Figure 4.1: Slit functions measured with an HeCd-laser for the single Brewer#037 and a double Brewer #107 at Izaña 2011. For Brewer #107 there are some spikes in the wing caused by internal reflections. On average, for Brewer #037 the relative intensity outside the triangular core is about two orders of magnitude.

4.2 Nordic Brewer campaign at Izana

Nordic Brewer campaign at Izana Oct-Nov 2013 was already described in chapter 3.1 above. FMI participated in this campaign with two brewers: the old single Brewer 37 and a new double Brewer 214. The purpose of the campaign was to establish a proper calibration for the new Brewer 214 and to check and update the calibration data for Brewer 37. For the latter instrument the aim was also to complement the instrument characterization by additional *slit function* and *response function* measurements to update of the straylight correction model.

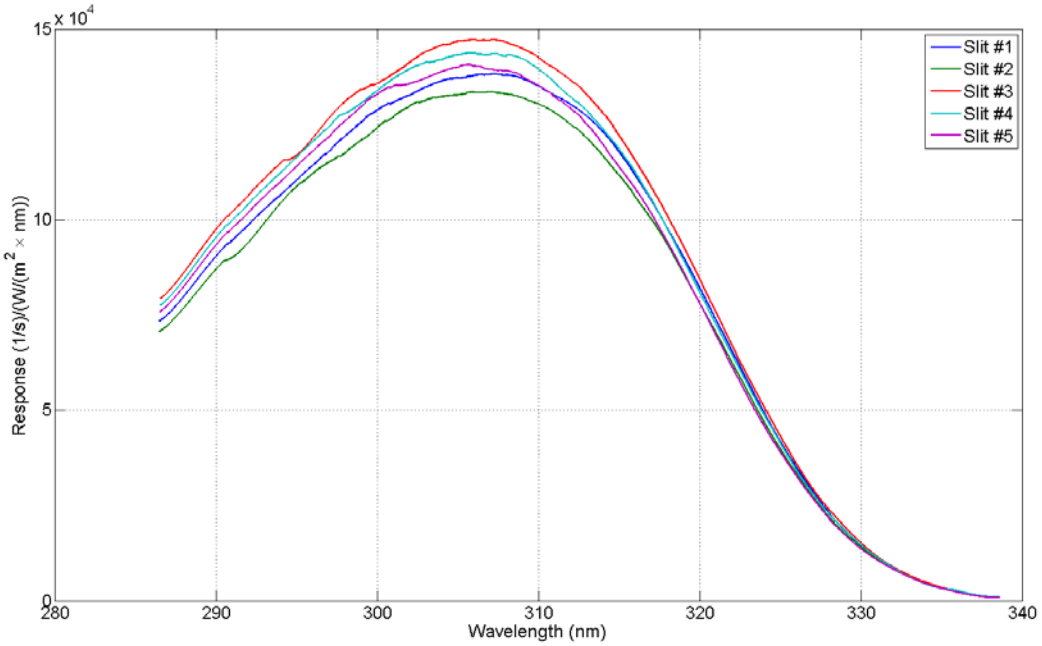

Figure 4.2: Brewer #037 direct response measured in a dark room in Sodankylä using 1000 W calibration lamp.

4.2.1 Individual slit functions

Periodically, high resolution one sided HeCd scans over the longer wavelength extend have been performed for the slit #1 to get information of the wing region (negative wavelengths w.r.t. the central peak, Figure 4.1). The high resolution slit function scans for all the slits have not been available previously. At the current campaign high resolution HeCd laser scans over wide micrometer step range were performed for each slit to obtain measured slit functions over the widest possible wavelength range (Figure 4.2). The wavelengths covered for each slit were: Slit #1 290-328 nm, Slit #2 294-331 nm, Slit #3 298-335 nm, Slit #4 301-338 nm and Slit #5 304-341 nm.

The measurements revealed a symmetric secondary reflection in the wing region of all the slit functions which has not been observed before (Figure 4.3). This “bump” was more closely studied but the origin was not confirmed. There were tries to remove the bump by changing the angle of incidence for the laser beam and by using the diffuser on filter wheel #1. However this feature remained in the measurements. As it was not present earlier it could be caused by a slight change in the positions of the optics after the last maintenance done in March 2013. This should not have any effect on stray light as the area of the feature is not significant. As Figure 4.4 shows there is not great differences between the wings of the slits. However, there some differences between the peaks (Figure 4.5) as could be expected based on the numerous dispersion tests done in the past.

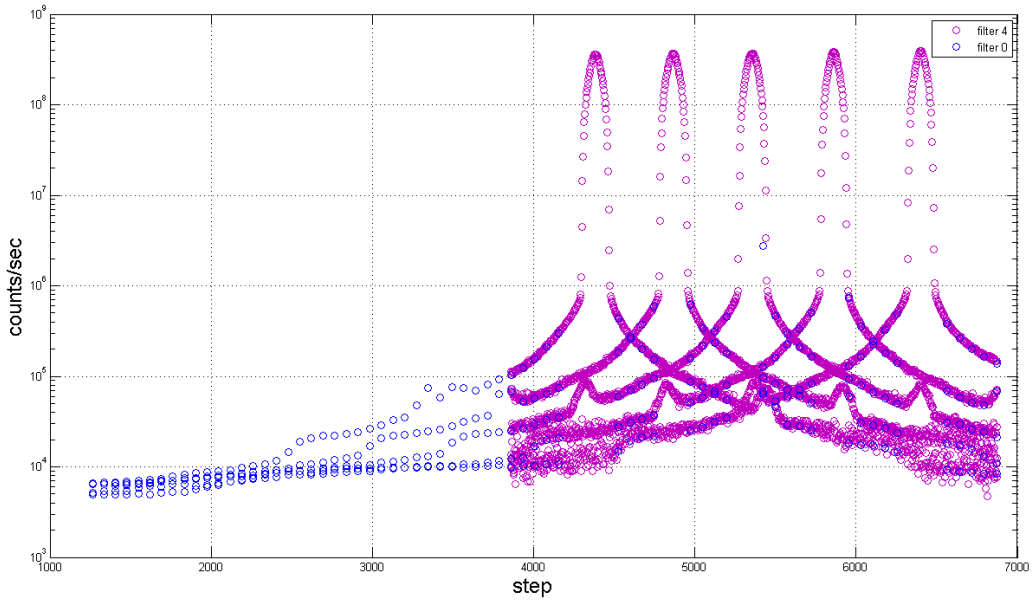

Figure 4.3: Slit functions. Photomultiplier counts as a function of stepping motor position.

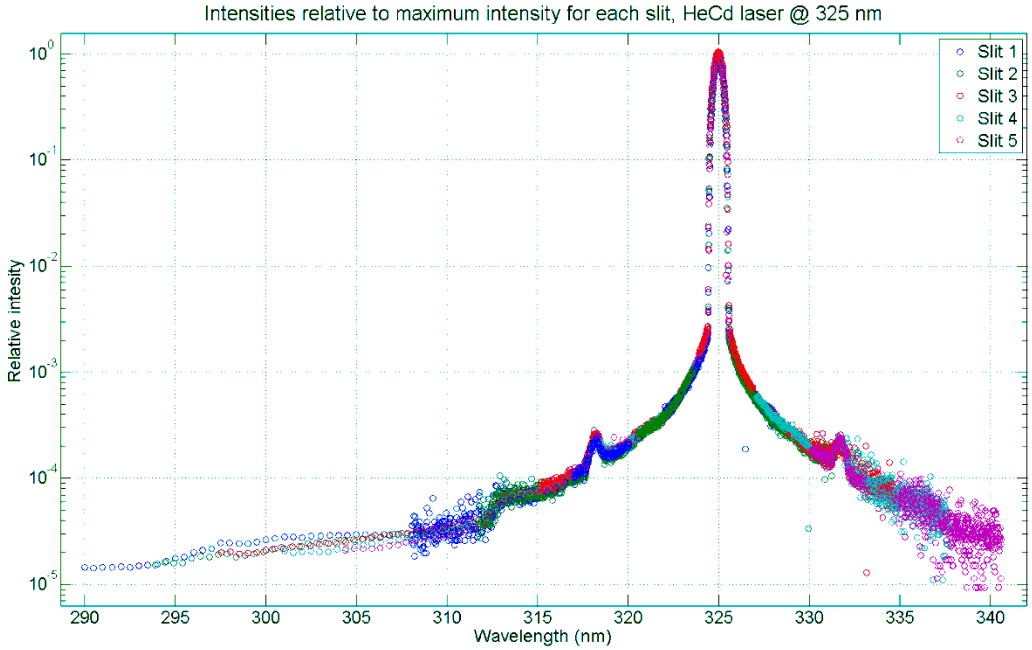

Figure 4.4: All laser measurements on top of each other color coded by slit number. Values are relative to the maximum value of each slit.

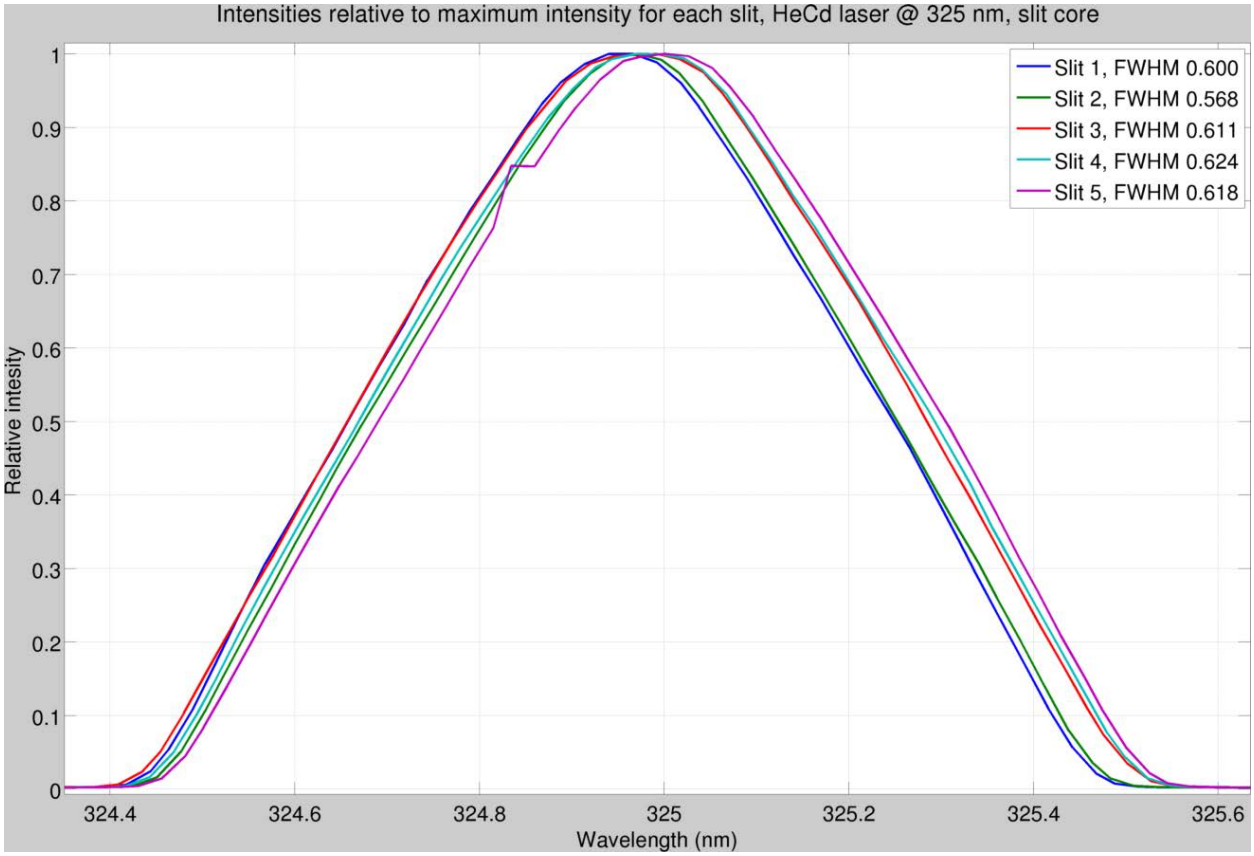

Figure 4.5: The peaks of slit functions for each slit. Full width half maximum (FWHM) is calculated using the highest value of each slit measured. Usually it is calculated from the point where the value is half of the value of the top of a triangle fitted to the measured values.

4.2.2 Direct Sun responses of Brewer 037

Previously we used reconstructed direct responses. During this project we determined real responses for all the Brewer slits using two different methods. First, the laboratory measurements were made at home laboratory using halogen lamp of known irradiance traceable to NIST standard. Second, during the campaign at Izana observatory the shadowing disc method was used based on the quasi simultaneous measurements of global and diffuse irradiance (see eg. Kazadzis et al, 2005 for details on both methods). The two methods agreed fairly well and in this report the calculations were made using laboratory measurements (Figure 4.6 and Figure 4.7).

The lab measurements were performed in February 2013. The lamp holder was lifted as high as possible without heating the ceiling and Brewer was set to look to at the lamp at an angle. The angle, position of the prism, was set using teletype-commands and viewing the lamp through the entrance slit viewport. The horizontal angle was found by turning the Brewer by hand. The distance measured from the filament of the lamp to the quartz window of the Brewer was 306 cm. This measure was used when calculating the lamp intensity from the calibrated irradiance values of the lamp using the inverse square law.

Direct response measurements using shadowing method were made during the last week of Izana campaign. For the method an earlier Brewer routine was modified to work with a single Brewer and to measure all the slits consequently. The routine is based on a cycle consisting of a direct measurement, a diffuse measurement (global UV port with the shadow cast on the dome) and a global measurement. A special motorized arm was used to make the procedure more reliable and easier to control without going near the instrument and thus interfere with the measurements. The motor was programmed to follow the movement of the Sun and the performance of the motor was followed through a webcam. The offset of the motor could be changed through a web based interface.

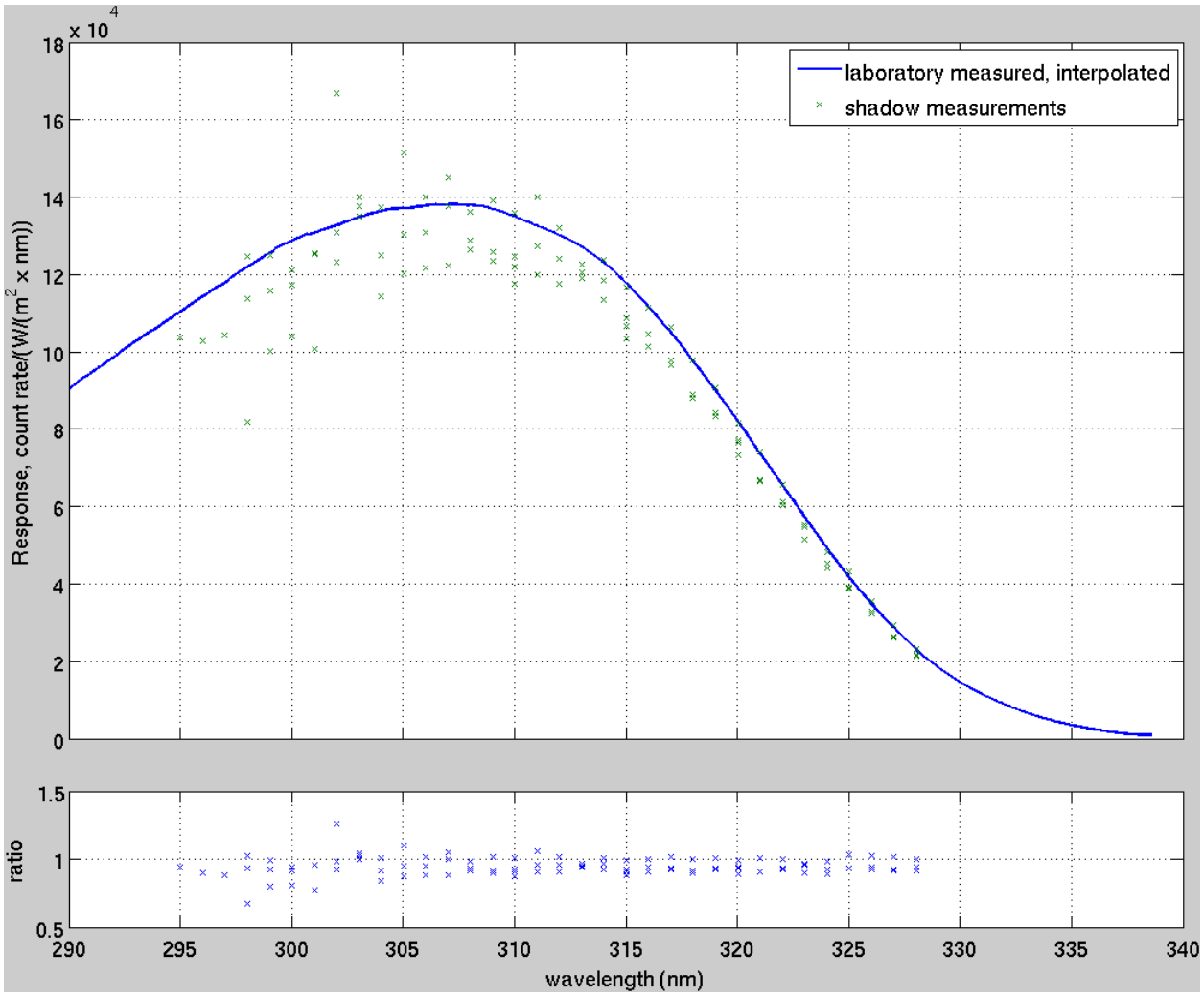

Figure 4.6 Direct response measured for Slit #1. The interpolated measurement is also expanded to longer wavelengths by response values form other slits scaled to match the last measured value of slit #1.

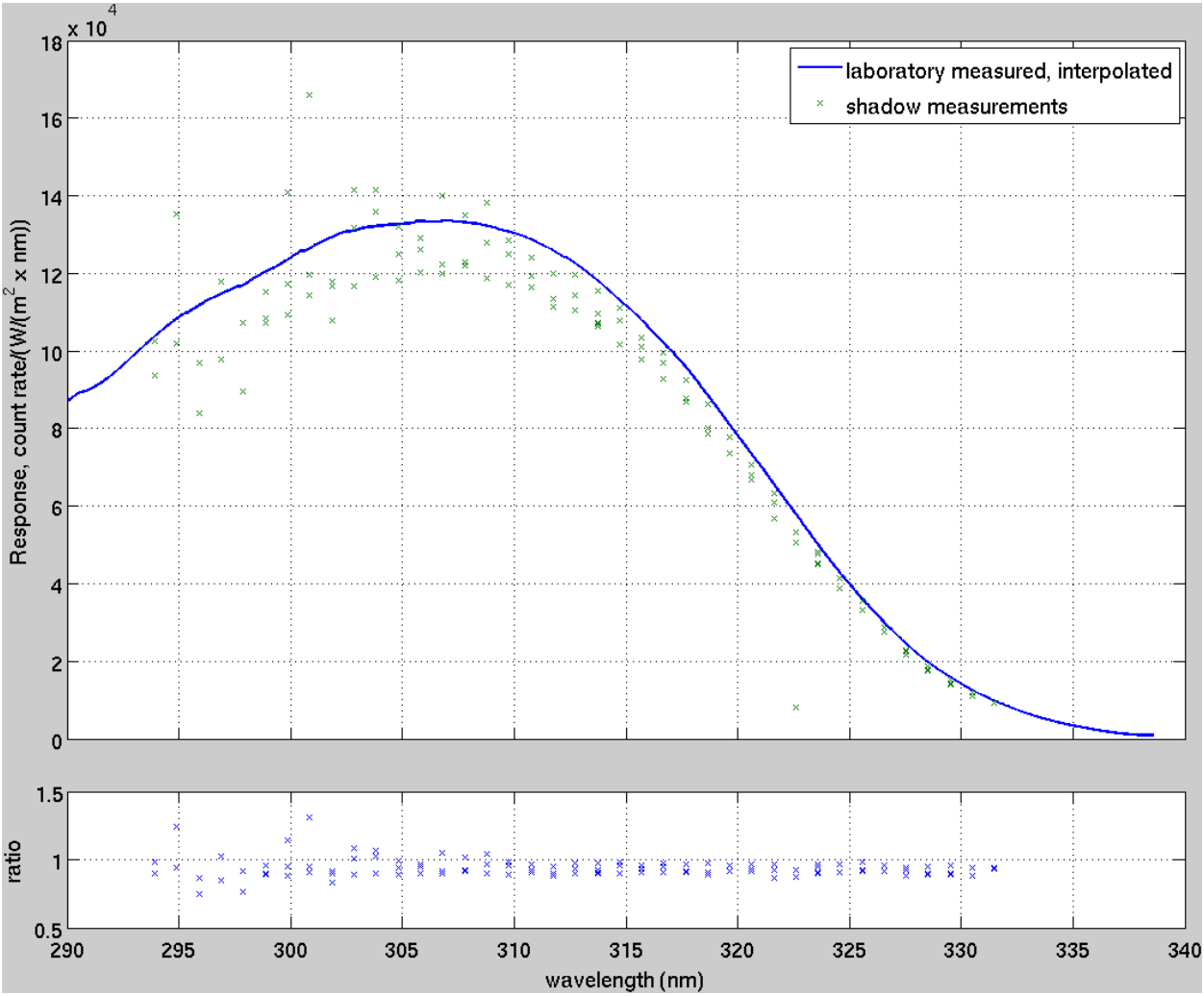

Figure 4.7: Direct response measured for slit #2. The interpolated measurement is also expanded to longer wavelengths by response values form other slits scaled to match the last measured value of slit #2.

4.2.3 Results of the stray light model

The radiative transfer model was set up as follows. The atmospheric parameters were based on Tenerife ozone soundings. The aerosols were set low by denoting aerosol visibility to 50 km. Bass and Paur (1985) was used for ozone cross sections. The model was run for ozone range of 220 to 570 Dobson units (DU) and air mass values of 1.01 to 6.01 to get wide range of ozone slant columns, even if the values are not realistic for Tenerife. The double ratios as a function of model input slant column are presented in Figure 4.8.

For an unresolved reason there was a slight difference between the modelled and real measurements. To diminish this mismatch, all the modelled double ratios (MS9) were multiplied by 1.075 to get the modelled values to obey similar calibration coefficients as the real measurements. The calibration

coefficients for the model Brewer were determined by using the model input ozone as reference and calculating the two point calibration coefficients for slant columns below 900 DU as opposed to the one point calibration done for real measurements. The model results suggest that the slit function has an effect already on small slant ozone columns and thus the absorption coefficient A is slightly smaller for a modelled single Brewer.

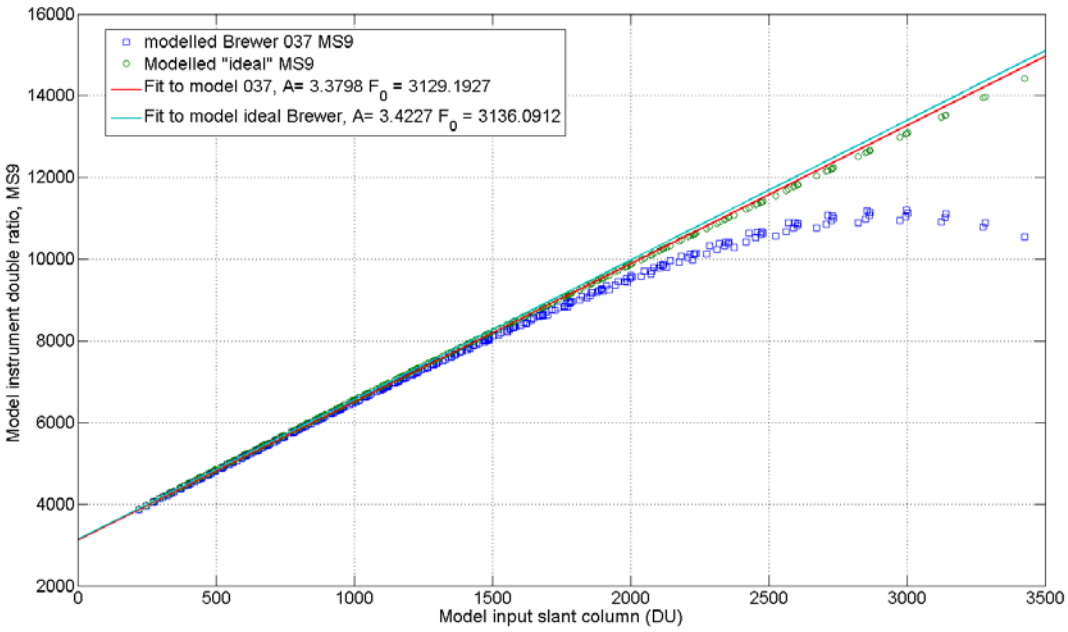

Figure 4.8: The modelled values of double ratios, MS9, for Brewers with different slit functions. Deviation from the calibration line is clearly visible for both ideal and

As opposed to the Karppinen et al. (2014) we did not want to redo the calibration for the corrected double ratios so the stray light compensation was calculated to make the modelled double ratios to obey the calibration line throughout the whole slant column range. The deviations, β, of each modelled MS9 from the line representing the two-point calibration was calculated as

$$\beta = MS9 - (A \times MS11 - F_0),$$

where MS11 is the ozone input to the radiative transfer model. The β of modelled single and double Brewers are depicted in Figure 4.9. The difference of β between the Brewers was calculated to get a slant column dependent coefficient which can be applied on Brewer 037 double ratios to make the performance of single Brewer to resemble the double Brewers. For this combined β a piecewise polynomial fit was applied and a look-up table was created from which the stray light compensation could be interpolated for each slant column. The fit was made as a function of single Brewer slant column so the compensation can be done without the measurements of a double Brewer. Comparison of Brewer 037 to RBCC-e Brewers during the 2011 campaigns is shown in Figure 4.10.

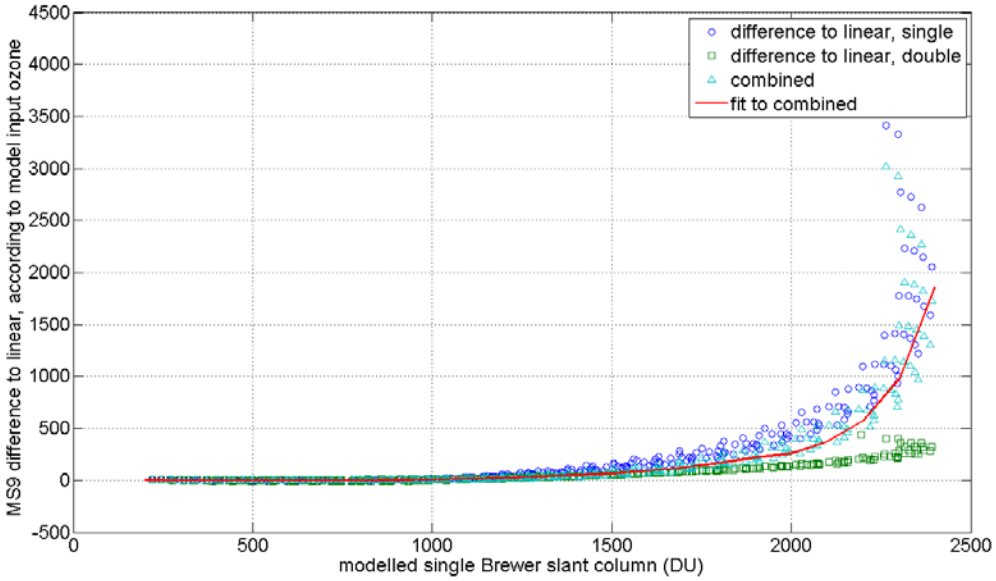

Figure 4.9: Modelled non-linearities for single and double Brewers. The compensation used for real measurements is the piecewise fit function interpolated to each slant column.

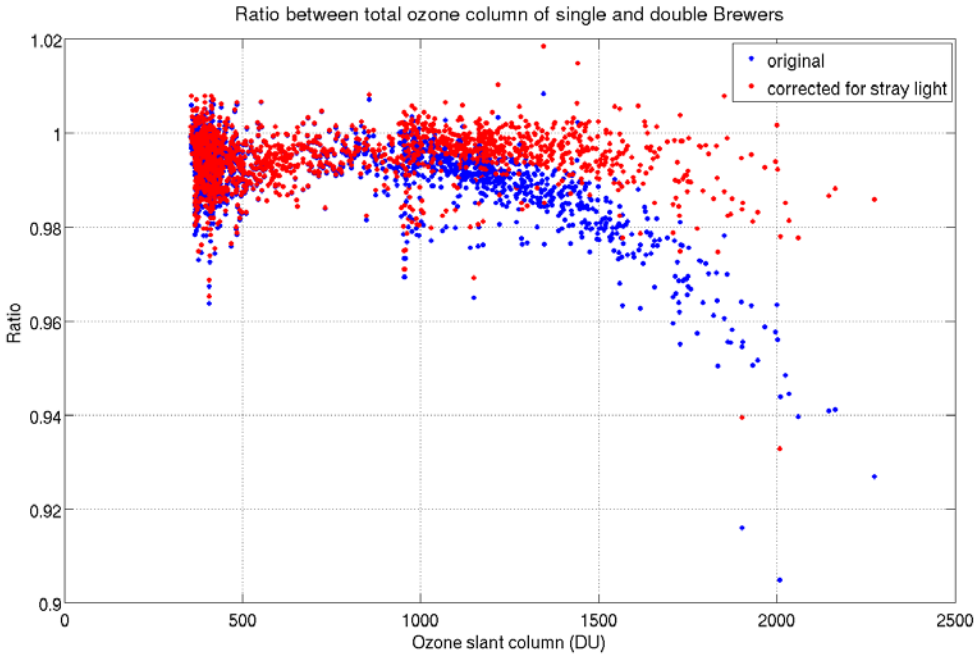

Figure 4.10: Ratio of total ozone between Brewer 037 and RBCC-E Brewer 157 and 185 during Ceos campaigns in Sodankylä and Izana 2011.

4.2.4 Comparison of Brewer 37 and Brewer 214

Originally the idea was to test the field performance of stray light model by comparing the simultaneous measurements of single Brewer 037 and newly purchased double Brewer 214 in spring and summer of 2013. However, the new Brewer performance proved to be inadequately tested at the factory. Even after service trips from the factory problems were not solved and the instrument had to be sent back to factory. The instrument was finally fixed just prior to the Izana campaign. Therefore, all the comparison results are from the Izana campaign. As chapter 3.1. shows, when the slant column increases the 214 seems to have a bit higher ozone column than Brewer 183. Therefore it was expected that the stray light compensation is not enough to bring the single Brewer 037 up to the level of 214 (see Figure 4.11). Also the model suggests a small addition to MS9 at very low slant columns which further deviates the ratio from even situation on very low slant columns.

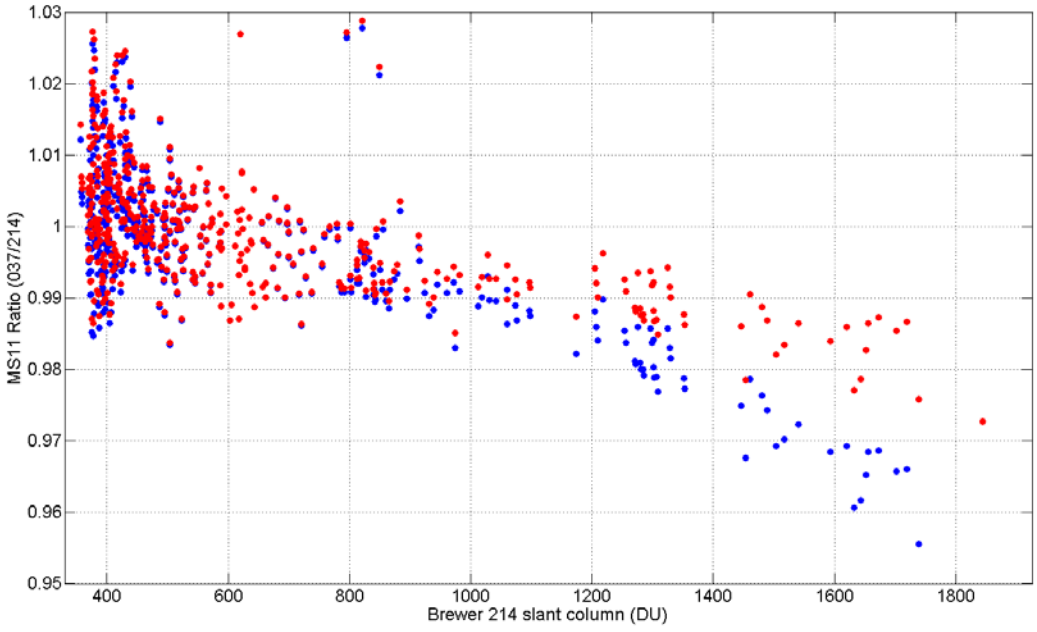

Figure 4.11: Ratio of total ozone columns between a double Brewer 214 and a single Brewer 037. Measurements from nordic Izana campaign 2013.

4.3 Long term data set of stray light corrected Sodankylä total ozone

In the extension phase of the project the data reduction routines were further developed to allow fluent processing. The correction routine uses Brewer raw data files (“B-files”) and instrument files in an automated batch processing scheme. It should be emphasized, however, that to start the decadal runs fair amount of manual work will be always needed, first to remove bugs in the raw data files and especially in building the instrument response and coefficients history from annual/biannual calibrations, uv-response measurements and daily standard lamp files. After data and metadata are organized also long time series of DS total ozone measurements can be processed (semi)automatically.

As a final test of the model we applied the stray light correction to the long term total ozone data set at Sodankylä. Total ozone has been measured at Sodankylä since May 1988 and the time series is among the longest in the European Arctic. Brewer 037 has a well-documented calibration history and the changes in the instrumental coefficients are well documented. The effect of stray light is strongest in Spring when the ozone slant path in Arctic can be quite large even at noon. Mean ratios between original and stray light corrected daily mean values are shown in

Figure 4.12 below.

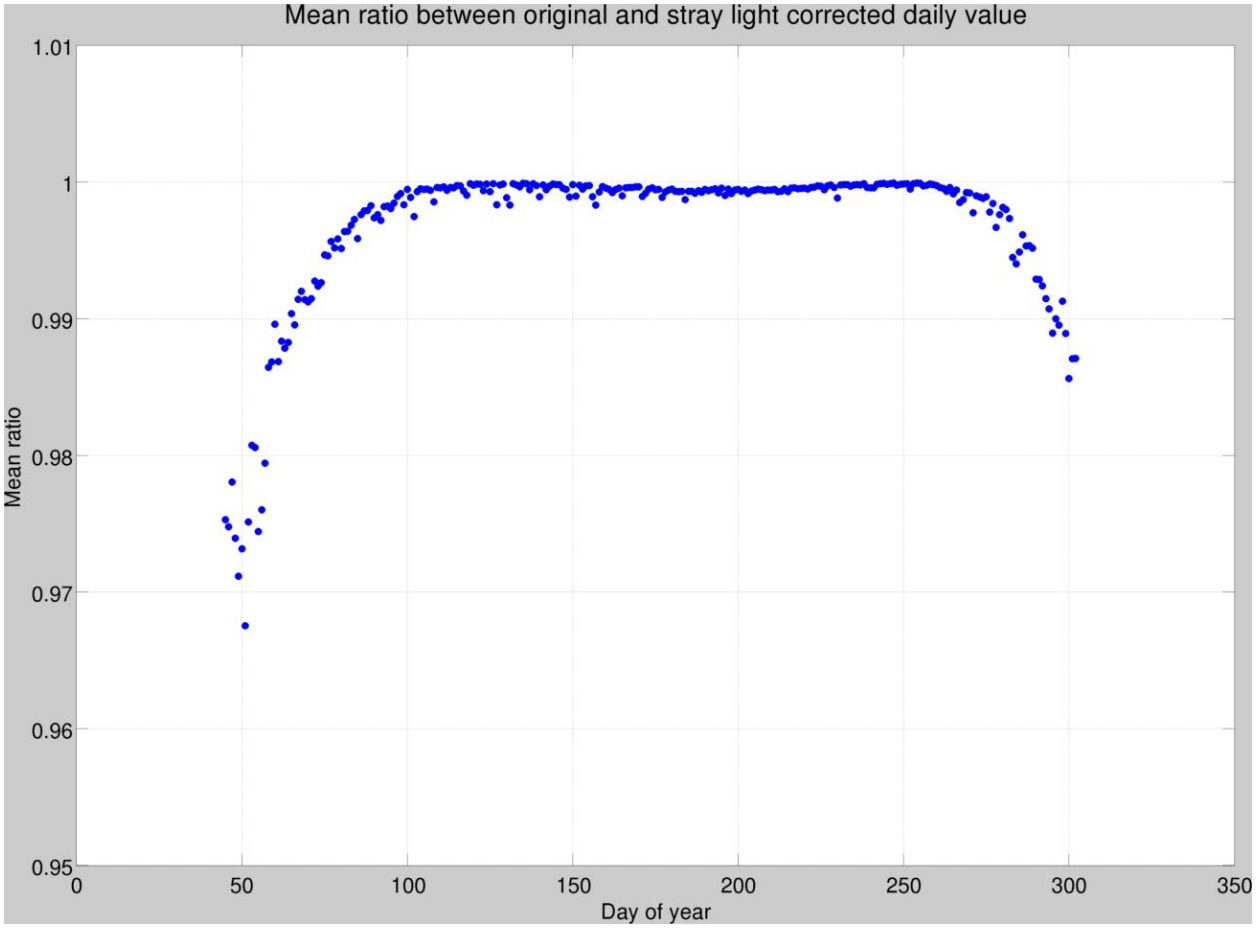

Figure 4.12: Average ratios between original and stray light corrected daily mean values.

The monthly mean values of spring months 1989-2013 are presented in Figure 4.13 (corrected and non-corrected). Clearly the well-known cold winters of the high Arctic loss (e.g. mid 90's, 2005, 2011) and the warmer winters of high spring ozone behave differently with respect to stray light effect and corrections in the former case to monthly means are significant. However, the effect seems to have only marginal influence on the long term spring trends (Figure 4.14). If we assume a piecewise linear March trends with the inflection point at 1997 we have for the original data 1989-1997 thinning at the rate of -8.6 % and recovery at the rate of +1.2% per year for 1997-2013. In case of the stray light corrected data the respective numbers are -8.9 % and +1.2 % per year. Outside the spring months stray light has insignificant effect on the mean value. The daily means for a time series always can be selected close to the noon thus excluding large ozone slant paths after April. Annual course of ozone layer thickness also contributes to smaller ozone slant paths towards summer and autumn. In October again the effect of stray light becomes visible.

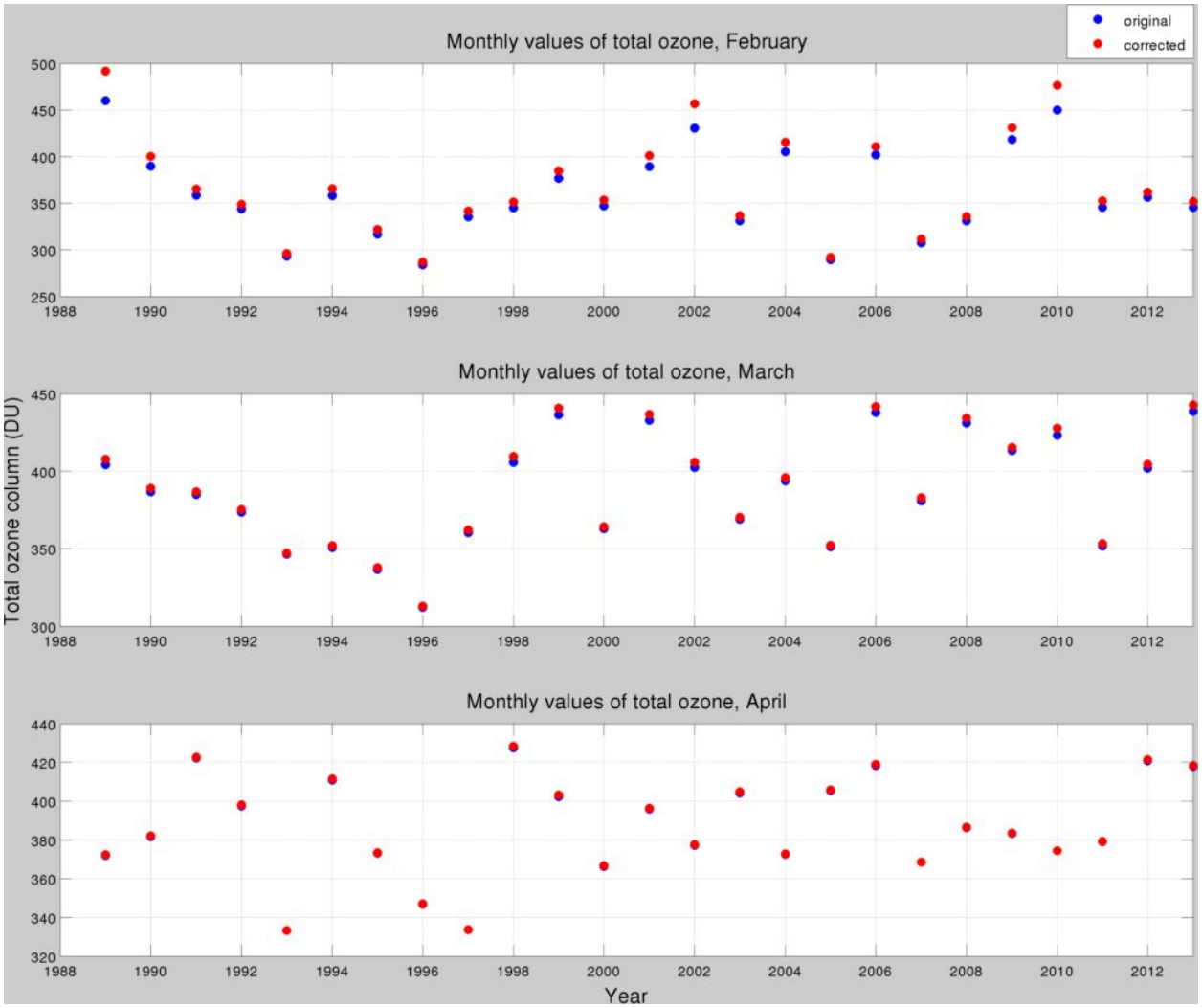

Figure 4.13: Monthly mean values of original and stray light corrected measurements of spring months.

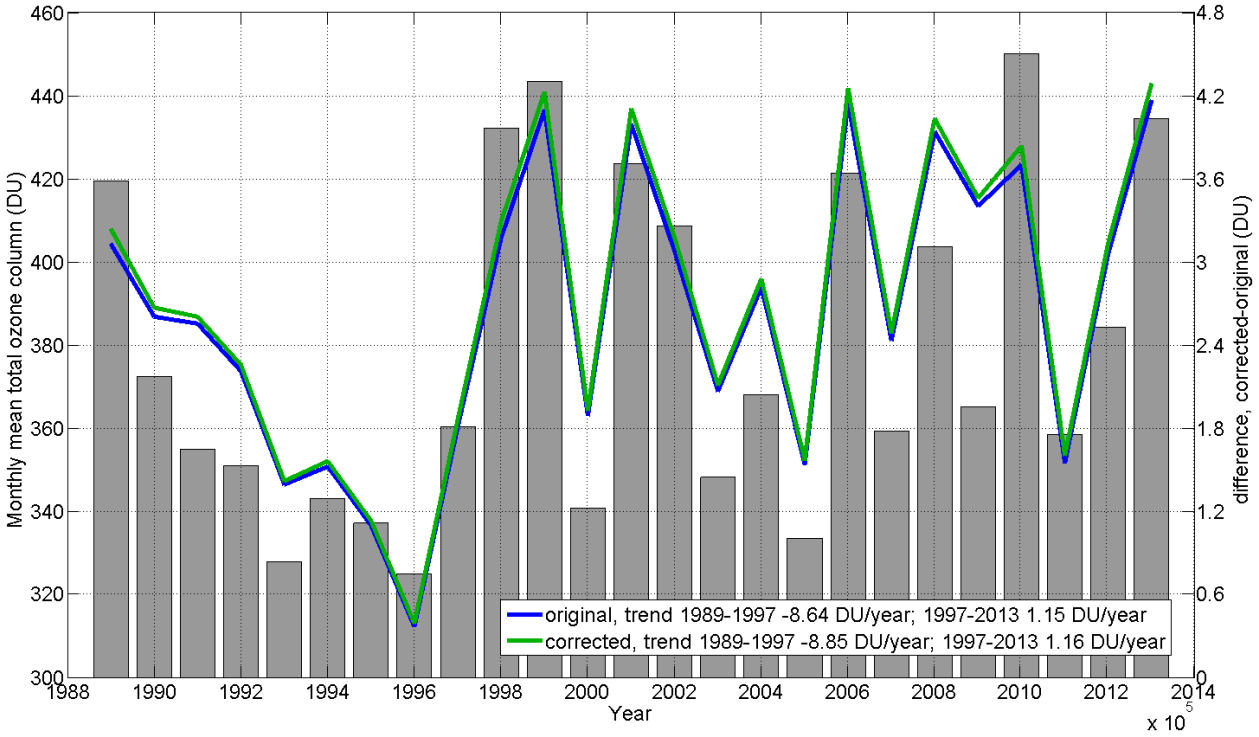

Figure 4.14: Corrected, non-corrected and size of the corrections in DU of the 25 March average values over the period 1989-2013.

4.4 Comparison of empirical correction and the stray light model on Brewer 037

The observations of three Nordic campaigns and his counterpart at Izaña are evaluated for the Brewer #037, using the stray light correction model and the empirical correction (Section 3.4). The comparison of this two approaches to correct the stray light, the stray light model and the empirical correction (Section 3.4) are shown in Figure 4.15. As stated in previous section the model slightly overestimate (up to +0.2%) the ozone at small ozone slant column. The agreement is good (0.1%) on the standard operating range of the instrument from 600 to 1200 DU whereas the model underestimate the ozone in the high OSC conditions up to 1% at 2000 DU OSC. Even that the improvement of model is remarkable the Brewer 037 without correction underestimate the ozone around 4% at 2000 DU (Figure 3.23) and only 1% when the model correction applied.

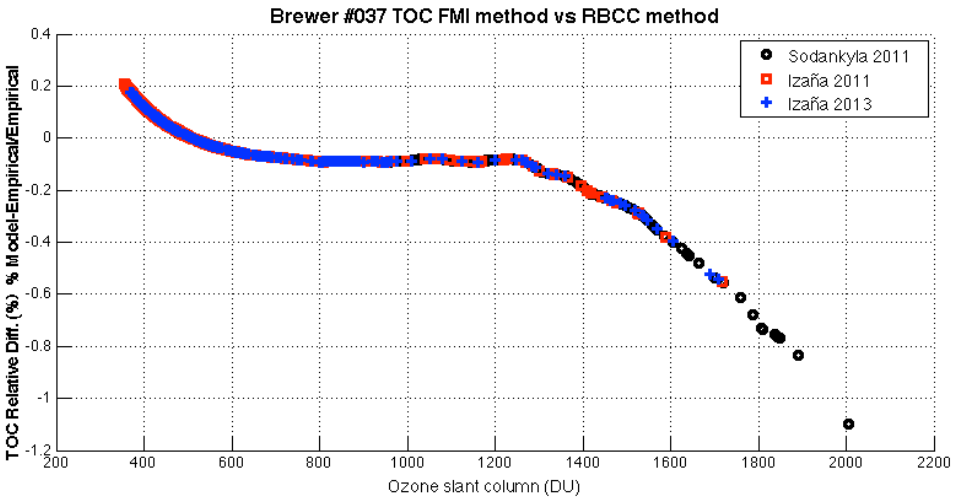

Figure 4.15: Ratio of total ozone columns calculated by the stray light model and the empirical correction from the comparison of a double Brewer. The stray light models slightly overestimates the ozone at low ozone slant column whereas underestimate the correction at high OSC, at standard conditions 300-1400 the agreement of both methods are very good.

5 Extension of CINDI data analysis and MAXDOAS developments (WP 3)

During this period, we have focused on the continued development of the MAXDOAS technique as a key tool for the validation of air quality observations to be delivered by the future atmospheric Sentinels 4, 5 and 5 Precursor. As already demonstrated in past studies and further demonstrated in this chapter, MAXDOAS instruments have the potential to deliver relevant high-quality measurements of both column and surface concentrations of most air quality gases that will be operationally generated by Sentinel 4/5/5P, i.e. tropospheric NO_2, HCHO, CHOCHO, SO_2, O_3, (HONO) and in addition they allow for simultaneous measurement of AOD and surface aerosol extinction at UV and visible wavelengths. Since MAXDOAS instruments measure both integrated columns and surface concentrations, they provide an ideal link between "in-situ" air quality monitoring network and satellite instruments. The available profile information also brings a key ancillary information for the verification of satellite algorithms which crucially depend on a-priori knowledge of the trace gas profile shape (generally based on model data). In addition, MAXDOAS instruments operated at twilight in zenith-sky mode also allow for high-quality stratospheric monitoring as demonstrated since early nineties e.g. in the framework of the Network for the Detection of Atmospheric Composition Change (NDACC).

In order to bring all these capabilities to a state where quality-controlled data sets can be operationally generated from a network of existing (and developing) instruments, efforts must be devoted on several axes: (1) deployment of high-quality instruments, assessment of their quality and monitoring of their long term stability, (2) development and demonstration of suitable inversion algorithms for all relevant data products, (3) harmonization of instrument operation, calibration procedures (in particular for elevation scan accuracy which is highly critical), and retrieval methods, (4) harmonization of data reporting including necessary key metadata, (5) development of a strategy for efficient data collection and processing, (6) development of adequate satellite validation methodologies accounting for uncertainty and representativity issues.

This report summarizes the work undertaken at BIRA in 2013 to progress on some of these axes. Results first highlight the continued exploitation of CINDI campaign measurements, with (1) a focus on the development and assessment of tropospheric NO_2 retrieval methods and (2) the development of a new generic cloud flagging approach applicable to all scattered-light UV-Vis instruments. Second we report on ongoing developments for the quality controlled automated processing of MAXDOAS measurements, including GEOMS compliant data formatting (work largely done in synergy with the EU FP7 NORS project) and we finally summarize the work done to extend and demonstrate the capabilities of MAXDOAS instruments for the measurements of other air quality gases than NO_2, with a particular emphasis on SO_2 and HCHO and their use for satellite validation.

5.1 Extension of the CINDI data analysis

5.1.1 Intercomparison of MAX-DOAS NO_2 profile retrievals

This study which has been already introduced in a previous report, is now almost completed (Wittrock et al., 2014). Nine different groups participating to the CINDI Campaign have compared their MAX-DOAS retrieval methods for NO_2, with focus on tropospheric columns (relevant to satellite validation) and surface mixing ratios, the two most frequently used retrieval results. Seven groups (IASB-BIRA, INTA, IUP

Bremen, IUP Heidelberg, Universities of Leeds and Leicester, NIWA and Washington State University) applied full inversion methods by describing the relation between measurements (SCDs of trace gas for different elevations) to the absorber profile as a linear problem. This is solved by using a priori information and the Optimal Estimation Method (OEM; Rodgers et al., 2000) and by doing online calculation of so called block air mass factors (BAMF). Three others (JAMSTEC, KNMI, MPI-Mainz) preferred to use simpler parameterisation methods i.e. reducing the retrieved profile to two to three independent parameters usually by assuming a block profile for the trace gas and retrieving the layer height and the mixing ratio in this layer.

In a first comparison, all groups applied their retrievals to a set of synthetic data computed for different atmospheric conditions. For this exercise, BIRA-IASB calculated NO_2 slant columns for both the UV and the visible spectral regions assuming eight different NO_2 scenarios (see Figure 5.1) and two aerosol loadings (AOD 0.14 and 0.54 at 477 nm) using the radiative transfer model LIDORT. The simulations were carried out applying boundary conditions (meteorology and viewing geometry) from June 24, 2009 in Cabauw. Slant columns for elevation angles similar to those chosen in the intercomparison exercise (Roscoe et al., 2011) were provided and used as input for the profile retrievals (1°, 2°, 4°,5°, 6°, 8°, 10°, 15°, 30°, 89°). The simulated SCDs also included errors which were computed based on real DOAS fitting errors approximated by Gaussian noise. Since this exercise focused on differences in the trace gas retrieval only, the aerosol parameters such as extinction profile, single scattering albedo, and phase function were provided to the participants. All OEM-type retrievals used similar settings for their calculations (e.g. a linearly decreasing a priori profile). More technical aspects were also investigated by using e.g. different altitude grids (50 and 200m) and different a priori errors. With the exception of MPI-Mainz, all groups were able to calculate profiles both for the UV (360 nm) and the visible (477 nm) case.

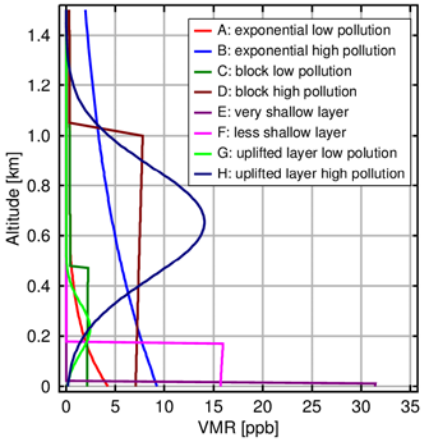

Figure 5.1: Vertical NO_2 mixing ratio profiles used for the simulation of SCDs in the first intercomparison exercise. The numbering of the profiles is the same as in the following figures.

The results of the retrievals on synthetic data are summarized in Figure 5.2 and Figure 5.3. For each profile scenario, the results are given for all groups showing both the low aerosol case (open symbols) and the high aerosol simulation (filled symbol). The solid line indicates the true value used in the simulations, the dashed lines limit the +/- 25% deviations from the true value. Each symbol is the daily

average over 28 retrievals at SZAs between 28 and 78°, the error bars giving the standard deviation of the values over the course of the day. As can be seen from the figures, all retrievals perform well for most situations with results being within 25% of the true values in the majority of cases.

When first considering the tropospheric column retrievals in the UV, some general patterns can be observed. First, the retrievals perform better on high NO_2 situations than on scenarios with lower NO_2 as one would expect from the better signal to noise ratio. Second, in nearly all cases, the low aerosol case has lower deviations from the true values than the high aerosol case, although the differences are not large in most cases. Third, the very shallow layer poses difficulties to many retrievals, in particular at low NO_2 values. This is probably linked to the impact of the a priori profiles which constrain the solution too much in this situation. The effect is smaller at high NO_2, arguably as result of the stronger weighting of the measurement information in this case. The NO_2 column for the uplifted NO_2 layer is well captured by most retrievals at high NO_2 but largely overestimated by many groups in the low NO_2 scenario. This again points at a too large impact of the a priori under these conditions.

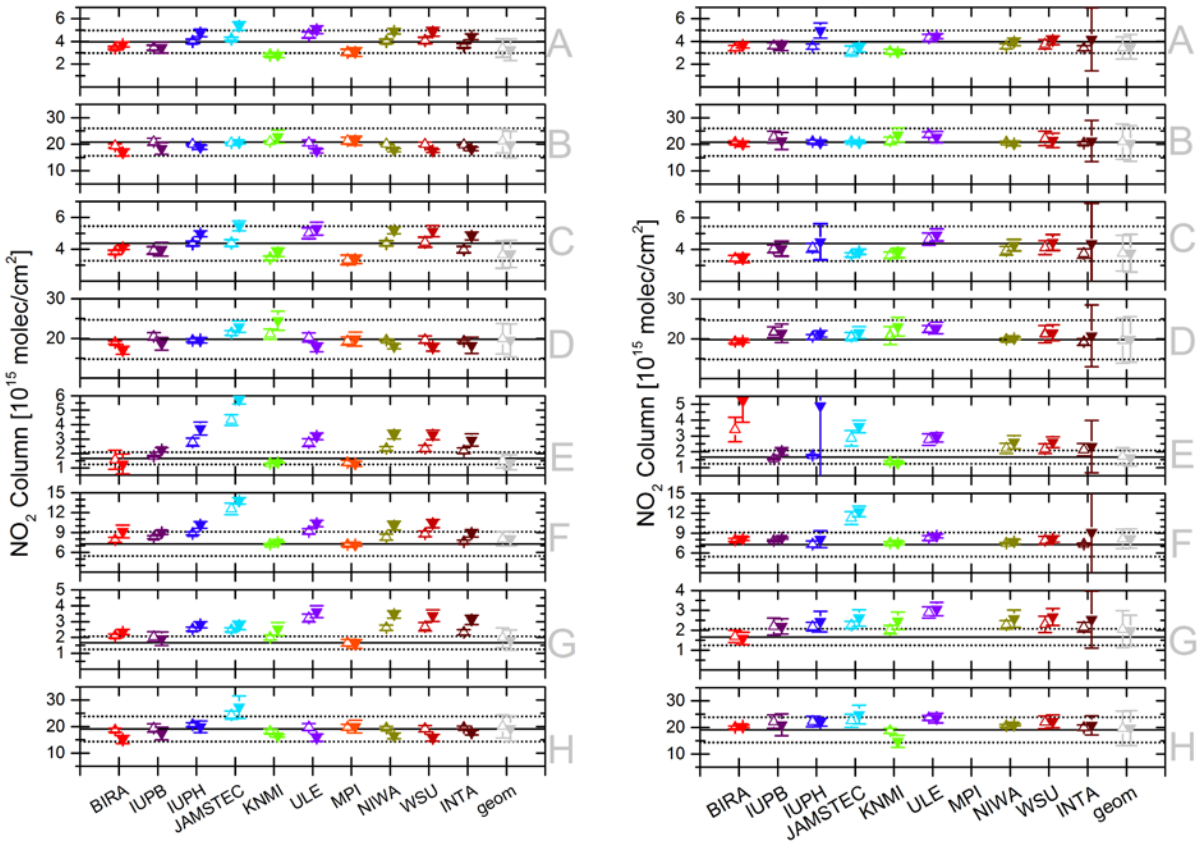

Figure 5.2: Results for the retrievals of tropospheric NO_2 columns on synthetic data in the UV (left) and visible (right). The black line indicates the true value, the dotted line the +/-25% range. Open symbols are for low aerosol cases, filled symbols for high aerosol scenarios. Error bars indicate the spread of values over the day.

It is interesting to also compare the spread of the values over the day as shown by the error bars. Overall, the variability of the results is rather small but can become large for some retrievals under certain scenarios. Generally, the scenarios with high aerosol load lead to larger variability for all retrievals with very few exceptions, but results vary between the groups with no obvious systematic. For example, BIRA results have usually low variability but for the very shallow layer and low NO_2, the spread of values is large while KNMI has an exceptionally small spread for the same model run. The reason for the different variations is not clear – possible explanations are instabilities in the retrieval, different aerosol approximations having an impact on the consistency of the retrievals under varying relative azimuth angles or inconsistencies between the radiative transfer models used by the individual groups and LIDORT, which was applied for the synthetic data calculation.

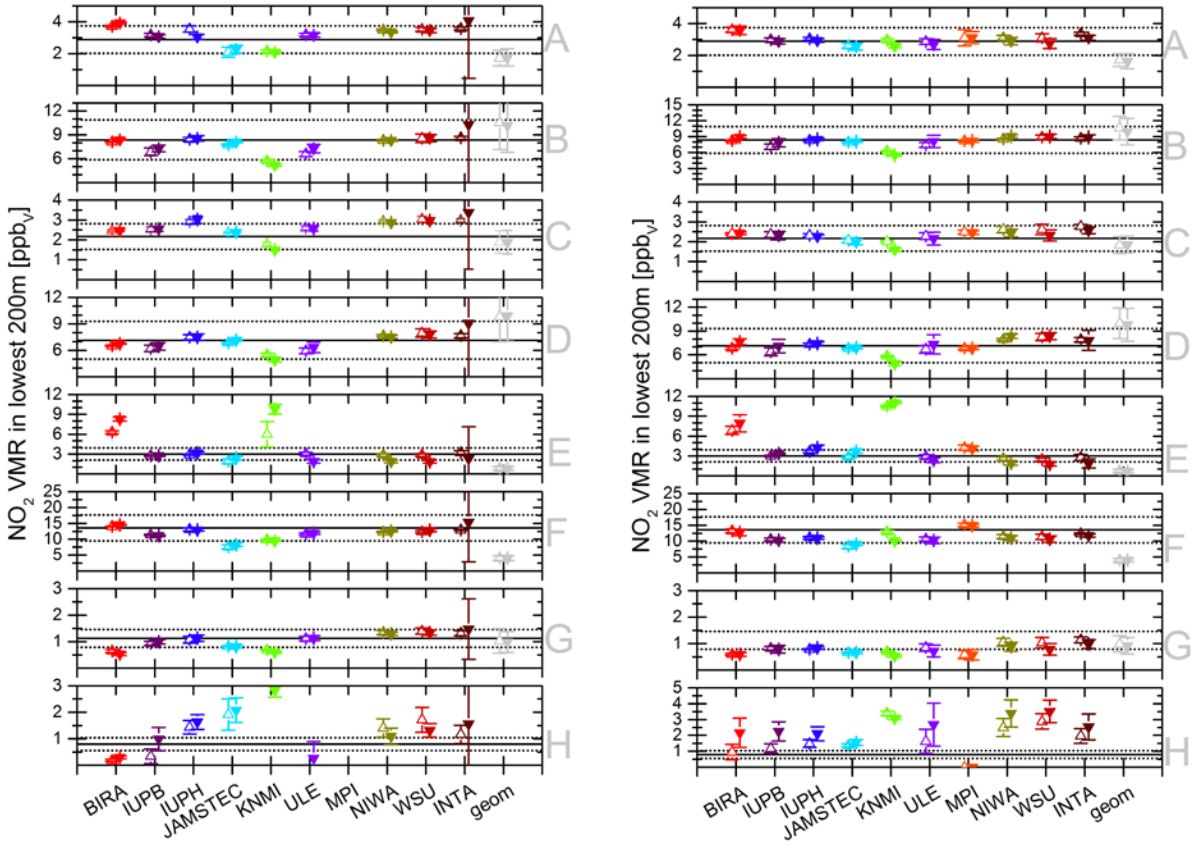

Figure 5.3: Results for the retrievals of NO_2 surface mixing ratios on synthetic data in the UV (left) and visible (right). The black line indicates the true value, the dotted line the +/-25% range. Open symbols are for low aerosol cases, filled symbols for high aerosol scenarios. Error bars indicate the spread of values over the day.

Results for the retrievals at the visible wavelength are very similar to those from the UV but show overall smaller deviations from the true values. This can be explained by the larger signal and the longer light path which both increase the sensitivity to the vertical NO_2 distribution. No attempt was made for a

retrieval using both wavelengths as is sometimes applied to real data in order to further constrain the vertical profiles.

An interesting observation is the fact, that the simple geometric approximation where only the 30° viewing direction is used (for which the geometric airmass factor (*1 /sin(elevation)*) takes the value of 1) performs surprisingly well on the daily averages. In fact, the geometric tropospheric column is within the 25% limits for all scenarios, regardless of whether the low or the high aerosol scenario is used. This is a relevant result as many previous studies have applied this approximation in spite of its well-known deficiencies. The variability of the geometric columns, however, is larger over the day and this can be linked to the impact of the relative azimuth angle (the geometrical approximation loses its relevance for measurements close to the sun).

The second quantity of interest, the NO_2 mixing ratio at the surface shows even better results than the tropospheric column (see Figure 5.3). This is somewhat surprising as it should be more sensitive to the a priori assumptions, but with the exception of the scenario with an elevated layer, nearly all retrievals perform very well. In contrast to the situation for the columns, the high aerosol situations overall do not lead to larger errors in the surface mixing ratios although there is a tendency for larger variability. As expected, the scenarios with elevated NO_2 layers lead to large deviations at the surface, in particular for the high NO_2 case.

In a second set of comparisons, all groups used their own data and their own “best settings” retrievals. The results are then compared to complementary measurements from the in-situ instrument operated by EMPA, with focus on the 5 “Golden days” of the campaign. The results of the comparison are shown in Figure 5.4, and further quantified in Table 5.1 and Table 5.2 which present statistics of regression analyses against in-situ data. As can be seen, the in-situ instrument reports large NO_2 mixing values in the morning, a rapid decrease towards noon and a moderate increase to the evening for all days. This variation by more than a factor of 6 over the day is linked to both photochemistry and the diurnal cycle of the boundary layer depth which was small in the morning and increased as it became warm during the day. This is a particularly challenging scenario for the MAX-DOAS observations as shallow layers are difficult to resolve. Nevertheless, all of the retrievals yield the right magnitude of the surface mixing ratios and also at least part of the diurnal and day-to-day variability. This includes both the optimal estimation based and the parameterized inversions. It is however also clear, that nearly all the retrievals have problems with the high NO_2 values early in the morning. From Figure 5.4 and Table 5.1, it can be seen that there are significant differences between the individual retrievals concerning the agreement of results with the independent observations. This could be the result of measurement uncertainties, specific assumptions made in the retrievals, use of different filtering approaches for cloud conditions, aerosols, and convergence of the retrievals. In particular the limited vertical resolution of MAXDOAS retrievals is expected to cause problems in the presence of a shallow boundary layer. This is confirmed by the fact that comparison results are significantly improved by excluding data taken at mixing layer heights smaller than 500m (see Table 5.2). In addition, it must be noted that not all instruments were located at exactly the same site (see Piters et al., 2012 for details) and therefore might have experienced slightly different NO_2 distributions.

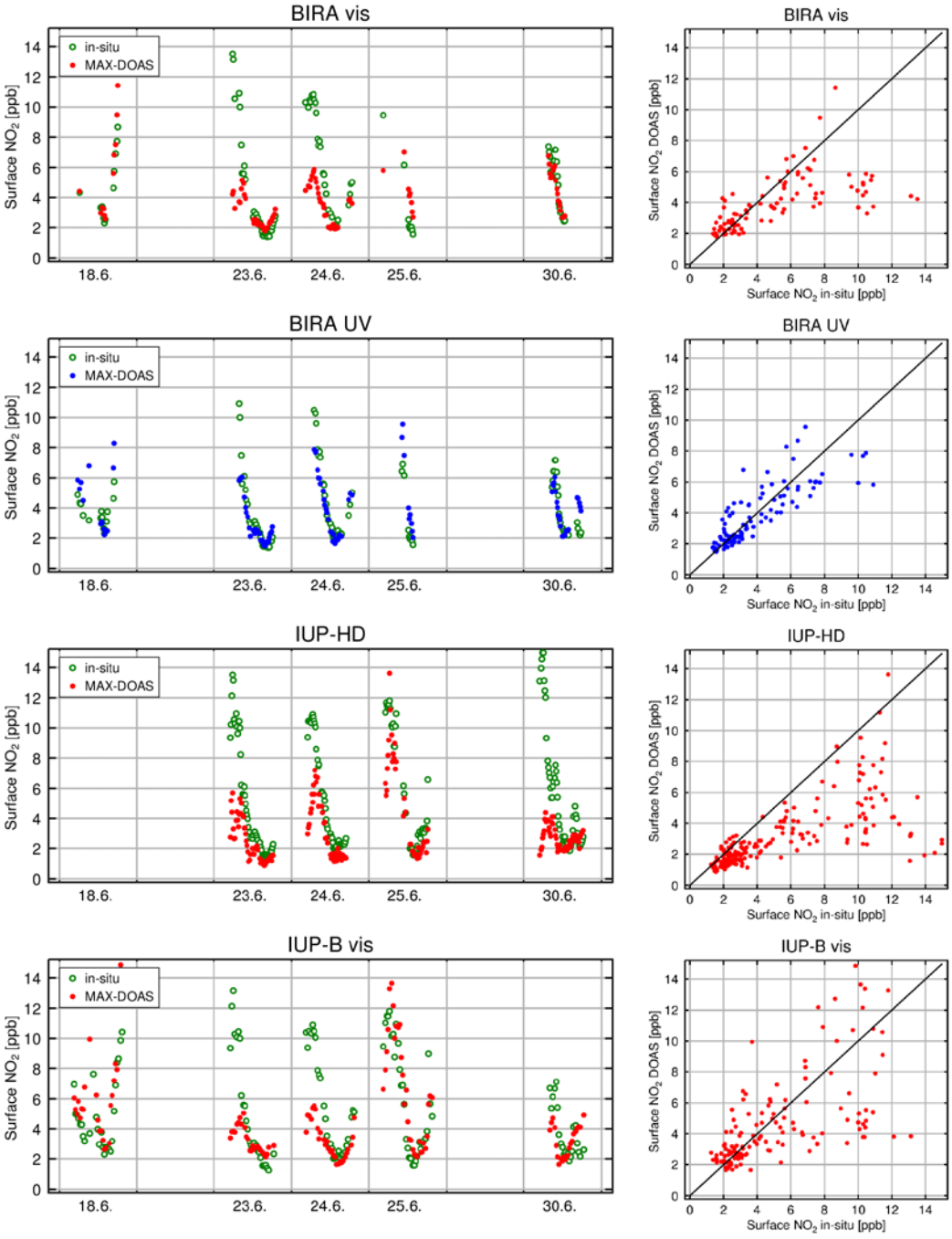
BIRA vis
in-situ
MAX-DOAS
Surface NO2 [ppb]
18.6.
23.6.
24.6.
25.6.
30.6.
BIRA vis
Surface NO2 DOAS [ppb]
Surface NO2 in-situ [ppb]
BIRA UV
in-situ
MAX-DOAS
Surface NO2 [ppb]
18.6.
23.6.
24.6.
25.6.
30.6.
BIRA UV
Surface NO2 DOAS [ppb]
Surface NO2 in-situ [ppb]
IUP-HD
in-situ
MAX-DOAS
Surface NO2 [ppb]
18.6.
23.6.
24.6.
25.6.
30.6.
IUP-HD
Surface NO2 DOAS [ppb]
Surface NO2 in-situ [ppb]
IUP-B vis
in-situ
MAX-DOAS
Surface NO2 [ppb]
18.6.
23.6.
24.6.
25.6.
30.6.
IUP-B vis
Surface NO2 DOAS [ppb]
Surface NO2 in-situ [ppb]

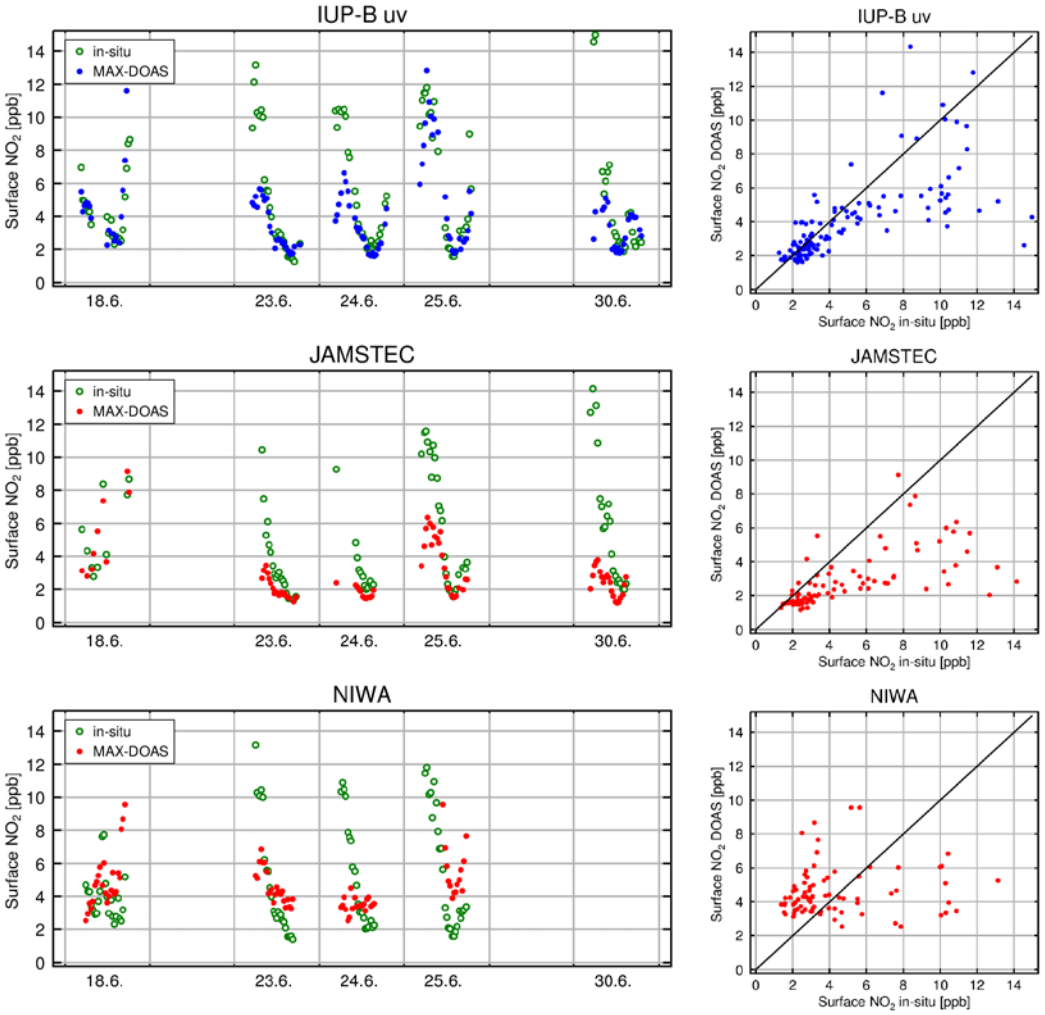
IUP-B uv
in-situ
MAX-DOAS
Surface NO2 [ppb]
18.6.
23.6.
24.6.
25.6.
30.6.
IUP-B uv
Surface NO2 DOAS [ppb]
Surface NO2 in-situ [ppb]
JAMSTEC
in-situ
MAX-DOAS
Surface NO2 [ppb]
18.6.
23.6.
24.6.
25.6.
30.6.
JAMSTEC
Surface NO2 DOAS [ppb]
Surface NO2 in-situ [ppb]
NIWA
in-situ
MAX-DOAS
Surface NO2 [ppb]
18.6.
23.6.
24.6.
25.6.
30.6.
NIWA
Surface NO2 DOAS [ppb]
Surface NO2 in-situ [ppb]

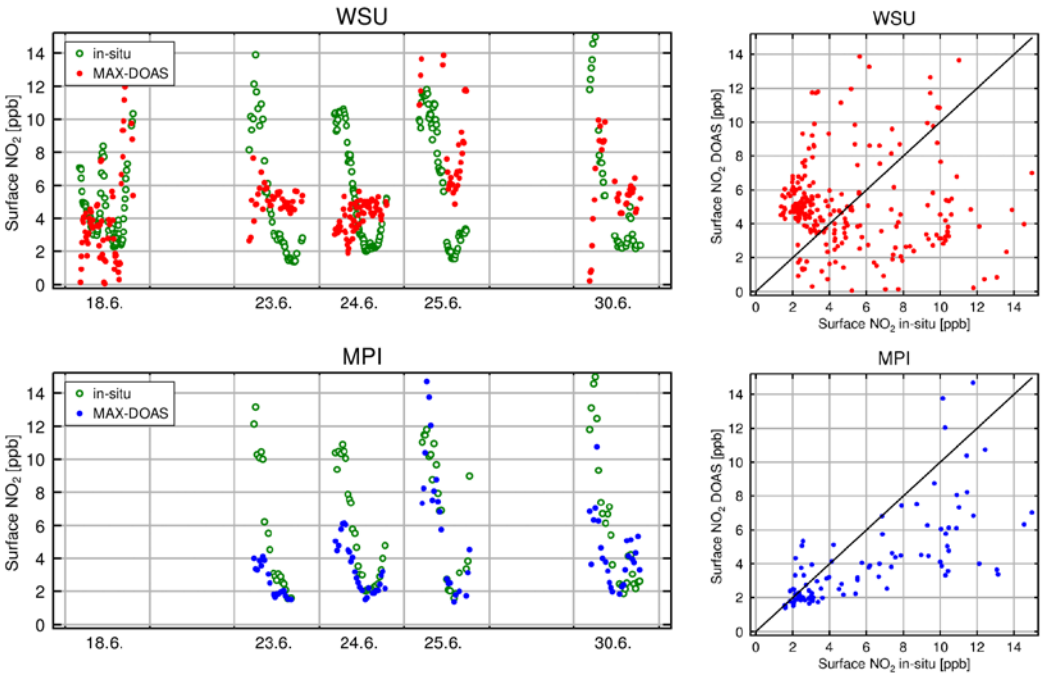

Figure 5.4: Comparison of in-situ (EMPA) measurements of surface NO_2 and MAXDOAS retrieved surface mixing ratios for the 5 golden days (18.6., 23.6., 24.6., 25.6., 30.6.2009). Each group has applied their own data selection. Red figures are for retrievals using the visible spectral range, blue data are from UV instruments.

Table 5.1: Statistics of scatter plots between EMPA in-situ observations and MAX-DOAS surface mixing ratios. All available data from the Golden Days have been used

Instrument	**N**	**Correlation**	**Slope**	**Offset [ppb]**
NIWA	89	0.5321	0.8295	2.1286
JAMTEC	84	0.6132	0.2864	1.4076
BIRA uv	104	0.8238	0.6843	1.1124
BIRA vis	98	0.6288	0.3454	2.1635
IUP-HD vis	186	0.6841	0.3793	1.0641
IUP-UB vis	133	0.6360	0.5877	1.6193
IUP-UB uv	116	0.6405	0.5134	1.5421
WSU	278	0.3820	0.7947	2.8742
MPIC	92	0.6968	0.4943	1.1658

Table 5.2. As but excluding data taken at mixing layer heights smaller than 500m

Instrument	N	Correlation	Slope	Offset [ppb]
NIWA	69	0.5866	1.0654	1.5610
JAMTEC	62	0.7503	0.4476	0.8026
BIRA uv	94	0.8036	0.7788	0.8153
BIRA vis	74	0.7346	0.4978	1.5622
IUP-HD vis	128	0.8300	0.4977	0.6200
IUP-UB vis	98	0.7231	0.8067	0.8610
IUP-UB uv	81	0.7575	0.6534	0.9417
WSU	190	0.4966	1.2871	1.5333
MPIC	62	0.7246	0.5137	1.0757

In summary, it can be concluded that reliable surface mixing ratios can be derived from MAXDOAS inversions not only on synthetic data but also on real observations. The uncertainties on the retrieved values vary between instruments and algorithms in a range of 20 to 60%, and for the best data set (BIRA-UV) result in a correlation of 0.8 which is considered to be excellent. In the presence of very shallow boundary layers, most of the retrievals either fail or yield too low NO_2 mixing ratios because of the limited vertical resolution of the MAXDOAS measurements.

5.1.2 Tropospheric NO_2 columns retrieved from zenith-sky DOAS observations

An algorithm dedicated to the retrieval of tropospheric NO_2 vertical column densities (VCDs) from ground-based zenith-sky measurements of scattered sunlight has been developed at BIRA in collaboration with the SAOZ team from LATMOS. It is based on a four-step approach consisting of (1) the DOAS analysis of zenith radiance spectra using a fixed reference spectrum corresponding to low tropospheric NO_2 content in order to increase the sensitivity to the troposphere, (2) the determination of the residual amount in the reference spectrum using a Langley-plot-type method, (3) the removal of the stratospheric content from the derived daytime total slant column using stratospheric vertical columns measured at twilight and simulated stratospheric NO_2 diurnal variation, (4) estimation of the tropospheric vertical columns by dividing the resulting tropospheric slant columns by appropriate airmass factors. The retrieval algorithm has been tested on the 2 month dataset acquired during the CINDI campaign by the BIRA MAX-DOAS instrument and retrieved VCDs have been compared to off-axis and direct-sun measurements from the same instrument as well as to data obtained by applying a similar method to a co-located SAOZ (Système d'Analyse par Observations Zénithales) spectrometer operated by LATMOS. First results show a good overall agreement between the different data sets (see Figure 5.5) with correlation coefficients and slopes close or larger than 0.8.

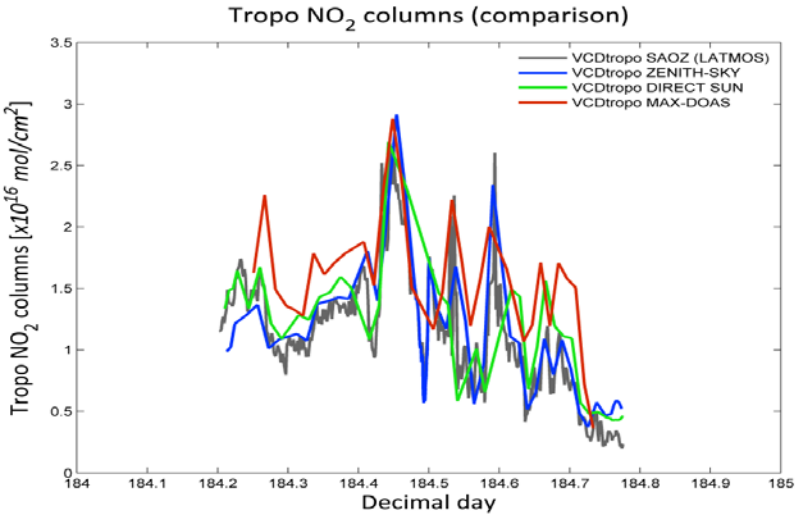

Figure 5.5: Comparison of tropospheric NO_2 VCDs retrieved from zenith-sky (BIRA + SAOZ spectrometers), direct-sun (BIRA spectrometer), and off-axis (BIRA spectrometer) measurements performed on July 3rd 2009 during the CINDI Campaign.

The main sources of error originate from the determination of the residual NO_2 amount in the reference spectrum, the stratospheric NO_2 abundance and its diurnal variation, and the tropospheric and stratospheric NO_2 air mass factors. Among these, the most critical parameters are the residual amount in the reference spectrum (for highly polluted situations) and the stratospheric NO_2 correction (for moderately and weakly polluted conditions). This study demonstrates zenith-sky measurements, which have been commonly used for many years to monitor the stratosphere, can be also be used for the retrieval of tropospheric NO_2 column amounts, offering new perspectives for the exploitation of historical zenith-sky UV-Vis datasets archived at NDACC stations.

5.1.3 Development of a generic cloud screening method for DOAS instruments

To better characterize MAX-DOAS measurements taken under cloudy conditions, BIRA-IASB has developed a cloud-screening method based on the colour index (CI) of the sky in the zenith geometry:

$$CI = I_{Low\ wavelength}/I_{High\ wavelength}$$

Given the above definition of the CI, high CI values correspond to clear-sky conditions, while lower CI values indicates the presence of clouds, aerosols, or fog/haze. Using the CI combined to radiative transfer calculations under various sky conditions for the determination of the different CI thresholds, 3 different sky conditions can be defined: bad (=full thick cloud cover/extreme aerosols), mediocre (=thin clouds/aerosols) and good (=clear sky). This cloud conditions classification is illustrated for the Xianghe station (Beijing suburban area; 39.75°N, 116.96°E) in Figure 5.6.

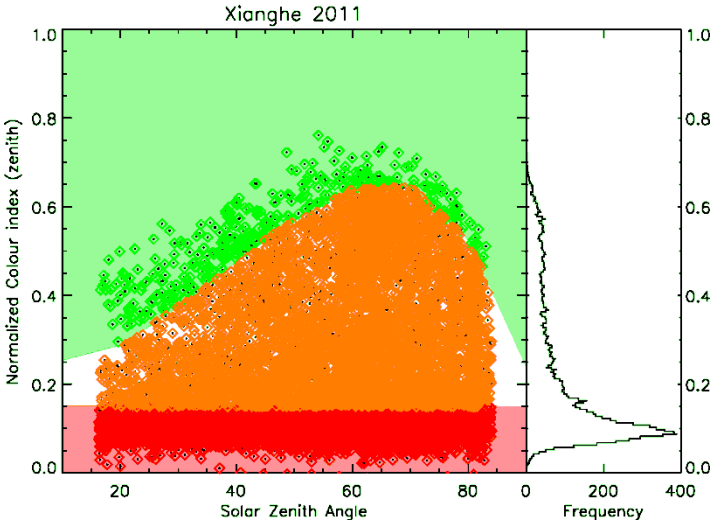

Figure 5.6: Classification of sky conditions for each MAX-DOAS scan at the Xianghe station (China) in 2011 based on the CI ($I_{405\ nm}/I_{670\ nm}$). Green is for clear-sky, red for bad conditions (full thick cloud/extreme aerosols), and orange is for mediocre/intermediate conditions (thin clouds/aerosols).

Because of the significant impact of broken clouds on MAX-DOAS observations, a dedicated flag has been developed based on the modeling of the CI diurnal variation with a double-sine function and the detection of outliers corresponding to a sudden change of the sky conditions above the MAX-DOAS spectrometer due to the presence of broken clouds.

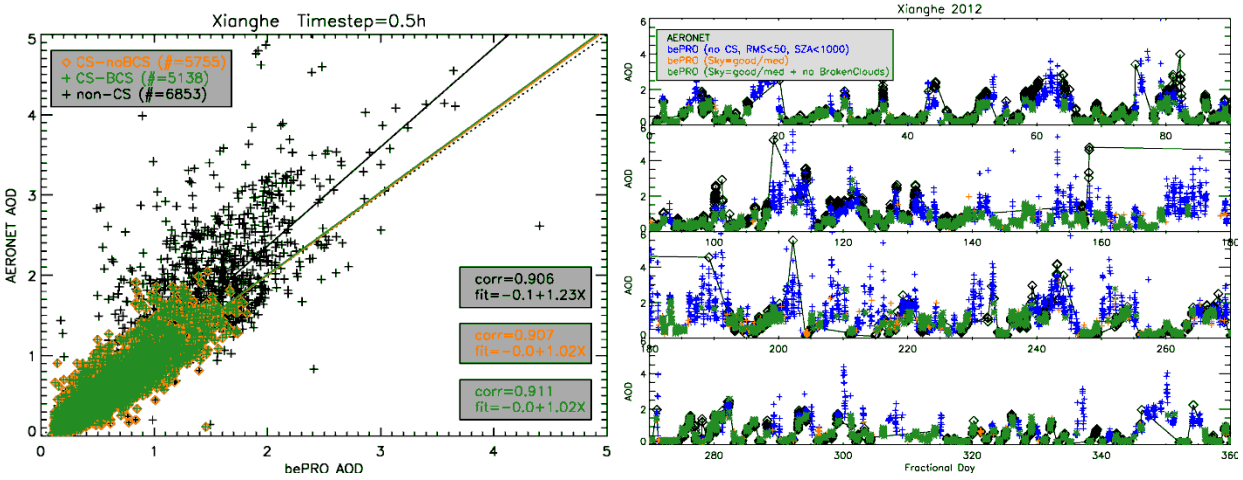

Figure 5.7: Left panel: Comparison of AOD retrieved by applying the bePRO profiling tool (Clémer et al. 2010) to MAXDOAS O_4 measurements at Xianghe and collocated AERONET data. In black the AERONET data, blue the non-cloud-screened MAXDOAS data, orange the cloud-screened data under good/mediocre conditions, green the good/mediocre data with additional removal of data hindered by broken clouds. Right panel: Corresponding correlation between MAXDOAS and AERONET AODs. In black the non-cloud-screened MAXDOAS data, green and orange are defined the same as in the left panel.

Removing data under bad-sky and broken-cloud conditions generally results in a better agreement, in both correlation and slope, between the AERONET and MAX-DOAS AOD retrievals (see Figure 5.7). It is found that high MAX-DOAS AODs are removed, as they are now identified as due to clouds (Blue crosses in Figure 5.7, left panel).

Clouds can also have an impact on the agreement between satellite and MAX-DOAS data. This is illustrated in Fig. 8 where tropospheric NO_2 VCDs from the GOME-2 and OMI satellite instruments have been compared to MAXDOAS retrievals at the Xianghe station. These preliminary results show that the removal of MAXDOAS scans corresponding to bad sky conditions significantly improves the agreement with satellite data. Further investigations on this issue are currently under progress.

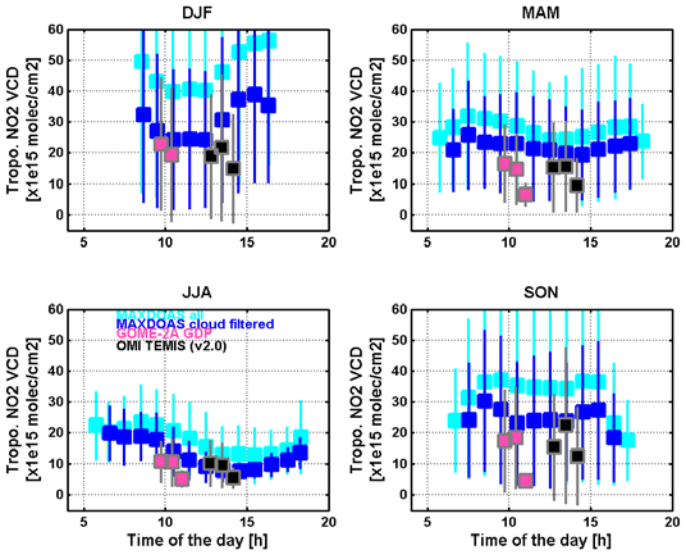

Figure 5.8: Comparison of seasonally-averaged tropospheric NO_2 VCD diurnal variations derived from satellite nadir (GOME-2, OMI) and MAXDOAS observations at Xianghe (Beijing suburban area). The following criteria have been used for the selection of satellite pixels: pixel center < 100km from the station; cloud fraction < 20%.

It should be noted that a similar more sophisticated (but also less generic) cloud flagging method based on the CI but also on other quantities like O_4 slant columns densities and their respective variation with the elevation and azimuthal angles has been recently developed by MPI-Mainz and successfully applied to CINDI Campaign measurements (Wagner et al., 2013).

5.2 Lessons learned from the CINDI campaign

The CINDI campaign has been largely successful in achieving its observational and scientific objectives. A large data set of continuous ground-based in-situ and remote sensing observations of nitrogen dioxide, aerosols and other air pollution constituents has been collected under various meteorological conditions and under various air pollution loadings.

A main objective of the CINDI campaign was to determine the potential of ground-based NO_2 observations for validation of tropospheric NO_2 columns derived from satellite observations such as, e.g. OMI aboard EOS-Aura, SCIAMACHY aboard Envisat, GOME-2 aboard METOP and the future Copernicus

GMES Sentinels 4, 5 and 5 Precursor. One key aspect is the accuracy of the determined tropospheric columns and vertical profiles, which is obtained by quantifying the performance of the measurements and retrieval methods under different atmospheric conditions. The CINDI data set has allowed to address this issue in several ways:

- Intercomparison of NO_2, O_4 (Roscoe et al., 2010) and HCHO (Pinardi et al., 2013) slant columns and recommendations for harmonized processing of these species
- Intercomparison of different NO_2 profile inversion methods (Wittrock et al., to be submitted)
- Intercomparison of AOD and aerosol surface extinction (Zieger et al., 2011)
- Intercomparison of aerosol profile retrieval methods (Friess et al., to be submitted)
- Demonstration of multi-species MAXDOAS retrievals (Irie et al., 2011)
- Demonstration of a new NO_2 sonde technique for high-resolution profile measurement in the troposphere (Sluis et al., 2010)

Regarding the process of intercomparing a large number of instruments (24 optical systems were intercompared during CINDI) several lessons have been learned. In particular:

- The need for suitable infrastructures. Local hosting was particularly dedicated and efficient during CINDI, and this contributed a lot to the success of the campaign
- The need for adequate preparation ahead of the campaign, sizing of rooms, renting of containers, sizing of power supplies, etc
- The need for optimal synchronization of the systems. This aspect was not optimal during CINDI since no requirements had been formulated ahead of the campaign on the operation settings (e.g. sets of common elevation angles, synchronization of acquisitions, exchange of information on instrument field of view, etc).
- The need for calibration facilities on site (even if limited in scope), and ideally to plan for a calibration period before starting the intercomparison
- The need for a campaign referee. The CINDI semi-blind intercomparison was managed by an independent referee who was tasked to collect data from all group, organize of quick look analysis and daily discussions. The semi-blind intercomparison approach, which had been adopted already in two previous NDACC intercomparisons, again proved to be particularly successful.

When comparing ground-based and satellite-borne remote-sensing observations, an important aspect to be taken into consideration is their difference in sensitivity to trace gas abundances as a function of the altitude. This characteristic of any remote sensing system, often quantitatively described using the Averaging Kernel (AK) concept, can be determined using radiative transfer model calculations or ray tracing through the atmosphere. The CINDI data have shown that trace gas and aerosol profile information from MAX-DOAS data can be usefully combined with column information to provide insight into the satellite retrieval uncertainties along the vertical axis.

Another equally important aspect to be considered is the difference in spatial and time sampling of the satellite and ground-based measurements. Typically the satellite observes ground-pixel footprints at the 30 to 100 km scale (which will be reduced to less than 10 km with the Sentinels), while the ground-based MAXDOAS horizontal field of view is typically of a few km in the viewing direction and a few 100m in the across viewing direction. Mobile measurements performed during CINDI which spanned an area of approximately $30\times40km^2$ have shown a range in NO_2 values of a factor of 6 or even more. This

variability is averaged over the satellite ground pixel footprint and actually provides the largest contribution to the noise of satellite versus ground-based comparisons in urban and sub-urban areas. Therefore, there is a need to better characterize this variability and its impact on the validation of satellite-borne measurements of short lived species such as NO_2 or HCHO. This aspect has only been partly addressed during CINDI and more has to be done in future experiments. To address and quantify the impact of the spatial variability on remote-sensing measurements, fixed ground-based systems should be combined with mobile measurements and high-resolution imaging measurements from aircraft or UAV. A first step into this direction has already been taken as part of the MADCAT campaign in Mainz during summer 2013 (see section 5.4), but more is needed.

Finally one important aim of the CINDI campaign was to provide a forum for discussion, experimentation, and definition of best practices that could benefit to the overall DOAS/MAXDOAS community, e.g. as part of the activities of the NDACC network. Owing to the CINDI results, a better homogeneity between the different MAXDOAS stations has been obtained through the use of CINDI recommendations, formulated for NO_2, O_4, HCHO, and aerosol retrievals. Another outcome has been the development of standardized cloud screening methodologies, allowing for automated QA/QC of MAXDOAS aerosol and trace gas retrievals that can be strongly affected by clouds. At BIRA in particular, large efforts have been devoted to the development of automated retrieval processes for DOAS and MAXDOAS products allowing for NRT submission of level-2 products to Cal/Val databases. Finally GEOMS compliant metadata HDF templates compatible with all UV-Vis geometries and products have been developed and demonstrated.

5.3 MAXDOAS developments addressing other air quality trace gases

In addition to tropospheric NO_2 which is a key product of the MAXDOAS technique and was a central focus in the CINDI campaign, other gases of interest can also be measured, in particular HCHO, SO_2, glyoxal, O_3, BrO, HONO, IO, O_3, water vapor, etc. In this section, we highlight results from recent MAXDOAS developments concentrating on HCHO, SO_2 and HONO retrievals. This work is based on MAXDOAS observations carried out by BIRA in the sub-urban city of Xianghe, China. Xianghe is located approximately 50 km to the East of Beijing in a region influenced by sources coming from three major surrounding cities (Beijing, Tianjin and Tangshan). The potential of these measurements for satellite validation is discussed.

5.3.1 Retrieval of tropospheric SO_2 and HCHO

Tropospheric SO_2 vertical profiles and corresponding column densities have been retrieved at the Xianghe station which has been set up in collaboration with IAP/CAS in early 2010. The BIRA vertical profiling Optimal Estimation code (be-Pro, Clémer et al., 2010) has been applied to the complete series of ground-based MAX-DOAS observations performed from March 2010 to February 2013 (Wang et al., 2014). The spectral retrieval was performed in the 305-317.5 nm wavelength interval which was found to provide best compromise in terms of S/N ratio and accuracy for near-noon conditions up to 70° SZA. For verification purpose, retrieved SO_2 surface concentrations have been compared to collocated in-situ data (see Figure 5.9). An excellent agreement was found, with correlation coefficient and slope close to 0.9, demonstrating the reliability and robustness of our retrievals.

These MAX-DOAS measurements have then been used to investigate the seasonal and diurnal cycles of SO_2 vertical columns and surface concentrations, in combination with meteorological data

(temperature, humidity, and wind speed and direction). Regarding the seasonal variation, both VCD and surface concentrations exhibit the same patterns (see Figure 5.10), with a maximum in winter (February) and a minimum in summer (July), in accordance with the large emissions due to domestic heating in winter. The high levels of SO_2 during the cold season are further enhanced by the weakness of the wet deposition mechanism and the frequent temperature-inversion events occurring during this period, favoring the accumulation of SO_2 in the atmospheric layers close to the surface.

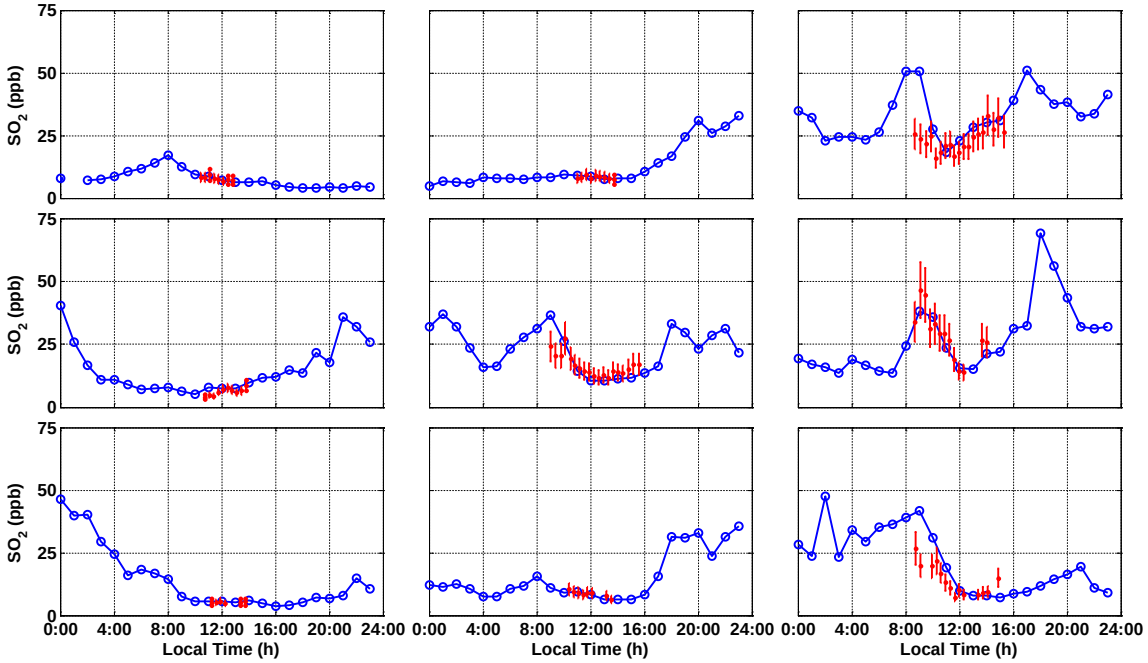

Figure 5.9: Comparison between in situ (blue, hourly means) and MAX-DOAS SO_2 surface concentrations (red, each point represents the retrieval from one scan) for the December 15-23, 2011 period.

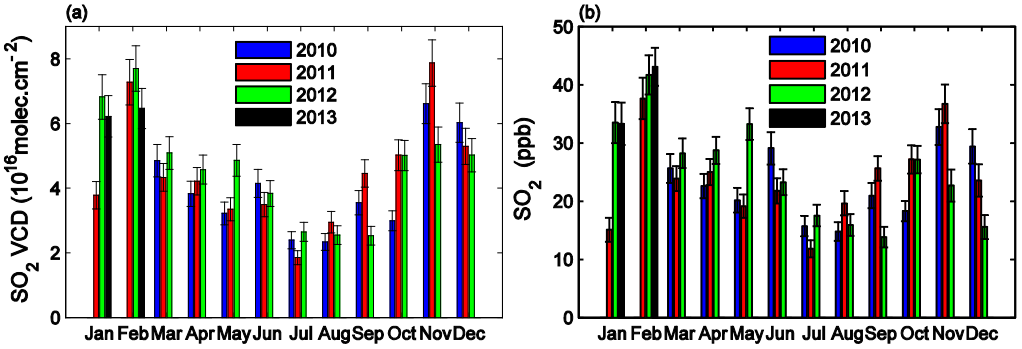

Figure 5.10: Monthly mean SO_2 VCDs (a) and surface concentrations (b) for the March 2010 - February 2013 period.

These three-year MAX-DOAS SO_2 measurements in Xianghe represents so far a unique demonstration data set for validating and improving space-borne observations over China, which is the region in the world where anthropogenic SO_2 emissions are the largest. In particular, retrieved SO_2 vertical profiles

(see Figure 5.11) can be used to verify the a priori profile information utilized for the calculation of airmass factors in satellite retrievals. Moreover, the combination of both integrated columns and surface concentrations could provide useful information to make explicitly the link between measured satellite columns and surface concentrations.

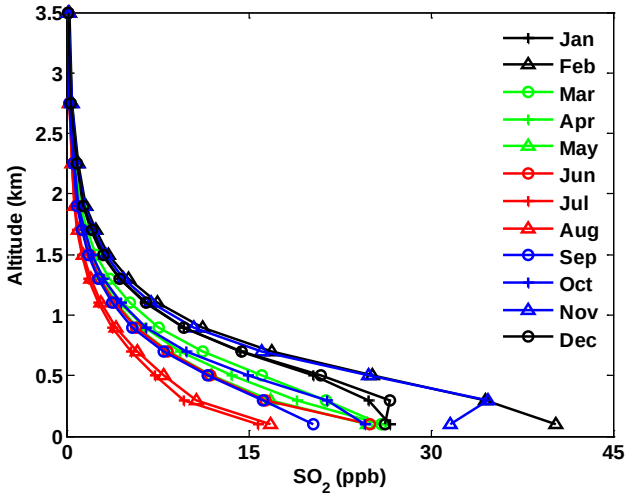

Figure 5.11: Monthly-averaged SO_2 concentration vertical profiles for the March 2010 - February 2013 period.

The potential of these observations for satellite validation is further illustrated in Figure 5.12 where monthly averaged MAXDOAS SO_2 columns are compared to OMI measurements. The OMI data used in this study have been processed at BIRA using a prototype algorithm recently developed in preparation of the Sentinel-5 Precursor/ TROPOMI mission (Theys et al., S5P ATBD, July 2013). This algorithm uses a multiple-window DOAS approach optimized for accurate determination of SO_2 columns under a very large range of column values. The algorithm also features advanced background corrections allowing for bias-free detection of small anthropogenic signals.

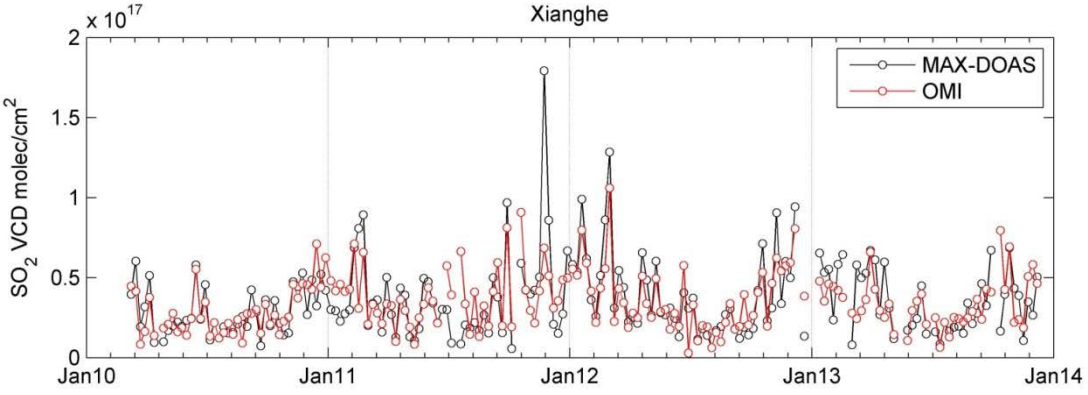

Figure 5.12: Comparison of weekly averaged SO_2 vertical columns measured in Xianghe from January 2010 until December 2013 by the BIRA MAXDOAS instrument and OMI/Aura retrievals. Satellite overpass data have been averaged in a circular area of 200 km radius around Xianghe.

For the Xianghe analysis, the SO_2 profile shape information derived from MAXDOAS measurements has been injected into the satellite retrieval algorithm, allowing for a fully consistent comparison. As can be seen, an excellent agreement is found when satellite and ground-based measurements use consistent vertical profile shape information. Such a result consolidates our trust in the ability of UV backscatter satellite instruments to detect and quantify SO_2 signals of anthropogenic origin. Future work will focus on applying the same algorithmic approach to GOME-2 measurements and on investigating the potential of UV sensors for inverse modelling of SO_2 emissions at the global scale.

Also based on MAXDOAS measurements in Xianghe and in Beijing, a similar study has been performed for formaldehyde. HCHO columns and profiles have been retrieved using the BIRA be-Pro OE code for the period from July 2008 until December 2011. In Figure 5.13, these columns are represented in comparison with satellite measurements obtained at BIRA using the OMI instrument, again in the context of the S5P Level-2 algorithm development.

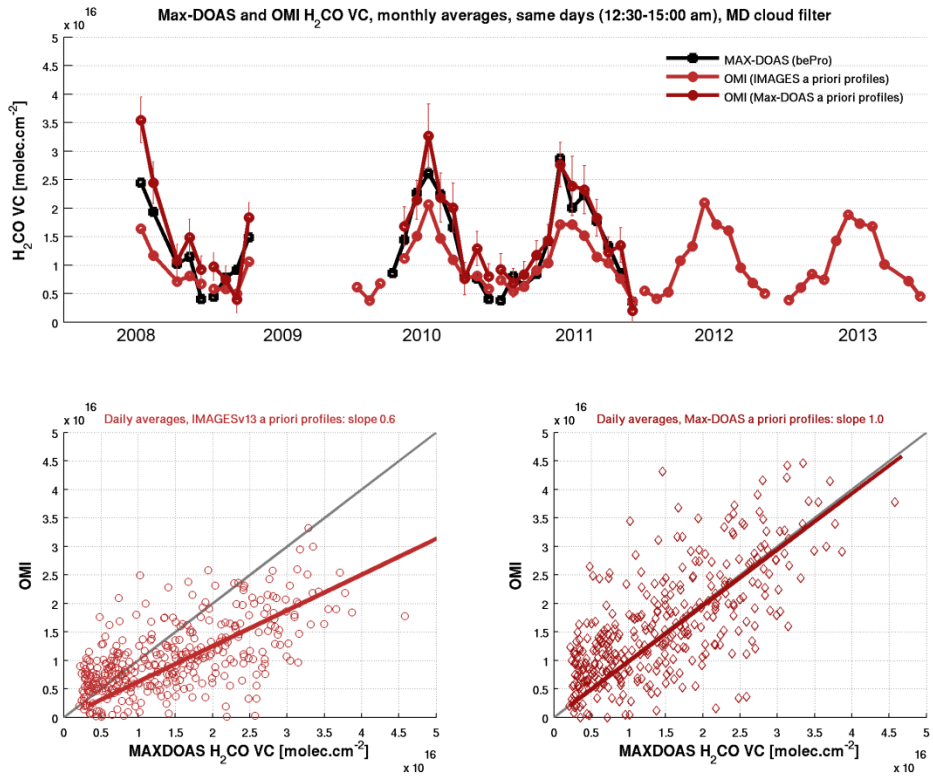

Figure 5.13: Comparison between HCHO columns derived from MAXDOAS measurements in Beijing (2008-2009) and Xianghe (2010-2011), and from OMI satellite observations. Results highlight the impact of the HCHO profile shape uncertainty on the satellite results. Comparisons using HCHO vertical profiles derived from MAXDOAS measurements as an input for the satellite retrievals are largely improved in comparison to the standard retrieval using model profiles (IMAGES).

In this case, the impact of the a-priori profile shape used in the satellite retrievals is illustrated. As can be seen, standard retrievals using HCHO vertical profiles simulated by a 3D-CTM (IMAGES) tend to underestimate HCHO columns while the agreement with ground-based measurements is largely improved when MAXDOAS profiles are used for the calculation of satellite air mass factors. This again illustrate the potential of the MAXDOAS technique to validate air quality data product and provide insight into the satellite retrieval process.

5.3.2 Retrievals of HONO and NO_2

HONO is a key chemical species in the troposphere, due to its significant role in the nitrogen oxides (NO_x) and hydrogen oxides (HO_x) cycles. The heterogeneous conversion of NO_2 on wet organic and inorganic ground surfaces (soil, buildings, vegetation, and aerosols) is believed to be a major source of HONO, while HONO photolysis, which is a major source of OH radicals, its main sink. Although HONO has not been detected so far from space, we have shown in a recent study published in ACP (Hendrick et al., 2013) that this molecule can be accurately detected from MAXDOAS measurements in polluted urban areas such as the Beijing megacity and Xianghe, China. In contrast to previous HONO observations mainly based on field campaigns using surface in-situ techniques, MAXDOAS measurements allowed for the first time the investigation of the seasonal cycle of HONO as well as its diurnal variation over several years of observations.

Results displayed in Figure 5.14 show that HONO and NO_2 near-surface concentrations and VCDs exhibit the same marked seasonality, with a maximum in late fall/winter and a minimum in summer.

The strong link between HONO and NO_2 is further supported by the high correlation of HONO with NO_2 found throughout the year, with coefficients comprised in the 0.7-0.9 and 0.5-0.8 ranges at Beijing and Xianghe, respectively (see Figure 5.15). Like NO_2, HONO is more abundant at Beijing than at Xianghe, with mean VMR ranging from ~0.1 to 0.8 ppb and from ~0.03 to 0.7 ppb, respectively. A strong role of NO_2 conversion to HONO at Beijing is suggested from the higher correlation coefficients between HONO and aerosol extinctions retrieved in the 0-200m layer at Beijing (ranging from 0.65 to 0.95 instead of 0.55 to 0.85 at Xianghe).

The diurnal profiles of HONO surface concentration and vertical column show a maximum in the early morning (1.3-1.6 ppb/1.5-1.8 x 10^{15} molec/cm^2 in Beijing and 0.7-1.0 ppb/0.9-1.1 x 10^{15} molec/cm^2 in Xianghe) likely explained by the photolysis of the HONO accumulated during the night. The subsequent decrease (to about 0.1-0.4 ppb for the concentration and 0.1-0.6 x 10^{15} molec/cm^2 for the vertical column around local noon) results mostly from a balance between HONO sources and the photolytic sink. Dilution effects appear to play only a minor role, given the observed very similar diurnal cycle of the HONO vertical column, which is expected to be insensitive to vertical transport variations.

This study showed that MAXDOAS is a useful technique for long-term monitoring of HONO near-surface concentrations and vertical column amounts in polluted areas. Multi-year data sets of HONO, NO_2, and aerosol observations, such presented in this work, offer a better quantitative characterization of HONO photochemistry and can provide additional constraints to modelling studies. With the improvement of spatial resolution and S/N ratio expected from future UV nadir sensors (TROPOMI and Sentinels 4 and 5) the HONO detection might become possible from space, and in this case the MAXDOAS technique would provide suitable validation data sets complementing those of NO_2.

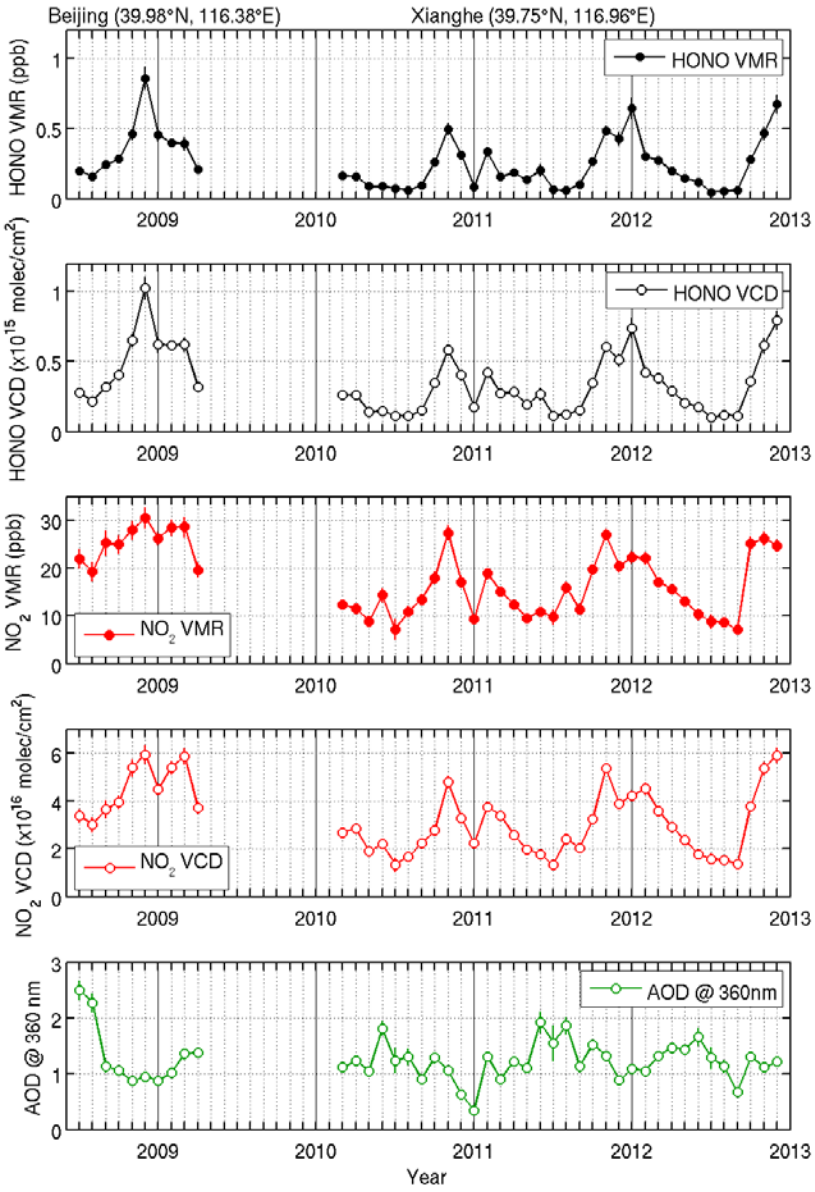

Figure 5.14: Time-series of monthly averaged HONO and NO_2 near-surface concentrations (filled circles) and vertical columns (VCD; empty circles) at local noon (±2h) at Beijing (July 2008-April 2009) and Xianghe (March 2010-December 2012). AODs at 360 nm retrieved from MAX-DOAS measurements appear in the lower plot. The error bars represent the standard deviation of the mean.

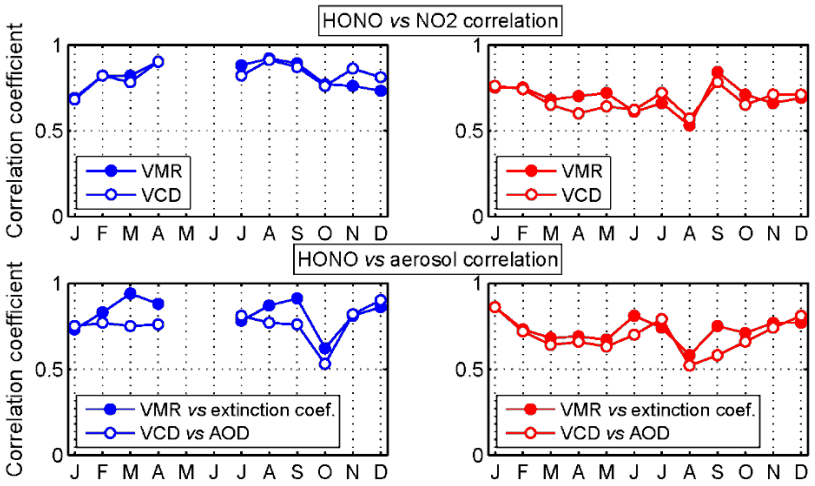

Figure 5.15: Seasonal variation of the HONO versus NO_2 and HONO versus aerosol correlation coefficients (0-200m VMR and vertical column density (VCD)) at local noon at Beijing (left plots) and Xianghe (right plots).

5.4 Contribution to the MAD-CAT Campaign

The MAD-CAT (Multi Axis DOAS – Comparison Campaign for Aerosols and Trace Gases) Campaign was held in June-August 2013 at MPI-Mainz in Germany (see Figure 5.16). Although it was initially planned as a trilateral campaign (MPI-Mainz, University of Heidelberg, and CAS (Hefei/China)), several other groups joined on a best-effort basis: BIRA-IASB, University of Colorado (USA), CAMS (Beijing/China), University of Bremen, NUST (Islamabad/Pakistan), University Minsk (Belarus), IISER (Mohali/India), and University of Galati (Romania).

The main objectives of MAD-CAT were the comparison of NO_2, HCHO, CHOCHO, H_2O, O_4, HONO differential slant columns densities, which are the direct product of the DOAS spectral analysis, investigation of cloud effects and azimuthal dependency, comparison of profile retrievals, and elevation angle adjustment. To achieve these goals, the following instruments were involved: 16 MAX-DOAS (among them 6 having azimuthal scan possibilities), 3 Car-MAXDOAS, 1 NO_2 cavity-enhancement (CE-) DOAS, collocated sunphotometer (AERONET) and ceilometer, IR-Cloud detection, all-sky-camera, + several air quality stations measuring NO_2, SO_2, PM2.5, PM10, humidity, wind, temperature in Mainz and Wiesbaden. In contrast to the CINDI campaign, the MAD-CAT had a much stronger focus on characterizing the horizontal variability of the NO2 field using a combination of MAXDOAS systems equipped of azimuthal scanners and mobile DOAS systems. The analysis of these interesting measurements is in progress and should provide a baseline for the design of more advanced experiments on the same subject in an upcoming campaign.

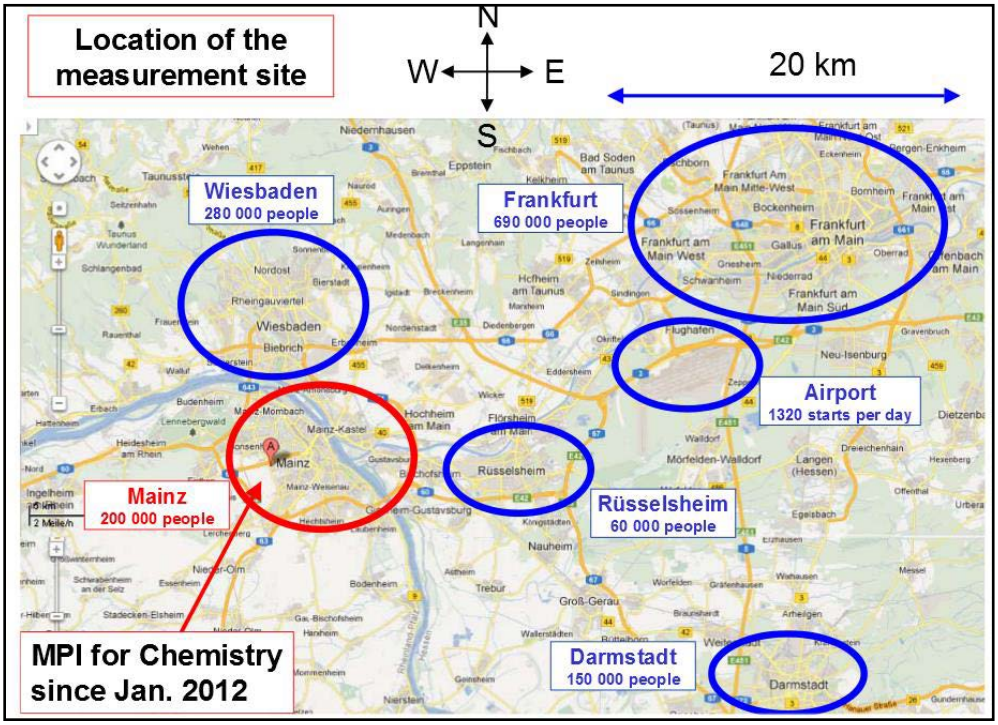

Figure 5.16: Location of the measurement site (© J. Remmers, MPI-Mainz).

During the campaign, one of the main tasks was to daily analyze measured MAXDOAS spectra and compare resulting NO_2 and O_4 DSCDs from the different groups. For this purpose, data format and DOAS fit settings were taken from the CINDI Campaign with some changes: new H_2O spectrum based on most recent spectroscopic parameters from the Hitran data base, orthogonalised low-temperature NO_2 cross-sections, I_0–corrected NO_2 cross-sections, order 5 polynomial. Figure 5.17 shows an example of NO_2 DSCDs comparison. A good overall agreement is obtained at low SZA between the different groups, while larger discrepancies are observed early in the morning, probably due to the presence of cirrus and broken clouds at that time.

Similar DSCD comparisons for other molecules are currently under progress, as well as comparisons between measurements performed with different techniques (e.g., MAXDOAS versus Car-MAXDOAS for NO_2, all-sky-camera versus MAXDOAS for the sky conditions, etc..).

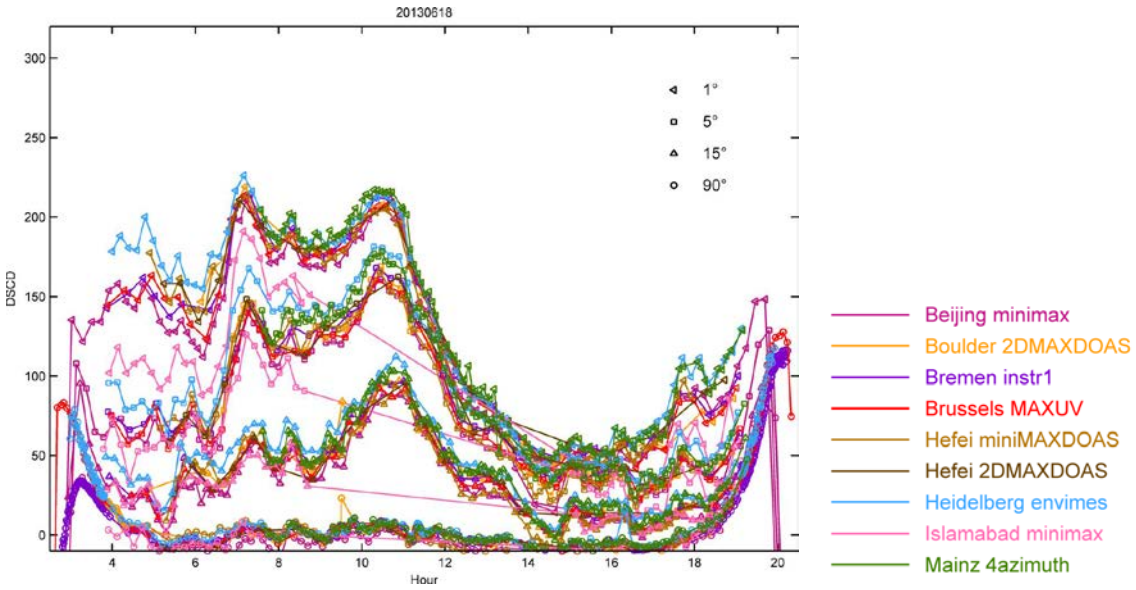

Figure 5.17: Example of comparison of NO_2 DSCDs during the MAD-CAT Campaign (18/06/2013). The cloud conditions were the following: fully cloudy or broken clouds till 8 am, then almost clear-sky (© J. Remmers, MPI-Mainz).

5.5 Progress towards harmonized MAXDOAS data processing and data reporting

5.5.1 Data file format harmonisation

In collaboration with the GEOMS Metadata Board (in particular, Ian Boyd from the University of Massachusetts), the NDACC UV-Vis Working Group has defined and adopted a common GEOMS-compliant HDF file format for reporting DOAS data. Its implementation has started within the framework of the FP7 project NORS (http://nors.aeronomie.be). In the first version of the file format, all variables corresponding to the three DOAS geometries (zenith, off-axis, and direct-sun) were declared as mandatory, with fill values for those which are not in use. Data users experienced problems with this format, due to the fact that files contain a large number of variables with fill values when only one geometry is reported. To solve this issue, a new version of the format has been created, with separate files for the three geometries (see http://avdc.gsfc.nasa.gov/index.php?site=1876901039 for more details), reducing therefore the number of variables with only fill values and facilitating automatic file reading processes. This new format is currently being implemented by the different NDACC/NORS UV-vis groups.

An important task has been also to implement in the GEOMS UV-Vis template a variable describing the cloud conditions for each MAXDOAS scan (possible values: clear-sky; thin clouds; thick clouds; broken clouds; + [empty] string for cloud retrieval not successful, not possible or missing) since clouds can have a significant impact on retrieval results as shown above. It has been decided that this variable will act as a warning for the quality of the corresponding MAXDOAS data but not as a full quality flag since cloudy scenes do not necessarily result in erroneous trace gas retrievals.

5.5.2 Automation of MAXDOAS retrievals

Also within the framework of the FP7 project NORS, some NDACC UV-Vis groups (BIRA-IASB, LATMOS, INTA, University of Bremen) have started the development of automated retrievals for zenith-sky and MAXDOAS products. At BIRA-IASB, automated daily retrievals are currently operational for MAXDOAS aerosols and NO_2 products at the Xianghe station (China) and for stratospheric O_3 and NO_2 VCDs at Jungfraujoch. Corresponding GEOMS HDF files are automatically submitted to the NORS/NDACC rapid delivery (RD) database by ftp on a daily basis. Monthly files are also submitted in an automatic way.

The operational chain is described in Figure 5.18 and includes the following 5 main steps:

1. Transfer by ftp of the raw absorption spectra from the on-site computers controlling the spectrometers to the BIRA-IASB server.

2. The DOAS spectral analysis providing the trace gas differential slant column densities (DSCDs) is performed using the QDOAS software (http://uv-vis.aeronomie.be/software/QDOAS/) developed by BIRA and widely used in the DOAS community.

3. At this stage, two different approaches are followed depending of the measurement type:

3.a. MAX-DOAS measurements: tropospheric profiles and columns of trace NO_2 and aerosols are retrieved for each MAX-DOAS scan by applying the OEM-based bePRO profiling tool developed at BIRA (Clémer et al., 2010; Hendrick et al., 2013) to the measured DSCDs.

3.b. Zenith-sky DOAS measurements: the retrieval of stratospheric NO_2 and total O_3 vertical columns from measured twilight DSCDs consists of three steps: (1) determination of residual amount in the reference spectrum using the Langley-plot approach, (2) conversion of absolute slant columns into vertical columns using appropriate AMFs, and (3) averaging of the vertical columns over the 86-91° SZA range. AMFs and averaging kernels (AVKs) are extracted from the NDACC-recommended UV-vis look-up tables (http://www.ndacc.org/; see also Hendrick et al., 2010).

4. The GEOMS HDF files are created.

5. HDF files are submitted by ftp to the NDACC/NORS database.

6. An important issue is the data quality control (QC). Several QC tests have been included in the operational retrieval chain. In case of MAXDOAS retrievals (NO_2 and aerosols), each scan is screened based on its DOFS (degree of freedom for signal; DOFS should be larger than 0.7, meaning that the information comes mainly from the measurements and not from the a priori) and on the RMS of the difference between measured DSCDs and those calculated with the retrieved profiles (the RMS should be lower than a threshold value). For stratospheric NO_2 data, measurements contaminated by tropospheric pollution events are rejected based on the Langley-plot method (data points not lying on a “smooth” line indicate a tropospheric contamination). File format is directly quality-controlled by the GEOMS idlcr8hdf IDL routine creating the HDF files (see http://avdc.gsfc.nasa.gov/index.php?site=1876901039 for more details).

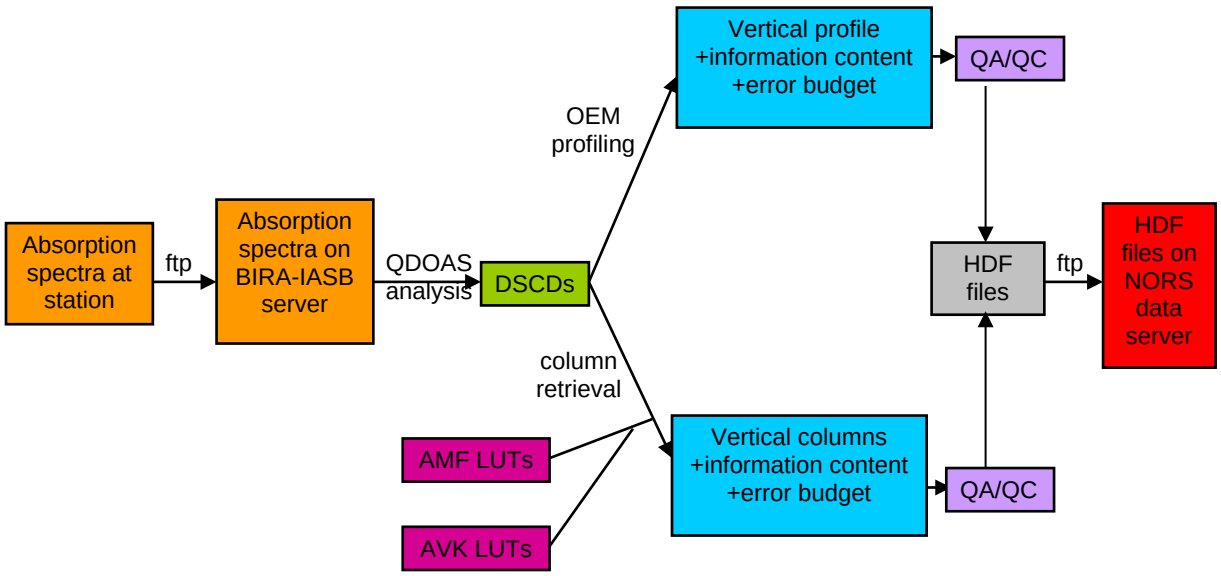

Figure 5.18: Automated DOAS retrieval chain at BIRA-IASB.

In the future, additional efforts will be put on the establishment of a comprehensive monitoring/QC of the spectral analysis (fitting residuals) and of the instrument stability (shift, slit function, offset). In the future, the automated MAXDOAS retrieval at Xianghe will be further extended to HCHO and SO_2. We plan also to implement automated retrieval chains at other BIRA stations, in particular at Bujumbura (Burundi) where a MAXDOAS spectrometer has been recently installed.

6 Minispectrometer intercalibration and satellite validation (WP 4)

6.1 Introduction

"Minispectrometer Intercalibration and Satellite Validation" is a CCN of the project, which was running from March 2013 to December 2013 [AD5, AD6]. The goals of this activity were the following:

- Collect all existing data of the Pandora spectrometer system.
- Identify for each instrument the best way to obtain a homogeneous calibration of its data. This includes an investigation of the instrument stability and possible causes of calibration change.
- Apply the best possible calibration to each station's data and recalculate the whole database of vertical O_3 and NO_2 columns from direct sun observations.
- Make recommendations about calibration of minispectrometer networks.
- Compare the resulting data base to observations from SCIAMACHY.

The following sections are essentially a summary of deliverables 1 to 7 of the activity [RD6 to RD11]. All figures and references are taken from these deliverables. The final conclusions and remarks are presented in section 1.4.

6.2 Data base

6.2.1 Data collection

We have collected and stored a total of 8547 daily Pandora Level 1 files (=raw data files) from 46 different locations (Figure 6.1 and Figure 6.2). The owners of these data have agreed to the analysis of the material within this project. Most locations are in the USA (34), 6 are in Asia, 4 in Europe, 1 in South Africa and 1 in New Zealand. In several occasions more than one Pandora were operating simultaneously at one location.

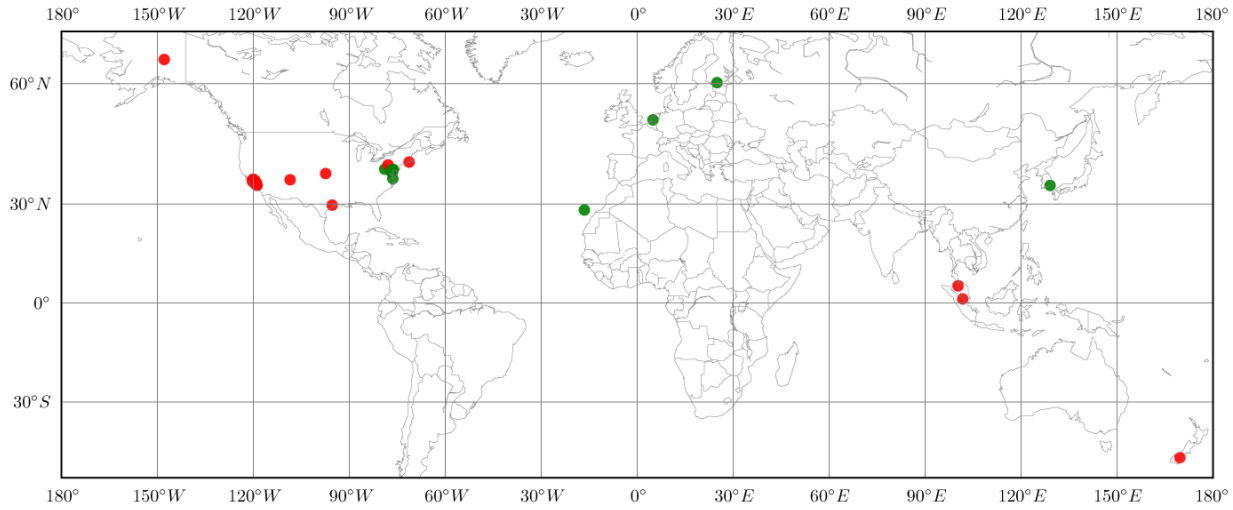

Figure 6.1: Validation locations. Green dots indicate locations with temporal overlap with SCIAMACHY. Locations marked in red have no overlap.

The data-base includes 4894 daily files before 8 April 2012 (the last date of available ENVISAT data) and 3653 daily files after 8 April 2012. Defining a "site-day" as a day, where at least one Pandora was measuring at a given location, i.e. days with multiple instruments on one site count as one site-day, we have 2858 site-days before 8 April 2012 and 2693 site-days after 8 April 2012. Most time series at a single location are short (~1 month), but at 4 locations we have time series longer than one year (Figure 6.2).

6.2.2 Instrument calibration

In addition to the field data, we also collected all laboratory calibration data (relative radiometric calibration and wavelength calibration) for each instrument. From the laboratory calibration we derive instrument parameters such as the dispersion, slit function, temperature dependence (for sensitivity and wavelength calibration), non-linearity and filter transmissions. With this characterization the Pandora Level 0 data (raw counts) are converted into Level 1 data (corrected count rates).

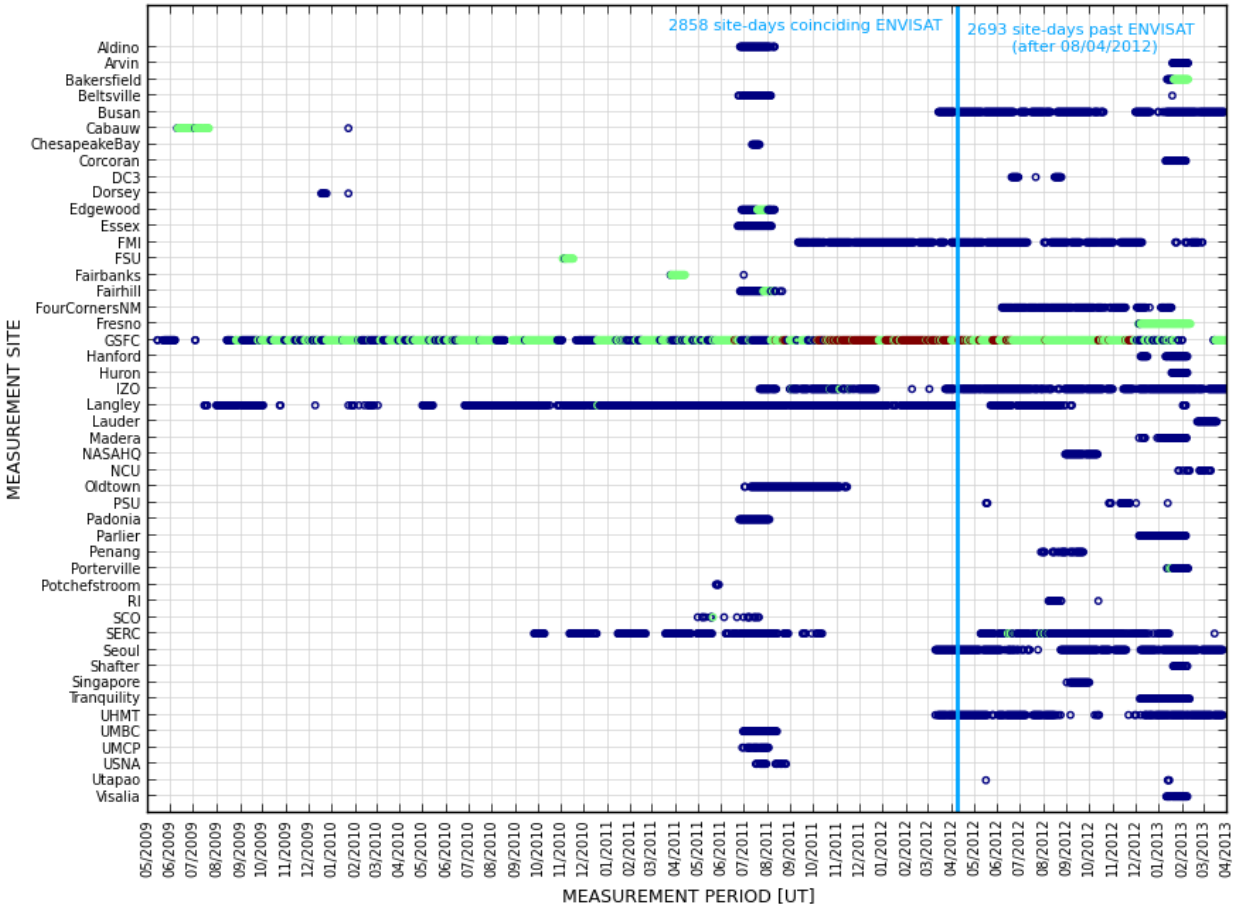

Figure 6.2: Time coverage of Pandoras. Blue dots indicate one Pandora, green dots indicate between two and five Pandoras, and red dots indicate more than five Pandoras were operating simultaneously at one location.

The vast majority of laboratory measurements provide high quality data. However, in a few instances an unstable laboratory setup required repetition of the relative radiometric calibration. This lab-instability was attributed to the temperature dependence of a metal bracket employed in the laboratory and has since been remedied.

6.2.3 Data processing

The vertical O_3 and NO_2 columns are obtained by spectral fitting on the Pandora Level 1 as described in Table 6.1.

For O_3 a convoluted extraterrestrial spectrum is used as the reference spectrum. Since this spectrum is by default absorption-free, the retrieval column amounts from the spectral fitting are absolute O_3 slant columns. By division through the direct-sun air mass factor the absolute vertical columns are obtained. One "cosmetic" disadvantage of this technique is that the spectral fitting residuals are relatively large, since systematic differences between the Pandora spectra and the extraterrestrial spectrum are always included. A possibly more serious disadvantage is that if the instrument has pronounced spectral features in the range of the fitting window, which cannot be reproduced by a 4^{th} order polynomial, a systematic bias in the data is obtained.

Table 6.1: Settings in spectral fitting algorithm for O_3 and NO_2 retrieval

Setting	**O_3 retrieval**	**NO_2 retrieval**
Fitting window	310-330 nm	400-440 nm
Order of smoothing polynomial	4	4
Order of offset polynomial	0	0
Order of wavelength change polynomial	1	1
Gases fitted simultaneously	O_3, SO_2, NO_2, HCHO	O_3, NO_2
Reference	Convoluted extraterrestrial spectrum	Synthetic reference spectrum

For NO_2 a so-called "synthetic reference spectrum" is used as the reference spectrum. This spectrum is the average over many spectra measured by the instrument itself and corrected for the NO_2 slant optical depth it includes. To estimate this NO_2 slant optical depth a field calibration called "Modified Langley extrapolation" is applied. A disadvantage of this statistical technique is that it depends to some extent on the atmospheric conditions present at the measurements days.

Note that both calibrations techniques (for O_3 and NO_2) require only data of the unit to-be-calibrated without intercomparison or traceability to a reference instrument. This was the only option with the available data set.

We applied the available laboratory and field calibrations in a systematic way to each Pandora in order to obtain the best possible database of vertical O_3 and NO_2 columns. The processed data are available in the native Pandora Level 3b format and have also been converted into GEOMS format. Since none of the

existing GEOMS templates covered the Pandora suite of measurements, we have agreed with EVDC and AVDC on a Pandora GEOMS metadata template. Compliancy checks were successfully performed and all files were processed and delivered to EVDC by end of November 2013 [RD9].

6.3 Data quality

To characterize the data quality, we determined so-called data quality parameters (DQP), which are summarized in the following sections. These DQP are then combined into a final overall data quality flag:

6.3.1 DQP1, Wavelength shift

This is the wavelength shift determined from comparing the measured spectra with the solar Fraunhofer structure. At a fixed location, Pandoras show excellent wavelength stability, where each measured spectrum differs less than 0.03 nm from the nominal dispersion. Slightly larger wavelength shifts (up to 0.1 nm) can occur, when the optical fiber is disconnected and reconnected at the spectrometer side. Figure 6.3 shows as an example the distribution of wavelength shifts for Pandora 2, which was deployed at 5 different locations. We noticed that wavelength shifts up to 0.1 nm (0.2 nm) have no significant influence on the retrievals of vertical NO_2 (O_3) columns, which means that DQP1 is virtually never limiting the data quality.

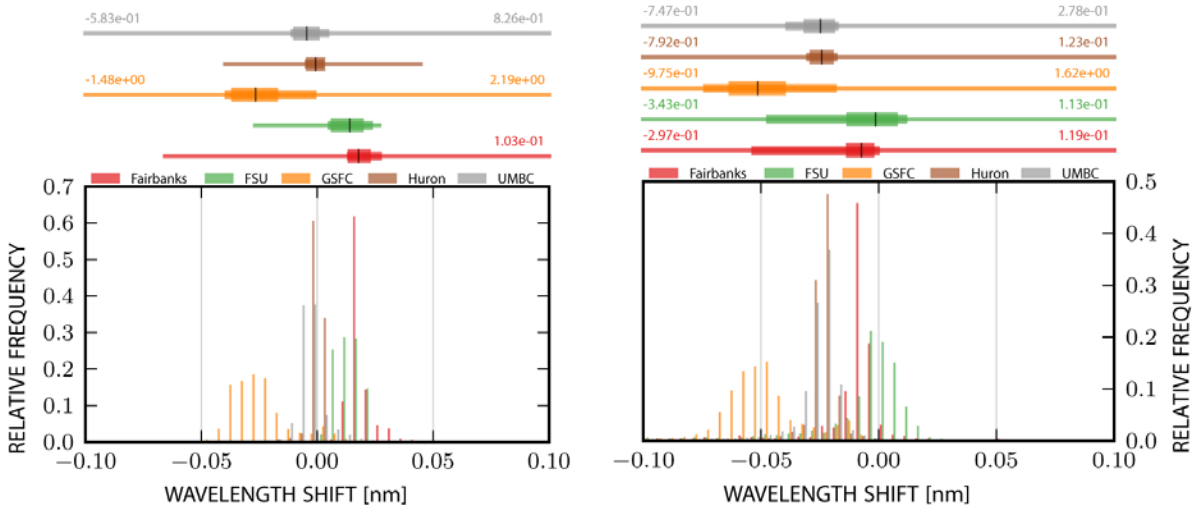

Figure 6.3: Distribution of wavelength shifts for Pandora 2 at 5 different locations (different colors) for NO_2 (left panel) and O_3 (right panel). The bars on top give the median (vertical black line), 25-75 percentile range (thickest bar), 10-90 percentile range medium thick bar), and minimum-maximum range (thin bar with numbers listed in the case they exceed the figure axes).

6.3.2 DQP2, Direct-sun air mass factor

For O_3 columns we observed internal stray light to be a limiting factor in gaining unbiased results for direct sun air mass factors >5 (solar zenith angles >79°, see Figure 6.4). This is a known problem affecting all single monochromator systems. Further sophistication of the stray light correction method should reduce this effect, allowing us to extent the reliable O_3 measurements beyond air mass factor 5.

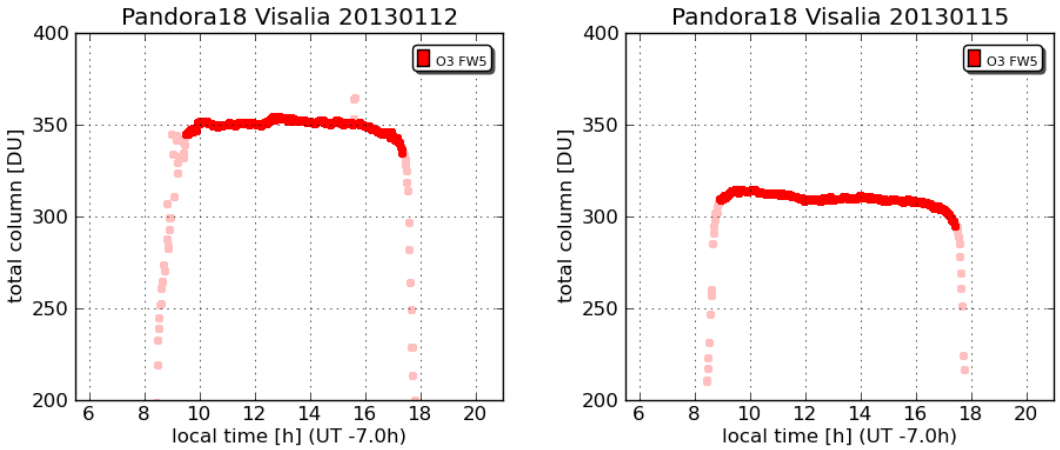

Figure 6.4: Total O_3 column derived by Pandora 18 at Visalia, California, USA, on 12 and 15 of January 2013 as a function of local time. For air mass factor >5 (data before 9:15 and after 17:00) the instrumental stray light produces a negative bias in the derived O_3 columns.

6.3.3 DQP3, Enhanced scatter

Total NO_2 data sometimes exhibit enhanced scatter. This happens usually around noon (see Figure 6.5), only affects some instruments and only during specific periods and at some locations. The cause is not understood at this time. We suspect an external noise source modifying the data. We do not know at present, whether the increased scatter is random noise, in which case the data could be averaged and are still useful, or if it includes a systematic error, which would render the data unusable. Figure 6.5 seems to suggest the latter is happening. Nevertheless, we know that the effect does not change the instrument's calibration, i.e. the data compare well with other units once the increased scatter is gone.

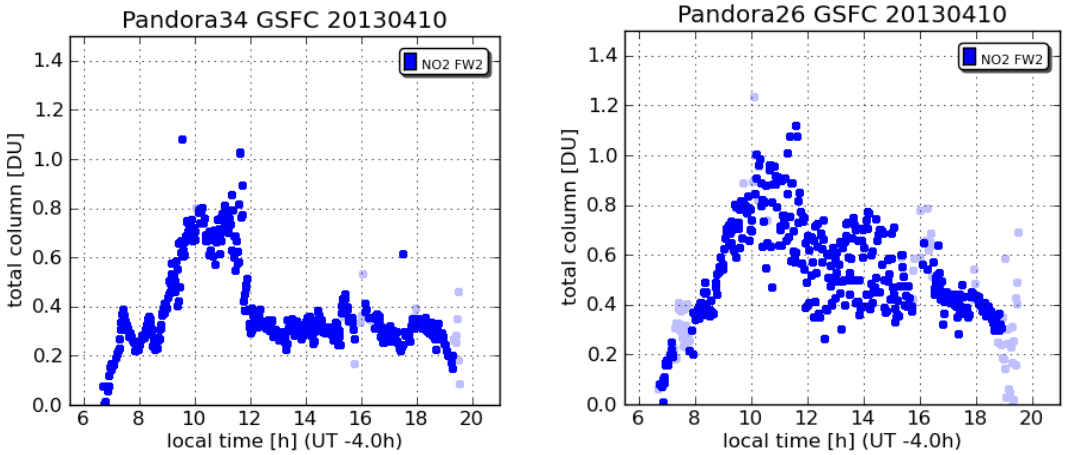

Figure 6.5: Total NO_2 columns from Pandoras 26 and 34 at Goddard Space Flight Center (GSFC) on 10 April 2013 as a function of local time. Dark blue dots have passed the cloud filter. Light blue dots have not passed it. Pandora 26 data show rather large instrumental scatter from approximately 10:00 to 16:00, while Pandora 34 data show the natural variability only.

While we do not know the reason for this effect, we have developed an automatic algorithm to detect it. The algorithm is based on comparing the sequence of the normalized root mean squares of the weighted spectral fitting residuals (wRMS) as illustrated in Figure 6.6. The enhanced scatter affects between 3 % and 30 % of the data, depending on instrument and location.

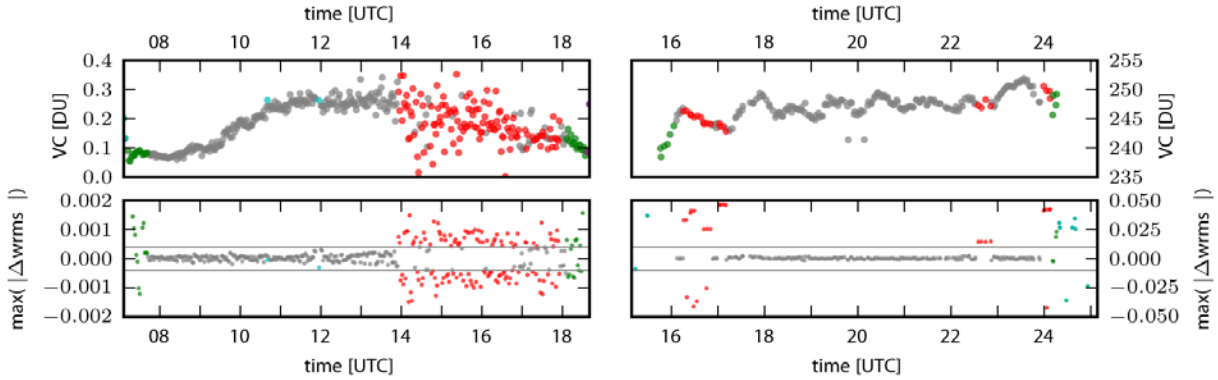

Figure 6.6: Top: diurnal variation for NO_2 (left panel) and O_3 (right panel). Bottom: diurnal variation in the maximum deviation of the adjacent wRMS values to the reference value. Red data indicate detected enhanced scatter, green data are above air mass factor 5 and cyan data are flagged as cloudy. The grey horizontal lines show the thresholds used to detect the enhanced scatter.

6.3.4 DQP4, Retrieval noise

Since the Pandora spectral fitting algorithm also includes the measured instrumental and atmospheric noise, we also obtain the "retrieval noise" for O_3 and NO_2, which we use as a cloud filter. For direct sun data we expect a bimodal distribution of the retrieval noise (Figure 6.7).

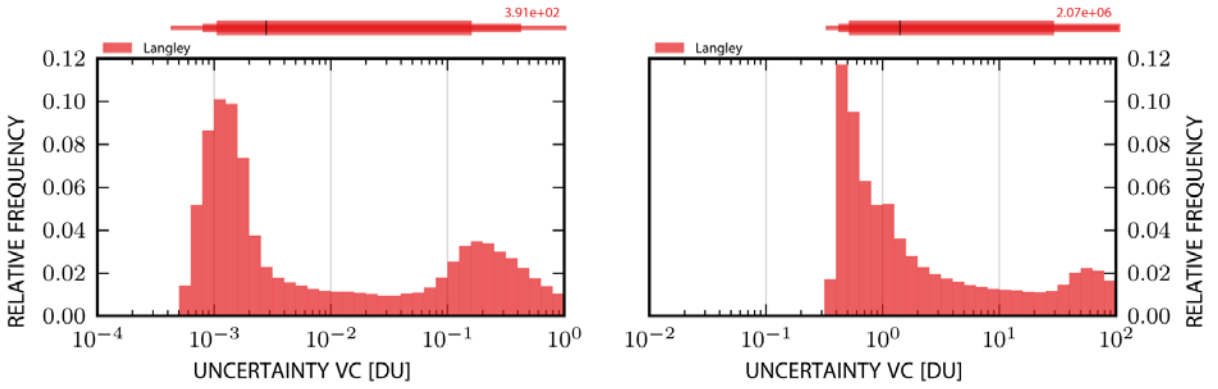

Figure 6.7: Distribution of retrieval noise of Pandora 6 for NO_2 (left panel) and O_3 (right panel). The bimodal behavior indicates situations where the sun is not covered by clouds (low noise) and situations where the sun is covered by clouds (high noise).

One peak represents situations, where the sun is not covered by clouds, and one peak where the sun is covered by clouds. In between the peaks are data for a large number of aerosols or thin clouds in the optical path from the sun to the instrument. In between the peaks the threshold for the cloud filter should be located. All Pandora units show comparable magnitudes of the retrieval noise. Thus we choose the Pandora unit with the longest continuous (i.e. excluding travel-uncertainties) time series to define the cloud filter thresholds, which we have set to 0.05 DU for NO_2 and 5 DU for O_3. The cloud filter affects between 5 % and 45 % of the data, depending on the location.

6.3.5 DQP5, Normalized root mean square of the weighted spectral fitting residuals wRMS

The wRMS are another parameter obtained in the spectral fitting. We can expect a close correlation of wRMS and the retrieval noise and hence also a bimodal distribution for wRMS in the direct sun data. The bimodal behavior is exemplary shown for Langley, Pandora 6 (Figure 6.8). However the clear separation of sun-free and sun-covered situations obvious for the retrieval noise is less pronounced for wRMS, especially for NO_2. The reason for that is still a point under investigation. The consequence is that data passing the cloud filter (i.e. below a certain retrieval noise) can still exhibit enhanced wRMS. We define the thresholds for wRMS to 0.005 for NO_2 and 0.02 for O_3. The wRMS filter affects between 5 % and 35 % of the data, depending on instrument and location.

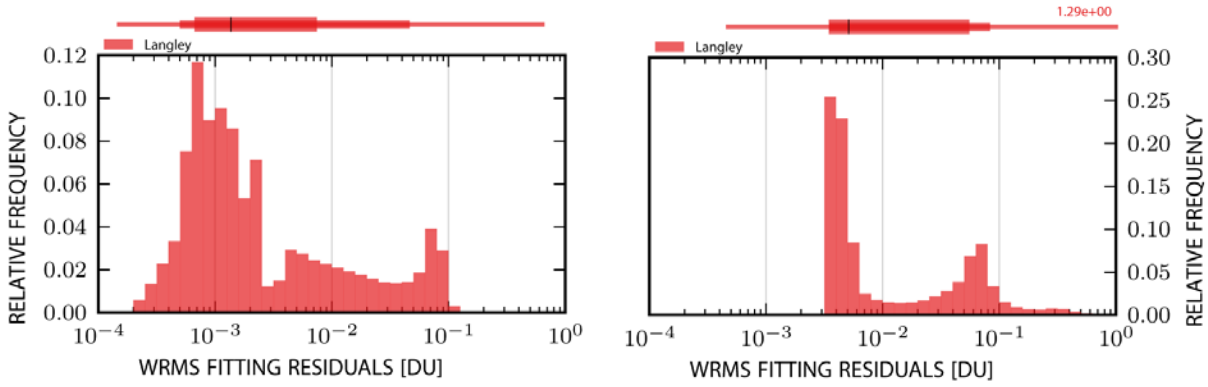

Figure 6.8: Distribution of the normalized root mean square of the weighted fitting residual of Pandora 6 for NO_2 (left panel) and O_3 (right panel). The almost bimodal behavior indicates sun-free (low wRMS) and sun-covered (high wRMS) situations.

6.3.6 DQP6, Saturation and fitting errors

Saturated pixels and fitting errors (e.g. that the maximum number of iterations is exceeded in the non-linear spectral fitting) are also considered in the overall data quality.

6.3.7 Overall data quality

The overall data quality (DQ) is separated into three groups:

- DQ0, “high quality”, ready to use: data is labeled as DQ0 if all data quality parameters DQP1 to DQP8 are below the defined thresholds.
- DQ1, “medium quality”, handle with care: data is labeled as DQ1 if any of the parameters DQP1 to DQP3 exceeds the defined thresholds.

- DQ2, “low quality”, do not use: data is labeled as DQ2 if any of the parameters DQP4 to DQP6 exceeds the defined thresholds.

The evaluated overall data quality for Pandora NO_2 and O_3 retrievals is presented in Table 6.2. In this table the DQ flags are evaluated for each Pandora, including all retrievals, no matter where the instrument has been deployed. Note that only a very small fraction of DQ2 is due to saturated pixels. Most situations in DQ2 are due to clouds.

Table 6.2: Overall data quality flags for Pandora NO_2 and O_3 retrievals. Shown are the relative occurrences of high quality data (DQ0), medium quality data (DQ1) and low quality data (DQ2) in percent (column 2 to 7). The median value covering all Pandora units is given in the last row. The number of retrievals for each Pandora unit for NO_2 (O_3) is shown in column 8 (9) with the overall number of retrievals in the last row.

Pandora number	DQ0 [%]		DQ1 [%]		DQ2 [%]		Number of retrievals	
	NO_2	O_3	NO_2	O_3	NO_2	O_3	NO_2	O_3
2	74	65	12	5	14	29	163750	159410
3	62	60	16	7	22	33	208144	207279
6	51	53	12	1	37	46	361324	360302
7	45	39	12	1	43	60	184834	180908
8	50	39	6	1	43	60	24706	23293
9	48	46	8	1	44	53	290871	282258
16	77	73	14	5	9	23	66088	66430
17	75	74	14	10	11	16	88216	82664
18	41	61	41	12	19	27	116601	111047
19	75	66	15	9	10	25	39416	39334
20	71	68	10	3	19	29	143258	139747
21	44	49	40	10	16	41	157145	154760
23	82	78	12	8	6	13	142412	141979
24	90	97	7	0	2	3	3775	1988
25	70	62	10	5	20	32	90564	92542
26	54	39	21	3	25	58	72763	41967
27	57	48	10	4	34	48	15538	15992
28	30	50	44	5	25	46	29453	25099
29	51	34	18	3	31	63	29408	18165
30	47	55	10	3	43	42	22101	18075
31	52	41	21	2	27	57	21237	21583
32	59	54	12	5	29	41	8644	8869
33	58	47	9	7	32	46	6779	7747
34	60	57	10	4	30	39	13769	14017
35	52	48	9	3	39	49	7098	7119
36	60	58	16	4	24	38	4434	4481
37	54	52	25	9	21	39	5937	5308
101	69	79	21	6	10	15	91111	87851
Median	57	54	12	4	24	40	2409376	2320214

All Pandora units are built with comparable electronic and optical components and the basic design is the same for all instruments (spectrometer, sun tracking unit, telescope, temperature controller, neutral

density and band pass filters, etc.). As a consequence, differences in the Pandora overall data quality are not so much caused by the instruments themselves, but by the conditions at the locations, where the instruments are deployed.
DQ2 is dominated by two filters: the cloud filter (DQP4 and DQP5) and the air mass factor filter (DQP2). DQ2(NO_2) gives basically the percentage cloud cover at a location. The reason DQ2(NO_2) is only 2 % for Pandora 24 is, that this unit is deployed on a ship and is activated almost only on clear sky days. DQ1 is dominated by the enhanced scatter effect (DQP3). This effect is also strongly dependent on the location. E.g. Pandora 28 was at two locations. While only 10 % of the retrievals in the first location (38 days) show enhanced scatter, 49 % of the retrievals in the second location (70 days) show this effect, giving a mean DQ1(NO_2) of 44 %. We still do not know what exactly causes this effect.

6.3.8 Additional spectral signal

We also observed another effect in the data, which is currently not captured by the data quality parameters. We frequently observe an additional spectral signal in the data (see Figure 6.9 and Figure 6.10). It seems to affect basically all instruments, but to different extent. The cause is not understood at this time. This effect does not impact the calibration, i.e. the final data are correct on average, and only seems to affect direct-sun data. However, first tests indicate that this spectral signal with a wRMS of up to 0.002 potentially impacts the derived O_3 (NO_2) columns by about ±5 DU (±0.07 DU). We believe that this temporary systematic error has an even greater impact on the retrieval of weaker atmospheric absorbers such as formaldehyde, sulfur dioxide, etc. We are working on a method to detect and eliminate this effect. Thus, reducing the uncertainty in the O_3 and NO_2 columns, as well as, significantly improve the capability to retrieve column amounts of weaker atmospheric absorbers. At present, a data user may avoid spectra including the additional signal by filtering all measurements with wRMS>0.001.

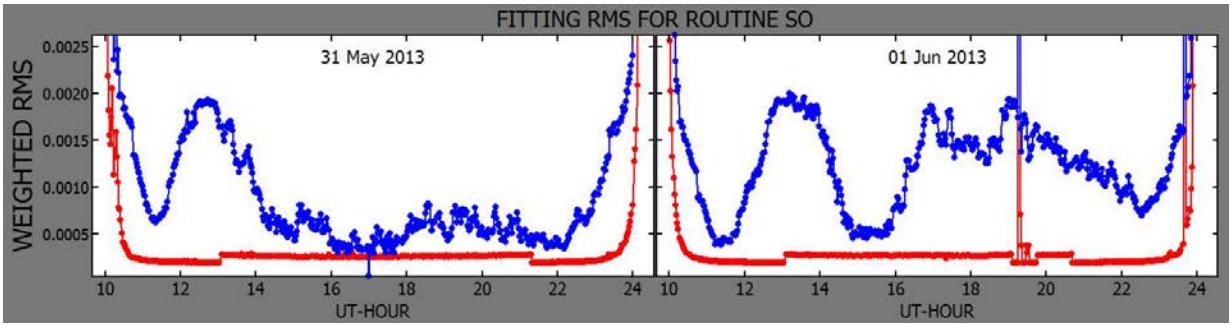

Figure 6.9: wRMS of residuals from NO_2 spectral fitting for Pandora 23 on 2013-5-31 and 2013-6-1. Red data show wRMS-level expected from instrumental noise only. Blue data show wRMS for a reference spectrum taken at 16:59 on 2013-5-31. Ideally the wRMS should be at a level below 0.001 from 11:00 to 23:00. However both days show a hump in the wRMS around 13:00, and there is also increased wRMS on 2013-6-1 from 17:00 to 22:00. The times of elevated wRMS are characterized by a spectral signal as shown in Figure 6.10.

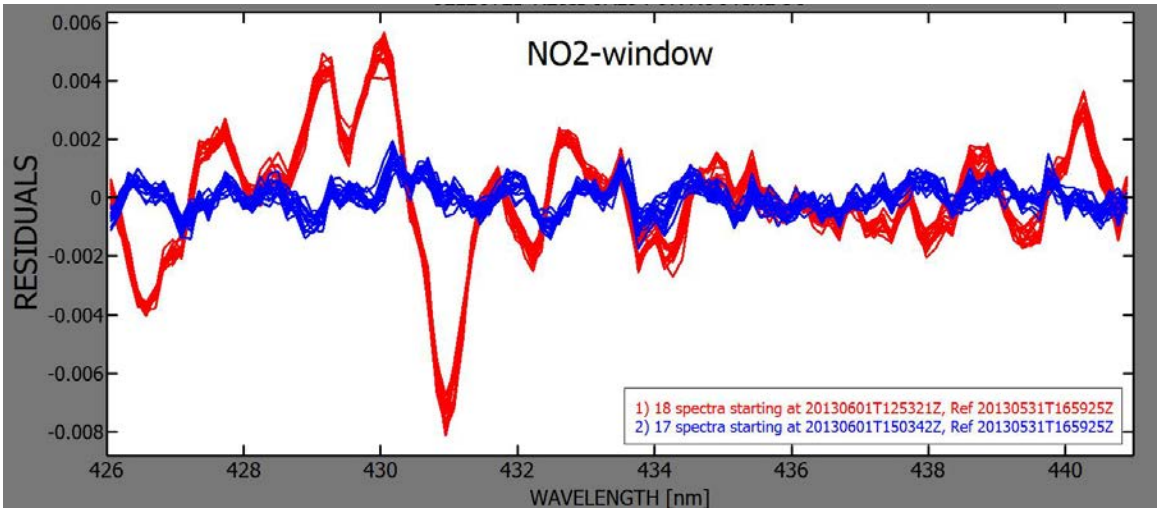

Figure 6.10: Residuals from NO_2 spectral fitting for Pandora 23 for groups of spectra on 2013-6-1 as a function of wavelength for the range 426 to 441 nm. Blue lines are spectra taken around 15:00 with wRMS around $5x10^{-4}$, i.e. the expected value. Red lines are spectra taken around 13:00 with wRMS around $2x10^{-3}$. The additional spectral signal for other spectra with elevated wRMS seen in Figure 6.9 also looks like the red lines.

6.4 Recommendations for minispectrometer networks

Recommendations for minispectrometer networks depend on the uncertainty requirements of the network. Our analysis is based on the following requirements:

- The homogeneity of 10 min-averaged network data of total O_3 (NO_2) columns from non-obstructed (i.e. no cloud in line of sight) direct sun observations for SZA<80° (SZA<85°) should be ±10 DU (±0.1 DU).
- The calibration drift of the network should be smaller than 2 DU (0.05 DU) per 10 years for total O_3 (NO_2) columns.

Under "homogeneity" we understand that all monitoring instruments measure in the same way. So the data can be biased, as long as the bias is the same for all units.

Two key-questions were analyzed for this purpose:

- How affected are the instruments by transport?
- How stable are the instruments when installed at a fixed location?

6.4.1 How affected are the instruments by transport?

The answer to this question is especially important when selecting a network instrument. Mobile reference instruments are frequently transported, i.e. dismantled, packed, shipped, unpacked, and mounted at a new location. Each of these processes could affect the hardware, causing calibration changes. Data analysis from a cross section of Pandoras was made to validate whether Pandora-like instruments are good travelers, or not. We detected "typical" transfer effects of 2 DU (0.01 DU) for O_3 (NO_2). This means that Pandoras are in general very good "traveler". Nevertheless for a network operation we recommend mobile reference instruments to travel to the monitoring locations and not

the opposite. This has the advantage that by comparing the mobile reference with the stationary reference before and after the period at the monitoring location, a possible calibration change during the transport can definitely be detected. We suspect the main reason for the transfer effect to be that the instrument is dismantled for the transport and then reassembled at the site. The fiber is disconnected on at least one end (spectrometer or head sensor) and then reconnected. This can cause small variations in the spectral throughput. In addition the manner the fiber is curled changes from location to location, which has some influence. Therefore, minimizing the travel effect for the mobile reference instruments is an essential part of the network operation.

6.4.2 How stable are the instruments when installed at a fixed location?

To answer this question we performed a stability check on the three longest Pandora time series. Due to a lack of ground-based reference data, we have chosen OMI as the independent reference as it provides a wider range of temporal and spatial coincidences than other satellite data products considered (see Figure 6.11 and Figure 6.12).

Without making a detailed quantitative trend analysis, which would include removing the seasonal difference in the data sets, we claim conservatively that a possible drift in the Pandora O_3 columns is <3 DU per 2 years and in the Pandora NO_2 columns is <0.05 DU per 2 years.

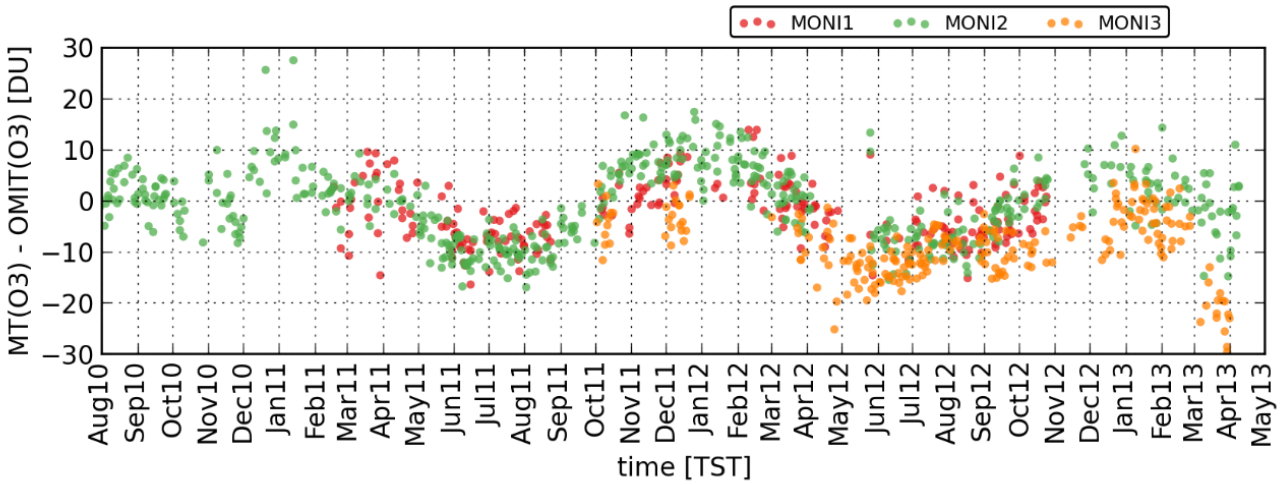

Figure 6.11: O_3 differences for (stationary, un-interrupted, one-time calibrated) Pandoras at 3 stations to the satellite product retrieved from OMI. The sinusoidal distribution observable in the data is attributed to the effective O_3 temperatures used in each retrieval algorithm. The OMI algorithm corrects for seasonal and latitudinal variations in atmospheric temperatures, whereas, Pandora utilizes a constant effective O_3 temperature. Apart from this, the overall agreement to OMI is excellent, showing no obvious drift between data sets for more than two and a half years.

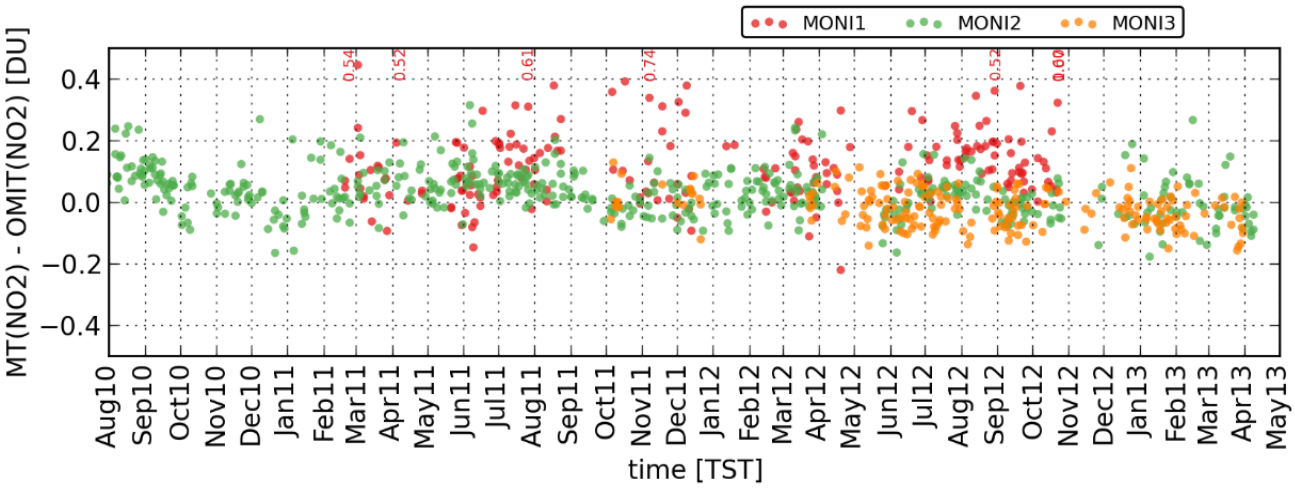

Figure 6.12: NO_2 differences for (stationary, un-interrupted, one-time calibrated) Pandoras at 3 stations to the satellite product retrieved from OMI. Outliers are written out in the corresponding color.

6.4.3 Specific network recommendations

Our recommendations for a network calibration strategy for 'Pandora-like' minispectrometer networks are the following:

- Our preferred intercomparison method is that a mobile reference instrument periodically visits the monitoring stations, as the main goal of the network is to provide long, un-interrupted data series of atmospheric parameters.
- Monitoring instruments shall only be transported if laboratory calibration is required and no proper laboratory is present at the operation site.
- The network shall have at least one, but preferably two and ideally three stationary reference instruments. They shall be located at a pristine site, where field calibration techniques can be applied with greater success than in polluted environments.
- In addition to stationary reference instruments, the network shall have a number of mobile reference instruments, dependent on the size of the network.
- In order to minimize the influence of temporary systematic effects, calibration transfers from the stationary reference instruments to a mobile reference instrument and from a mobile reference instrument to a monitoring instrument shall include at least five clear sky days. Therefore, we recommend an average time for the intercomparison between a mobile reference instrument and a monitoring instrument of two weeks. Weather conditions can increase or reduce the number of days needed.
- Allowing for travel time and intercomparison to stationary reference instruments, it is possible that one mobile reference instrument checks the calibration status of 10-15 monitoring instrument per year.
- The results of this analysis have shown that a rotation of every two years calibration of a monitoring instrument by a mobile reference instrument is enough for total O_3 and NO_2 columns. Therefore, the approximate number of mobile reference instruments needed for the entire network is ceil(n/25), where n is the number of monitoring instruments.

- If the personnel at the monitoring site are well trained, a mobile reference instrument can be sent by mail to the monitoring site, installed, operated by local operators, and then returned by mail. If the local operators are not adequately trained, the mobile reference instrument shall be brought, installed, operated, and returned by network operators. Note that 'adequate training' does not refer to data processing, which is achieved from a central server. Rather, adequate training refers to the preparation of an operator in correct installation, operation, and alignment techniques of the instrument.

6.4.4 Network uncertainty

Table 6.3 gives an estimation of the data homogeneity for a Pandora-like minispectrometer network, in the case that all recommendations listed in 6.4.3 are applied. We assume all uncertainty contributions to be uncorrelated. At present, the homogeneity is driven by the temporary systematic effects (see row with red background), specifically by the additional spectral signal in the data (section 6.3.8). Currently our main goal is to reduce the occurrence and impact of this effect. We can see that the drift correction uncertainty, calculated for a two years cycle of intercomparisons between the monitoring instrument and the mobile reference instrument, is small. Thus, indicating that an even longer data period might be usable.

Table 6.3: Summary of all uncertainty contributions; numbers are in DU at the 1-sigma-level (or 1 standard deviation) and refer to 10min averages of un-obstructed direct sun observations for SZA<80° and SZA<85° for O_3 and NO_2, respectively.

Uncertainty contribution	O_3	NO_2	Remark
Noise	0.2	0.002	Estimated for 10min averages
Permanent systematic effects	0.3	0.001	Stray light error not included, as it applies to SZA outside the required range
Temporary systematic effects	5.0	0.07	Caused by additional spectral signal
Calibration transfer uncertainty	0.7	0.007	Includes both transfers
Transport uncertainty	2.0	0.01	Based on section 6.4.1
Drift correction uncertainty	0.6	0.01	Based on section 6.4.2
Homogeneity	5.5	0.072	= combination of all uncertainties, assuming no correlation

6.5 Validation of SCIAMACHY O_3 and NO_2 retrievals

The reprocessed data base was used to validate vertical column amounts of O3 (TO3) and NO2 (TNO2) retrieved from SCIAMACHY. The SCIAMACHY overpass data for each location were provided by ESA, extracted from Level 2 data by Alessandro Burini. Whenever there was more than one Pandora measuring within one SCIAMACHY footprint, there data were averaged before comparing to SCIAMACHY. The overpass time of SCIAMACHY at about 10:00 local time implies that the direct-sun data from Pandora has been measured at moderate to high solar zenith angles. If we estimate the effective

O3 (NO2) absorption layer height to 20.1 km (1.0 km), the effective validation location is not the ground geolocation itself. Instead, the effective location is shifted towards the South-East direction (on the Northern Hemisphere). While this has a minor effect for TNO2 validation, the spatial shift can be significant for TO3 validation: in winter months in the Northern hemisphere the latitudinal (longitudinal) shift is about 40 km (15 km) for mid latitudes. In order to enhance the representativeness of the Pandora direct-sun retrievals, we referred to the effective Pandora locations throughout this validation study.

6.5.1 Sensitivity study for O_3 validation

We conducted a sensitivity study to estimate the influence of the following filter parameters on the validation:

1) Longitudinal distance of footprint-center distance to effective Pandora location
2) Latitudinal distance of footprint-center distance to effective Pandora location
3) Size of SCIAMACHY footprint
4) SCIAMACHY cloud fraction
5) Pandora vertical column uncertainty
6) Pandora data averaging interval time around SCIAMACHY overpass time

The sensitivity study was performed for the two stations with the longest time Pandora series, Langley (Fairfax, Virginia) as a location considered to be rural and GSFC (Goddard Space Flight Center, Greenbelt, Maryland) as an urban location. The result of the sensitivity study is as follows:

- Filter parameters 1 to 3 have no significant influence on the validation, as long as the ground location is included in the SCIAMACHY footprint.
- Filter parameters 4 and 5 are interconnected. As long as filter parameter 5 is below 5 DU, the exact setting of filter parameter 4 does not matter.
- Filter parameter 6 is optimal for 160-200 min averaging time around the SCIAMACHY overpass.

Based on the study and considering the 6-days overpass cycle of SCIAMACHY, we selected the thresholds for the filter parameters that gave us the highest quantity of data. We chose the Pandora DQ0 (high quality data, uncertainty <5 DU) and a 200 min window around the SCIAMACHY overpass time.

6.5.2 O_3 time series

Currently, the standard Pandora TO3 algorithm does not include a variable effective O_3 temperature, while satellite products from SCIAMACHY and OMI do. As a consequence we see an undulating difference between the satellite and Pandora data during the year. Overestimation in O_3 effective temperature leads to overestimation in TO3 and vice versa. The time series for the difference in SCIAMACHY and Pandora for Langley and GSFC again reveals the expected temperature wave, more obvious for OMI (Figure 6.13 bottom) than for SCIAMACHY (Figure 6.13 top) due to the higher data density. The spring and autumn TO3 median differences are almost equal. Pandoras gas temperature related error is approximately 7 DU in the extreme points (summer and winter).

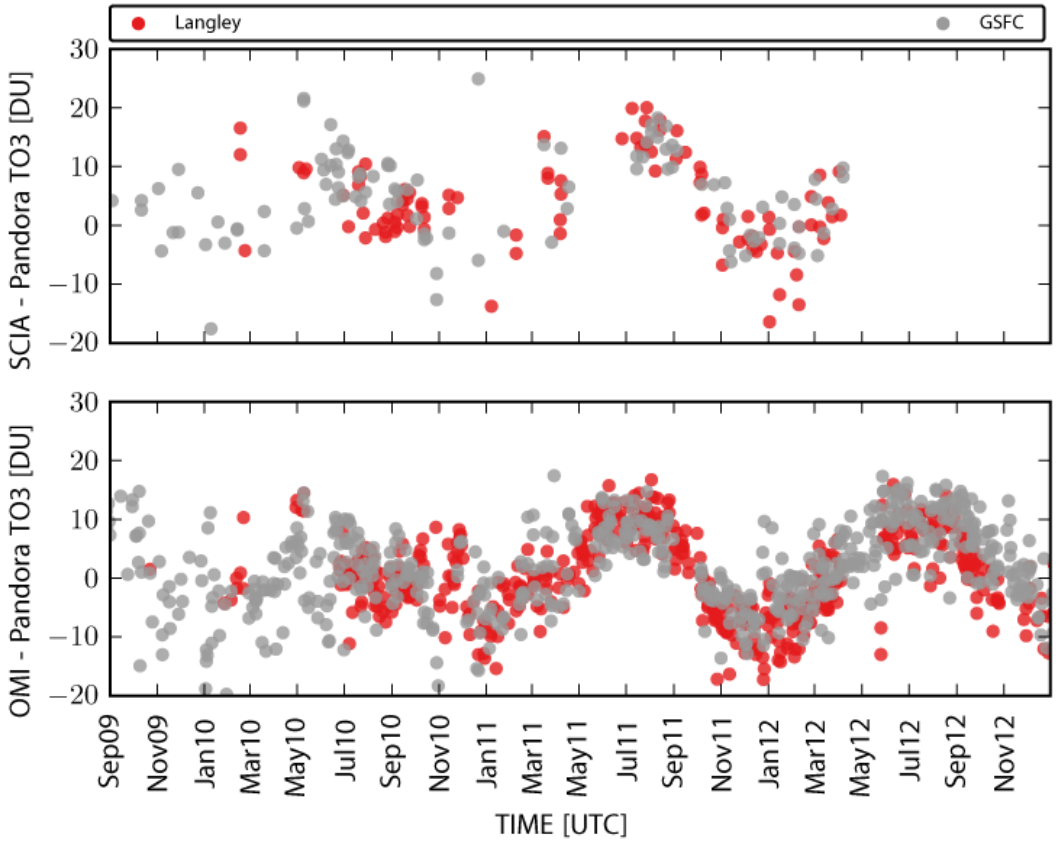

Figure 6.13: Time series for the difference of SCIAMACHY (top panel) and OMI (bottom panel) to Pandora. Depicted are data from Langley and GSFC. The wave structure is related to the effective O_3 temperature. Due to the 6-days overpass repeat cycle of SCIAMACHY it provides significantly less coincidences than OMI.

We can observe in Figure 6.13 that the seasonal cycle in the TO3 differences is not as defined before May 2011 than after this date. We carefully checked whether this could be due to the Pandoras measuring at GSFC and Langley. We have no indication that they might not have worked properly. Therefore we suspect that this may be caused by the effective O_3 temperature itself. We made a rough estimation of T_{eff} at GSFC for the period 2010 to 2012 using the O_3 profile from the US Standard Atmosphere in combination with the NOAA ESRL/PSD GEFS forecast version 2, which gives the atmospheric temperature profile for 11 pressure layers (data available from http://www.esrl.noaa.gov/psd/forecasts/reforecast2/download.html).

Figure 6.14 shows the TO3 differences OMI to Pandoras (top panel) and T_{eff} (bottom panel) at GSFC. The year 2012 exhibits a pronounced annual cycle in the difference OMI to Pandora, corresponding to a clear variation in T_{eff}. The offset is mainly driven by the algorithm temperature error from Pandora data. In contrast, the year 2010 shows reduced amplitude in T_{eff} attributable to warmer winter periods. This causes on the one hand less temperature error from Pandora retrievals but on the other hand enhanced

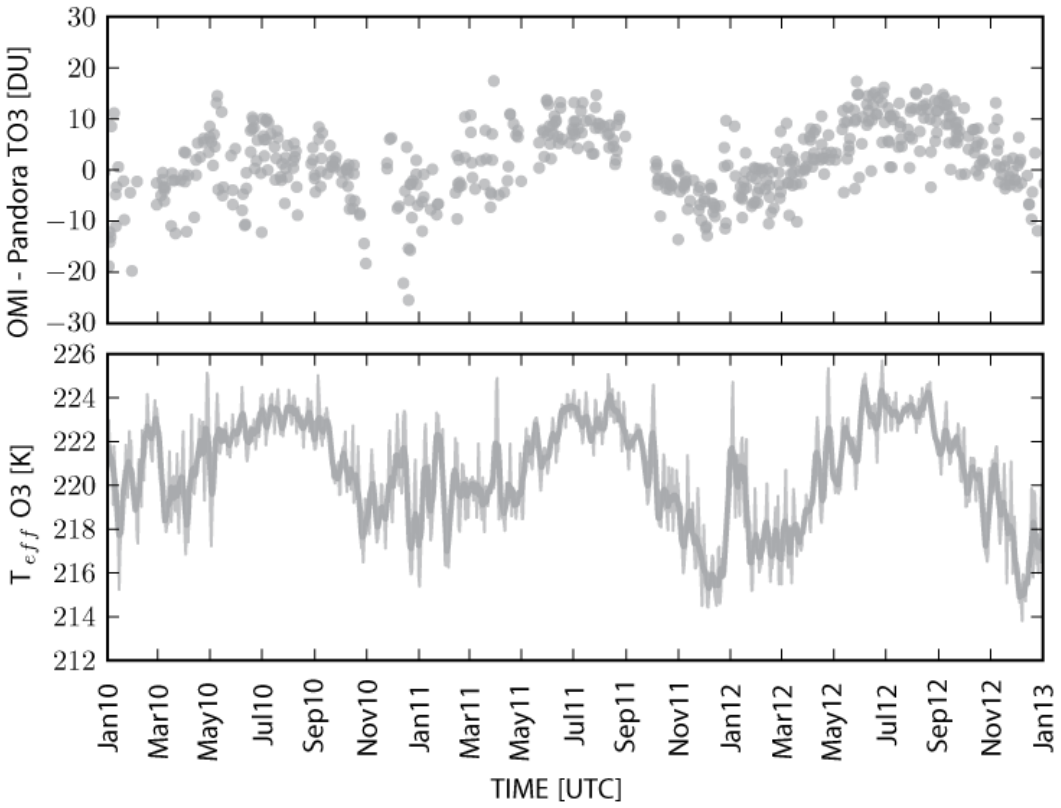

temperature errors from OMI retrievals due to enhanced deviation from the assumed temperature climatology. This superposition of different temperature related errors from Pandora and OMI leads to increased data scattering in the TO3 difference. This is clearly mirrored from November 2010 to May 2011. The OMI to Pandora offset is particularly uncorrelated in this region and coincides with rapidly varying T_{eff} around the same temperature.A correction for the temperature related retrieval error in Pandora data is necessary to actually quantify the temperature related algorithm error when using a temperature climatology in satellite retrievals. Preliminary tests have shown the retrieval of effective O_3 temperature by Pandora is possible with a further developed algorithm. We are presently working on such an algorithm to be used in routine network operation.

Figure 6.14: TO3 differences OMI to Pandora at GSFC (top panel, same as data as in bottom panel of Figure 6.13) and the effective O_3 temperature T_{eff} (bottom panel, thin line daily values and thick line weekly averages). T_{eff} is based on temperature profiles from ESRL/PSD GEFS reforcast database.

6.5.3 Results of O_3 validation

For each Pandora location overlapping with SCIAMACHY we produced a scatterplot as shown in Figure 6.15 for GSFC.

The results for the individual stations are summarized in Table 6.4. For columns $MEDD_{TCORR}$ and CC_{TCORR} we applied a very rudimentary method to remove the effect of the effective O_3 temperature. We added (removed) 7 DU to (from) the Pandora TO3 summer (winter) values before forming the median difference and correlation coefficient. The spring and autumn values remain untouched, since we assume the constant gas temperature to be suitable throughout these months.

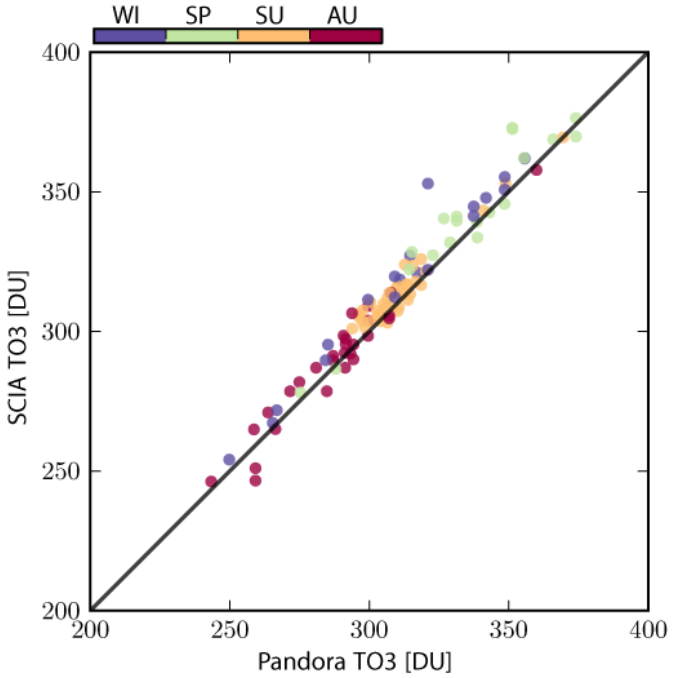

Figure 6.15: Scatterplot Pandora TO3 versus SCIAMACHY TO3 for all data at GSFC. Different colors represent different seasons. Black line is the 1:1 line.

Table 6.4: TO3 validation results for each location; n is Number of data, MEDD is the median of the difference SCIA TO3-Pandora TO3, CC is the correlation coefficient, $MEDD_{TCORR}$ and CC_{TCORR} are like MEDD and CC, but applying the temperature correction to the Pandora data.

Location	N	MEDD	$MEDD_{TCORR}$	CC	CC_{TCORR}
Aldino	6	14.9 DU	7.9 DU	0.96	0.96
Beltsville	85	4.5 DU	4.0 DU	0.97	0.98
Busan	5	4.5 DU	4.5 DU	0.97	0.97
Cabauw	13	0.5 DU	-6.5 DU	0.89	0.89
Edgewood	9	12.4 DU	5.6 DU	0.97	0.98
Essex	10	18.4 DU	12.5 DU	0.94	0.96
FMI	18	4.2 DU	4.2 DU	0.99	0.99

FSU	4	8.4 DU	6.6 DU	0.99	1.00
GSFC	106	4.9 DU	3.9 DU	0.97	0.98
IZO	17	4.4 DU	5.9 DU	0.99	0.98
Langley	95	2.1 DU	3.5 DU	0.97	0.98
NASAHQ	106	4.9 DU	3.9 DU	0.97	0.98
Oldtown	17	19.9 DU	12.9 DU	0.95	0.95
Padonia	10	13.4 DU	7.2 DU	0.94	0.95
SERC	65	5.5 DU	4.0 DU	0.97	0.98
UMBC	14	20.0 DU	13.6 DU	0.89	0.89
UMCP	87	4.4 DU	4.0 DU	0.98	0.98
USNA	66	4.9 DU	3.8 DU	0.98	0.98

The MEDD range from 0 to 20 DU and the $MEDD_{TCORR}$ from -7 to 13 DU. Excluding Cabauw, all CC are above 0.95 and the $MEDD_{TCORR}$ are between 3 and 13 DU. On average the SCIAMACHY TO3 are 8±5 DU (about 1-4 %) higher than the Pandora TO3. This bias can have several reasons. From the Pandora side the most likely explanation is a too low calibration standard. Remember, that the Pandora data are not referenced to any standard instrument, but use a calibration purely from the laboratory. More important than the bias is the excellent homogeneity of the Pandora data, which is the main goal of a ground based network. One can state that variability among the results from station to station is minimal, falling well within the uncertainty ranges for both Pandora and SCIAMACHY.

Cabauw (summer data only) is different from all other locations with a CC=0.89 and a $MEDD_{TCORR}$=-6 DU, i.e. SCIAMACHY about 2 % lower than Pandora. Thus it is the only location where the bias is significantly worse for $MEDD_{TCORR}$ than for MEDD. The negative bias could be related to the geolocation of Cabauw. At 50°N, the average summer temperatures are expected to be lower compared to e.g. GSFC. The underestimation in temperature would lead to an underestimation in TO3 for the Pandora retrieval.

6.5.4 NO_2 validation

As for O_3, we based the NO_2 validation on the SCIAMACHY vertical column amounts provided by ESA. Figure 6.16 shows a comparison of TNO2 from Pandora and SCIAMACHY at GSFC using the ESA-provided data in the left panel and the SCIAMACHY retrievals from http://www.temis.nl/airpollution/no2col/data/scia/overpass/Goddard_sciano2.dat in the right panel. The right panel shows an excellent average agreement between ground and satellite observations. The satellite data in the left panel underestimate the column amounts by approximately a factor of 2. The SCIAMACHY (ESA) data scaled by this factor are shown in gray color. The same large discrepancy in the provided SCIAMACHY NO_2 columns is seen at each single Pandora location. This makes any further analysis meaningless.

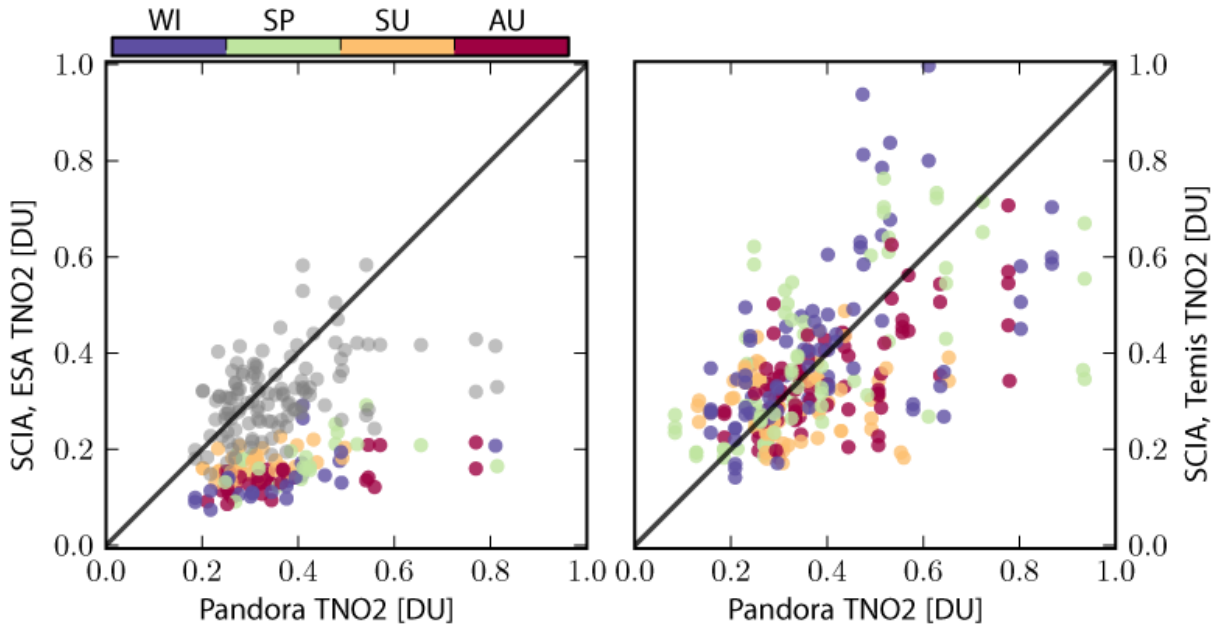

Figure 6.16: TNO2 scatter plot for SCIAMACHY and Pandora data from GSFC. The colored data in the left panel show SCIAMACHY TNO2 extracted from SCIAMACHY level 2 files, in the right panel data from Temis. The SCIAMACHY TNO2 underestimate the Pandora TNO2 by approximately a factor of 2. The gray data are the SCIAMACHY data multiplied by 2. The color code reflects the different seasons.

The SCIAMACHY TNO2 provided by ESA are largely underestimating the true NO_2 columns. This is not a problem of data extraction and interpretation from the provided files, since we have checked carefully whether the correct columns were used or any scaling or offset factors were not applied. The underestimation of approximately a factor of 2 is due to the SCIAMACHY retrievals of TNO2 for polluted areas, which does not use a proper tropospheric air mass factor for such situations. Therefore we did not proceed with a detailed validation analysis as we did for O_3. This is unfortunate since for TNO2 we had expected interesting results from a sensitivity study and also were looking forward to test the climatological correction outlined in the validation strategy.

7 References

Bass, A. M. and Paur, R. J.: The ultraviolet cross-sections of ozone. I. The measurements, II – Results and temperature dependence, in: Atmospheric ozone; Proceedings of the Quadrennial, 1, 606–616, 1985.

Bernhard, G., Evans, R. D., Labow, G. J., and Oltmans, S. J.: Bias in Dobson total ozone measurements at high latitudes due to approximations in calculations of ozone absorption coefficients and air mass, J. Geophys. Res, 110, D10305, doi:10.1029/2004JD005559, 2005.

Brion, J., Chakir, A., Daumont, D., Malicet, J., and Parisse, C.: High-resolution laboratory absorption cross section of O3. Temperature effect, Chem. Phys. Lett., 213, 610–612, 1993.

Clémer, K., Van Roozendael, M., Fayt, C., Hendrick, F., Hermans, C., Pinardi, G., Spurr, R. J. D., Wang, P., De Mazière, M, Multiple wavelength retrieval of tropospheric aerosol optical properties from MAXDOAS measurements in Beijing. Atmos. Meas. Tech., 3, 863–878, 2010.

Daumont, D., Brion, J., Charbonnier, J., and Malicet, J.: Ozone UV spectroscopy I: Absorption cross-sections at room temperature, J. Atmos. Chem., 15, 145–155, 1992.

Fragkos, K., Bais, A. F., and Meleti, C.: Effect of Atmospheric Temperature Variations on Total Ozone Mea- sured with a Brewer MKII Spectrophotometer at Thessaloniki, in: Advances in Meteorology, Climatology and Atmospheric Physics, edited by: Helmis, C. G. and Nastos, P. T., Springer Atmospheric Sciences, 959– 965, Springer Berlin Heidelberg, 2013a.

Fragkos, K., Bais, A. F., Balis, D., Meleti, C., and Koukouli, M.: The effect of three different absorption cross sections and their temperature dependence on total ozone of a mid- latitude Brewer spectrophotometer, Atmos.-Ocean, 2013b.

Frieß, U., H.K. Baltink, S. Beirle, K. Clémer, H. Irie, M. van Roozendael, R. Shaiganfar, T. Wagner, T. Vlemmix, S. Yilmaz, and P. Zieger, Intercomparison of aerosol extinction profiles retrieved from MAX-DOAS measurements, to be submitted to Atmos. Meas. Tech., 2014.

Gorshelev, V., Serdyuchenko, A., Weber, M., Chehade, W., and Burrows, J. P.: High spectral resolution ozone absorption cross-sections ; Part I: Measurements, data analysis and comparison with previous measurements around 293 K., Atmos. Meas. Tech. Discuss., 6, 6567–6611, doi:10.5194/amtd-6-6567-2013, 2013.

Grobner, J., Wardle, D. I., McElroy, C. T., and Kerr, J. B.: Investigation of the wavelength accuracy of Brewer spBass, A. M. and Paur, R. J.: The ultraviolet cross-sections of ozone. I. The measurements, II – Results and temperature dependence, in: Atmospheric ozone; Proceedings of the Quadrennial, 1, 606–616, 1985.

Hendrick, F., J.-F. Müller, K. Clémer, M. De Mazière, C. Fayt, C. Hermans, T. Stavrakou, T. Vlemmix, P. Wang, and M. Van Roozendael, Four years of ground-based MAX-DOAS observations of HONO and NO2 in the Beijing area, Atmos. Chem. Phys. Discuss., 13, 10621-10660, 2013 (accepted for publication in Atmos. Chem. Phys.).

Hendrick, F., J.-P. Pommereau, F. Goutail, R. D. Evans, D. Ionov, A. Pazmino, E. Kyrö, G. Held, P. Eriksen, V. Dorokhov, M. Gil, and M. Van Roozendael, NDACC/SAOZ UV-visible total ozone measurements:

Improved retrieval and comparison with correlative ground-based and satellite observations, Atmospheric Chemistry and Physics, 11, 5975-5995, 2011.

Irie, H., Takashima, H., Kanaya, Y., Boersma, K. F., Gast, L. F. L., Wittrock, F., Van Roozendael, M., et al., Eight-component retrievals from ground-based MAX-DOAS observations. Atmos. Meas. Tech. Discuss., 4(1), 639–690, 2011.

Kerr, J. B., Asbridge, I. A., and Evans, W. F. J.: Intercomparison of Total Ozone Measured by the Brewer and Dobson Spectrophotometers at Toronto, J. Geophys. Res., 93, 11129–11140, 1988.

Kerr, J.: New methodology for deriving total ozone and other atmospheric variables from Brewer spectropho- tometer direct sun spectra, J. Geophys. Res, 107, 4731, doi:10.1029/2001JD001227, 2002.

Kohler, U., Redondas, A., and Kyro, E.: Regional Calibration Centers for Dobson and Brewer in Europe – Ajoint venture for highest quality in monitoring the ozone layer, in: Quadrennial International Ozone Symposium, Toronto, Canada, available at: http://larss.science.yorku.ca/QOS2012pdf/5967.pdf, ID5967, 2012. Komhyr, W. D. and Evans, R. D.: Dobson spectrophotometer total ozone measurement errors caused by in- terfering absorbing species such as SO2, NO2, and photochemically produced O3 in polluted air. Geophys.Res., 7(2), 157-160, 1980

Kohler, U.: Recalibration of the hohenpeissenberg dobson spectrophotometer 104 presuming effective absorp-tion coefficients, J. Atmos. Chem., 4, 359–374, 1986.

Komhyr, W. D., Mateer, C. L., and Hudson, R. D.: Effective Bass-Paur 1985 ozone absorption coefficients for use with Dobson ozone spectrophotometers, J. Geophys. Res., 98, 20451–20465, 1993.

Liu, X., Chance, K., Sioris, C. E., and Kurosu, T. P.: Impact of using different ozone cross sections on ozone profile retrievals from Global Ozone Monitoring Experiment (GOME) ultraviolet measurements, Atmos. Chem. Phys., 7, 3571–3578, doi:10.5194/acp-7-3571-2007, 2007.

Malicet, Daumont, D., Charbonnier, J., Parisse, C., Chakir, A., and Brion, J.: Ozone UV spectroscopy. II. Absorption cross-sections and temperature dependence, J. Atmos. Chem, 21, 263–273, 1995.

Pinardi, G., Van Roozendael, M., Abuhassan, N., Adams, C., Cede, A., Clémer, K., Yilmaz, S., et al., MAX-DOAS formaldehyde slant column measurements during CINDI: intercomparison and analysis improvement. Atmospheric Measurement Techniques, 6(1), 167–185. doi:10.5194/amt-6-167-2013, 2013.

Piters, A. J. M., K. F. Boersma, M. Kroon, J. C. Hains, M. Van Roozendael, F. Wittrock, N. Abuhassan, C. Adams, M. Akrami, M. A. F. Allaart, A. Apituley, J. B. Bergwerff, A. J. C. Berkhout, D. Brunner, A. Cede, J. Chong, K. Clémer, C. Fayt, U. Frieß, L. F. L. Gast, M. Gil-Ojeda, F. Goutail, R. Graves, A. Griesfeller, K. Großmann, G. Hemerijckx, F. Hendrick, B. Henzing, J. Herman, C. Hermans, M. Hoexum, G. R. van der Hoff, H. Irie, P. V. Johnston, Y. Kanaya, Y. J. Kim, H. Klein Baltink, K. Kreher, G. de Leeuw, R. Leigh, A. Merlaud, M. M. Moerman, P. S. Monks, G. H. Mount, M. Navarro-Comas, H. Oetjen, A. Pazmino, M. Perez-Camacho, E. Peters, A. du Piesanie, G. Pinardi, O. Puentadura, A. Richter, H. K. Roscoe, A. Schönhardt, B. Schwarzenbach, R. Shaiganfar, W. Sluis, E. Spinei, A. P. Stolk, K. Strong, D. P. J. Swart, H. Takashima, T. Vlemmix, M. Vrekoussis, T. Wagner, C. Whyte, K. M. Wilson, M. Yela, S. Yilmaz, P. Zieger, and Y. Zhou, The Cabauw Intercomparison campaign for Nitrogen Dioxide measuring Instruments (CINDI): design, execution, and early results, Atmos. Meas. Tech., 5, 457-485, 2012.

Redondas, A., R. Evans, R. Stuebi, U. Köhler, and M. Weber, Evaluation of the use of five laboratory-determined ozone absorption cross sections in Brewer and Dobson retrieval algorithms, Atmos. Chem. Phys., 14(3), 1635–1648, doi:10.5194/acp-14-1635-2014, 2014.

Rodgers, C. D.: Inverse Methods for Atmospheric Sounding, Theory and Practice. World Scientific Publishing, Singapore-NewJersey-London-Hong Kong, 2000.

Roscoe, H. K., Van Roozendael, M., Fayt, C., du Piesanie, A., Abuhassan, N., Adams, C., Piters, a. J. M., et al., Intercomparison of slant column measurements of NO2 and O4 by MAX-DOAS and zenith-sky UV and visible spectrometers. Atmos. Meas. Tech., 3, 1629–1646, 2010.

Savastiouk, V.: The effect of change of BP to DBM ozone absorption cross sections on total ozone from Brewer, in: Absorption Cross Sections of Ozone (ACSO), Geneva, available at: http://igaco-o3.fmi.fi/ACSO/presentations 2010/ground-based/OTM 2010 Savastiouk.pdf, 2010.

Scarnato, B., Staehelin, J., Peter, T., Gro¨bner, J., and Stu¨bi, R.: Temperature and slant path effects in Dobson and Brewer total ozone measurements, J. Geophys. Res., 114, D24, doi:10.1029/2009JD012349, 2009. Scarnato, B., Staehelin, J., Stu¨bi, R., and Schill, H.: Long-term total ozone observations at Arosa (Switzerland) with Dobson and Brewer instruments (1988–2007), J. Geophys. Res., 115, D13306,doi:10.1029/2009JD011908, 2010.

Serdyuchenko, A., Gorshelev, V., Weber, M., Chehade, W., and Burrows, J. P.: High spectral resolution ozone absorption cross-sections; Part II. Temperature dependence, Atmos. Meas. Tech. Discuss., 6, 6613–6643,doi:10.5194/amtd-6-6613-2013, 2013.

Sluis, W. W., Allaart, M. a. F., Piters, a. J. M., & Gast, L. F. L., The development of a nitrogen dioxide sonde. Atmospheric Measurement Techniques, 3(6), 1753–1762. doi:10.5194/amt-3-1753-2010, 2010.

Van Roozendael, M., Peeters, P., Roscoe, H. K., De Backer, H., Jones, A. E., Bartlett, L., Vaughan, G., Goutail,F., Pommereau, J. P., Kyro, E., Wahlstrom, C., Braathen, G., and Simon, P. C.: Validation of Ground- Based Visible Measurements of Total Ozone by Comparison with Dobson and Brewer Spectrophotometers, J. Atmos. Chem, 29, 55–83, 1998.

Vanicek, K.: Differences between ground Dobson, Brewer and satellite TOMS-8, GOME-WFDOAS total ozone observations at Hradec Kralove, Czech, Atmos. Chem. Phys., 6, 5163–5171, doi:10.5194/acp-6-5163-2006, 2006.

Wagner, T., S. Beirle, S. Dörner, U. Friess, J. Remmers, and R. Shaiganfar, Cloud detection and classification based on MAX-DOAS observations, Atmos. Meas. Tech. Discuss., 6, 10297-10360, 2013.

Wang, T., F. Hendrick, P. Wang, G. tang, K. Clémer, H. Yu, C. Fayt, C. Hermans, C. Gielen, G. Pinardi, N. Theys, H. Brenot, and M. Van Roozendael, Evaluation of tropospheric SO2 retrieved from MAX-DOAS measurements in Xianghe, China, submitted to Atmos. Chem. Phys. Discuss., 2014.

Weber, M., Chehade, W., and Spietz, P.: Impact of ozone cross-section choice on WFDOAS total ozone re- trieval applied to GOME, SCIAMACHY, and GOME2 (1995–present), in: Contribution to ACSO.(IGACO Activity: Absorption Cross-Sections for Ozone), Vol. 2, p. 25, Universitat Bremen, Bremen, available at: http://www.iup.uni-bremen.de/UVSAT material/manuscripts/weber acso 201101.pdf, 2011.

Wittrock, F., K. Clémer, S. Beirle, S. Berkhout, D. Brunner, U. Friess, L. Gomez Martin, T. Hay, F. Hendrick, H. Irie, K. Kreher, E. Peters, G. Pinardi, A. Piters A. Richter, M. Van Roozendael, W. Sluis, E. Spinei, T. Vlemmix, T. Wagner, Measurements of NO_2 profiles with MAX-DOAS: Theoretical and practical case studies as part of the Cabauw Intercomparison campaign for Nitrogen Dioxide Measuring Instruments (CINDI), to be submitted to Atmos. Meas. Tech., 2014.

Zieger, P., Weingartner, E., Henzing, J., Moerman, M., de Leeuw, G., Mikkilä, J., Baltensperger, U., et al., Comparison of ambient aerosol extinction coefficients obtained from in-situ, MAX-DOAS and LIDAR measurements at Cabauw. Atmospheric Chemistry and Physics, 11(6), 2603–2624. doi:10.5194/acp-11-2603-2011, 2011.